Investigation of Thermal-Hydraulic Effects of Dry Storage Canister Helium Backfill Loss Using the Horizontal Dry Cask Simulator

Spent Fuel and Waste Disposition

Prepared for
US Department of Energy
Spent Fuel and Waste Science and Technology

R.J.M. Pulido
R.E. Fasano
E.R. Lindgren
R.W. Williams
G.T. Vice
S.G. Durbin

Sandia National Laboratories
March 26, 2021
Milestone No. M2SF-21SN010203032
SAND2021-3653 R

Prepared by
Sandia National Laboratories
Albuquerque, New Mexico 87185 and Livermore, California 94550

Sandia National Laboratories is a multimission laboratory managed and operated by National Technology and Engineering Solutions of Sandia, LLC, a wholly owned subsidiary of Honeywell International, Inc., for the U.S. Department of Energy's National Nuclear Security Administration under contract DE-NA0003525.

EXECUTIVE SUMMARY

The thermal performance of commercial spent nuclear fuel dry storage casks is evaluated through detailed numerical analysis. These modeling efforts are completed by the vendor to demonstrate performance and regulatory compliance. The calculations are then independently verified by the Nuclear Regulatory Commission (NRC). Canistered dry storage cask systems rely on ventilation between the inner canister and the overpack to convect heat away from the canister to the surrounding environment for both horizontal and vertical configurations. Recent advances in dry storage cask designs have significantly increased the maximum thermal load in a canister in part by increasing the efficiency of internal conduction pathways and by increasing the internal convection through greater canister helium pressure. Carefully measured data sets generated from testing of full-sized casks or smaller cask analogs are widely recognized as vital for validating these models. While several testing programs have been previously conducted, these earlier validation studies did not integrate all the physics or components important in a modern, horizontal dry cask system.

A previous investigation produced data sets that can be used to benchmark the codes and best practices presently used to determine cladding temperatures and induced cooling air flows in modern horizontal dry storage systems. The horizontal dry cask simulator (HDCS) was designed to generate this benchmark data and add to the existing knowledge base. The objective of the previous HDCS investigation was to capture the dominant physics of a commercial dry storage system in a well-characterized test apparatus for a wide range of operational parameters. The close coupling between the thermal response of the canister system and the resulting induced cooling air flow rate was of particular importance. The previous investigation explored these parameters using helium backfill at 100 kPa and 800 kPa pressure as well as air backfill with a series of simulated decay heats. The helium tests simulated a horizontal dry cask storage system at normal storage conditions with either atmospheric or elevated backfill pressure, while the air tests simulated horizontal storage canisters following a complete loss of helium backfill, in which case the helium would be replaced by air.

The present HDCS investigation adds to the previous investigation by exploring steady-state conditions at various stages of the loss of helium backfill from a horizontal dry cask storage system. This is achieved by using helium/air blends as a backfill in the HDCS and running a series of tests using various simulated decay heats to explore the effects of relative helium/air molar concentration on the thermal response of a simulated horizontal dry cask storage system.

A total of twenty tests were conducted where the HDCS achieved steady state for various assembly powers, representative of decay heat. The power levels tested were 0.50, 1.00, 2.50, and 5.00 kW. All tests were run at 100 kPa vessel pressure. The backfill gases used in these tests are given in this report as a function of mole fraction of helium (He), balanced by air: 1.0, 0.9, 0.5, 0.1, and 0.0 He. Steady-state conditions (where the steady-state start condition is defined as where the change in temperature with respect to time for the majority of HDCS components is less than or equal to 0.3 K/h) were achieved for all test cases.

Figure E.1 shows the axial centerline fuel temperature profiles for all mole fractions of helium balanced by air explored in this study, for 5.00 kW power and 100 kPa pressure. The profile trends are similar across all mole fractions of helium, and as the mole fraction of helium in air decreases, the temperatures at all locations of the axial profile increase. In general, the axial, vertical, and horizontal temperature profiles presented in this report show that the effects of helium concentration were present primarily in the temperatures within the fuel assembly, with decreasing helium concentration leading to higher fuel assembly temperatures.

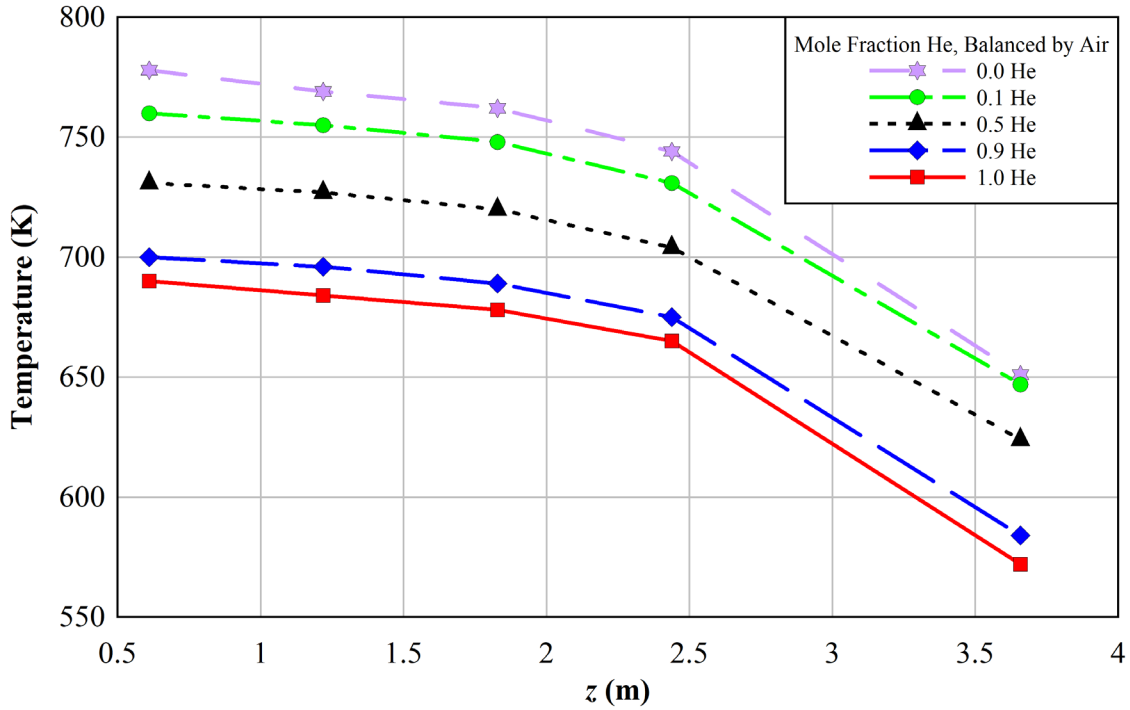

Figure E.1 Centerline fuel temperature profile as a function of *z* for 5.00 kW and all helium/air backfill compositions at 100 kPa.

The vertical and horizontal temperature profiles presented in this report show that the temperature differences between tests with varying helium/air concentrations for a given power were significant at the center of the fuel, but these differences reduced in magnitude at locations further away from the fuel center. The temperatures at the canister and the vault were largely similar across all tests for a given power.

Figure E.2 shows the canister axial temperature profiles for all mole fractions of helium in air considered in this report. The uncertainty bars are generated from the maximum uncertainty in temperature across the test series conducted at 5.00 kW and 100 kPa. This maximum uncertainty is the uncertainty in temperature from the air test (0.0 He), since the uncertainty is calculated as 1% of the peak cladding temperature (PCT) and the largest PCT in the 5.00 kW, 100 kPa test series was measured from the air test. As shown in the plot, the majority of temperatures at each canister axial location are largely similar, suggesting that changes in canister backfill gas that would result from a loss of helium backfill may be undetectable by measurement of the canister surface temperatures.

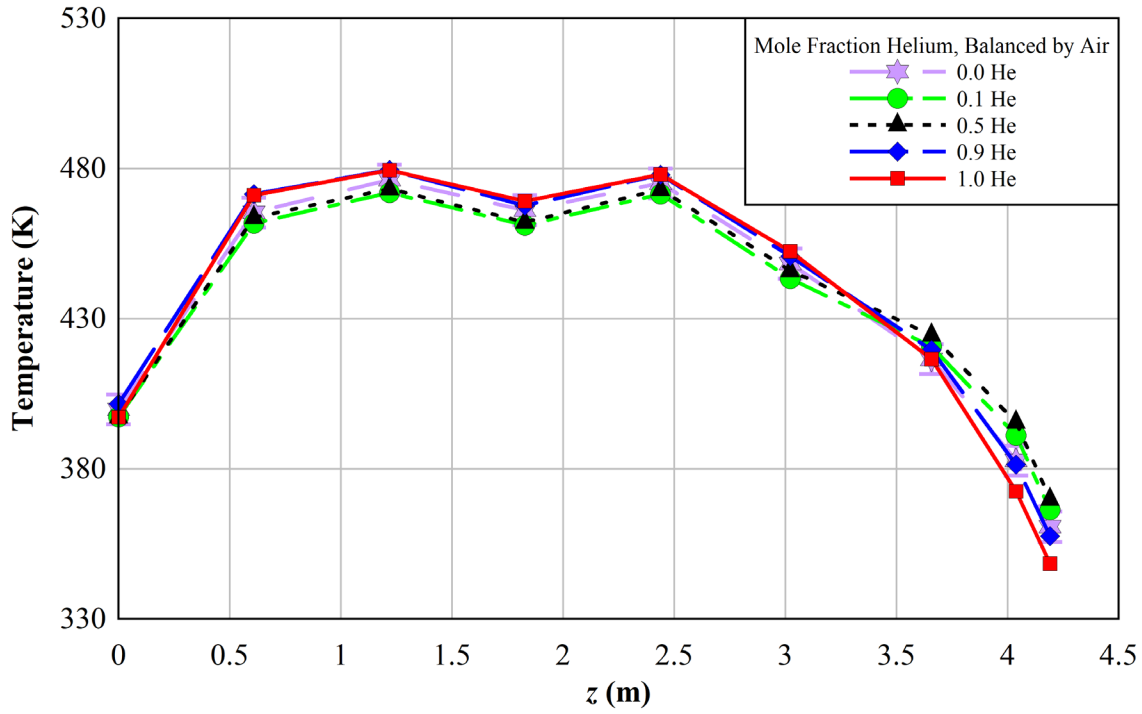

Figure E.2 Canister axial temperature profile for 5.00 kW and all helium/air backfill compositions at 100 kPa.

Further investigations into the consequences of a loss of helium backfill from a horizontal dry storage canister were carried out, which included comparisons of PCT, total air mass flow rate, canister/ambient temperature difference, and vault inlet/outlet temperature difference across tests with varying mole fractions of helium in air. These investigations revealed that total air mass flow rate and the temperature differences were independent of helium mole fraction in the canister. Changing the mole fractions of helium in air for a given power within the canister primarily affected the temperatures in the fuel assembly, including the peak cladding temperature. Decreasing helium concentration, representing a loss of helium backfill, lead to higher fuel assembly temperatures in the HDCS.

This page is intentionally left blank.

ACKNOWLEDGEMENTS

The authors would like to acknowledge the hard work and commitment of all contributors to the project. In particular, we would like to acknowledge the strong support and leadership of Ned Larson at the Department of Energy. Sylvia Saltzstein (8845) and Geoff Freeze (8843) are to be commended for their programmatic and technical guidance.

The authors would also like to thank Greg Koenig, Adrian Perales, and Beau Baigas of 8843 for their tireless efforts and dedication to service, which made the success of this project possible.

This page is intentionally left blank.

CONTENTS

LIST OF FIGURES

This page is intentionally left blank.

LIST OF TABLES

ACRONYMS / ABBREVIATIONS

BR	blockage ratio
BWR	boiling water reactor
CFD	computational fluid dynamics
CYBL	Cylindrical Boiling
DCS	Dry Cask Simulator
DOE	Department of Energy
DSC	dry storage canister
HDCS	Horizontal Dry Cask Simulator
HSM	horizontal storage module
MAWP	maximum allowable working pressure
NE	Nuclear Energy
NRC	Nuclear Regulatory Commission
PCT	peak cladding temperature
PWR	pressurized water reactor
SCC	stress corrosion crack
SFWD	Spent Fuel and Waste Disposition
TC	thermocouple

This page is intentionally left blank.

INVESTIGATION OF THERMAL-HYDRAULIC EFFECTS OF DRY STORAGE CANISTER HELIUM BACKFILL LOSS USING THE HORIZONTAL DRY CASK SIMULATOR

This report fulfills milestone M2SF-21SN010203032 (Thermal-Hydraulic Effects of Loss of Helium Backfill Using the HDCS) in the Spent Fuel and Waste Science and Technology work package (SF-21SN01020303). This work was sponsored under the Department of Energy's (DOE) Office of Nuclear Energy (NE) Spent Fuel and Waste Disposition (SFWD) campaign.

1 INTRODUCTION

The performance of commercial spent nuclear fuel dry storage casks is typically evaluated through detailed analytical modeling of the system's thermal performance. These modeling efforts are performed by the vendor to demonstrate both performance and regulatory compliance and are independently verified by the Nuclear Regulatory Commission (NRC). The thermal profiles and peak cladding temperatures in a dry storage system are of high importance in addressing knowledge gaps associated with spent nuclear fuel degradation mechanisms, most of which are temperature dependent with degradation rates generally increasing with temperature [Hanson *et al*., 2012; Saltzstein *et al*., 2020].

The majority of commercial dry storage casks currently in use are aboveground in both horizontal and vertical orientations. Figure 1.1 shows a diagram for a typical horizontal system. Cooling of the assemblies located inside the sealed canister, which is typically backfilled with helium, is enhanced by the induced flow of air drawn through the bottom air inlet and exiting out the top air outlet.

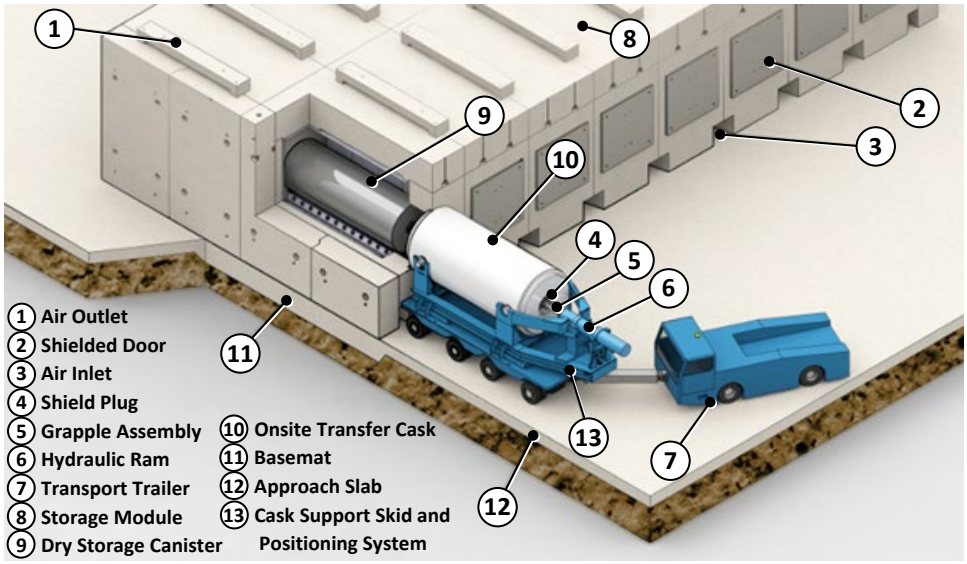

Source: http://us.areva.com/EN/home-3138/areva-nuclear-materials-tn-americas--nuhoms-used-fuel-storage-system.html#tab=tab6

Figure 1.1 Horizontal dry storage system.

This passively cooled design allows dust from the environment into the system. These particulates may then collect on the surfaces of the canister. As the spent nuclear fuel cools, salts contained in the dust may deliquesce in the presence of moisture from the ambient relative humidity to form concentrated brines, which may contain corrosive species such as chlorides. These species can cause localized corrosion, called pitting. With sufficient stresses, these pits can evolve into stress corrosion cracks (SCCs), which

could penetrate through the canister wall and allow communication from the interior of the canister to the external environment [Schindelholz, 2017]. It is therefore imperative to understand the potential thermal-hydraulic effects of this communication, which in a worst-case scenario would result in the loss of helium backfill from the canister and the subsequent replacement of helium with air.

Carefully measured data sets generated from testing of full-sized casks or smaller cask analogs are widely recognized as vital for validating design and performance models. Numerous studies using these cask or cask analogs for validation purposes have been previously conducted [Bates, 1986; Dziadosz *et al.*, 1986; Irino *et al.*, 1987; McKinnon *et al.*,1986]. Recent advances in dry storage cask designs have significantly increased the maximum thermal load in a canister in part by improving the efficiency of internal conduction pathways and by enhancing internal convection through greater canister helium pressure. Horizontal, canistered cask systems rely on ventilation between the canister and the vault walls to convect heat away from the canister to the surrounding environment. While several testing programs have been previously conducted, these earlier validation attempts did not integrate all of the physics or components important in modern horizontal dry cask systems. Thus, the enhanced performance of modern horizontal dry storage systems cannot be fully validated using previous studies.

1.1 Objective

The purpose of the investigation described in this report is to document new data sets from the horizontal dry cask simulator (HDCS) that can be used to benchmark the codes and best practices presently used to determine cladding temperatures and induced cooling air flows in modern horizontal dry storage systems. The new data sets presented in this report are from tests using helium/air blends as canister backfill gases. These data sets complement the existing database that was presented in the HDCS update report [Lindgren *et al*., 2019] and the HDCS blind model validation report [Pulido *et al*., 2020b] by simulating various stages of loss of helium backfill from a horizontal storage canister and quantifying the resulting thermal response and induced air flow.

1.2 Previous Studies

1.2.1 Small Scale, Single Assembly

Two single assembly investigations were documented in the mid-1980s [Bates, 1986; Irino *et al.*, 1987]. Both included electrically heated 15×15 pressurized water reactor (PWR) assemblies with thermocouples (TCs) installed to directly measure the surface temperature of the cladding. In Bates (1986), the electrically heated assembly was instrumented with fifty-seven TCs distributed over seven axial levels. In Irino *et al.* (1987), the electrically heated assembly was instrumented with ninety-two TCs distributed over four axial levels. In Bates (1986), a single irradiated 15×15 PWR assembly was also studied using 105 TCs distributed equally into each of the fifteen guide tubes at seven axial levels. All testing included a horizontal orientation using helium or air at one atmosphere but imposed a constant temperature boundary condition on the outer cask wall in order to obtain prototypic storage temperatures in the fuel assembly bundle. None of these tests incorporated the naturally convective cooling by induced air flow inside of vault-like enclosures.

The natural convection heat transfer mechanisms in an enclosed horizontal rod bundle were investigated in a study aimed at obtaining convection correlations that could be applied to analytical models [Canaan and Klein, 1996]. The correlations focused on the Nusselt number, defined in terms of the maximum and average fuel assembly temperatures. Canaan and Klein, through experimental testing, claimed the presence of both conduction and convection regimes based on the Rayleigh number of the flow within the horizontal rod bundle enclosure. Predictions of maximum assembly temperatures were made using the Nusselt number correlations. The experimental setup included materials thermally equivalent to spent nuclear fuel, and heater rods simulated spent fuel decay heat. Thermocouples were installed within two concentric cylindrical steel shells to avoid wires external to the heater rods that may interfere with the flow within the fuel assembly. Although this study maintained geometrically-prototypic dimensions of a

boiling water reactor (BWR) assembly in a two-dimensional cross section, only a partial axial length was tested, so the setup was not geometrically prototypic in the axial direction. Additionally, the channel box was maintained as a constant temperature heat sink at 300 K and served as the boundary condition, which is not representative of a prototypic channel box which would most likely heat up beyond 300 K. The setup also did not include all of the components of a full horizontal storage module; for example, the basket, canister, and vault enclosure were missing. The study used heater rod powers per unit length of 1 to 7 W/m, pressures ranging from 101.3 to 514.8 kPa, and backfills of helium and nitrogen. The use of nitrogen was meant to simulate an alternative backfill gas used in the transportation of spent fuel and is not representative of a loss of helium backfill.

In a recent investigation [Durbin and Lindgren, 2018], an existing electrically heated and Incoloy-clad but otherwise prototypic BWR test assembly was deployed inside of a representative storage basket and cylindrical pressure vessel that represents a vertical canister system. The symmetric single assembly geometry with well-controlled boundary conditions simplified interpretation of results. Two different arrangements of ducting were used to mimic conditions for aboveground and belowground storage configurations for vertical, dry cask systems with canisters. Transverse and axial temperature profiles were measured throughout the test assembly. The induced air mass flow rate was measured for both the aboveground and belowground configurations. In addition, the impact of cross-wind conditions on the belowground configuration was quantified.

Over 40 unique data sets were collected and analyzed for this effort. Fourteen data sets for the aboveground configuration were recorded for powers and internal pressures ranging from 0.5 to 5.0 kW and 0.3 to 800 kPa absolute, respectively. Similarly, fourteen data sets were recorded for the belowground configuration starting at ambient conditions and concluding with thermal-hydraulic steady state. Over thirteen tests were conducted using a custom-built wind machine. The results documented in the BWR dry cask simulator (DCS) test report [Durbin and Lindgren, 2018] highlight a small, but representative, subset of the available data from this test series.

Data sets from the vertically oriented dry cask simulator were used in a model validation activity [Pulido *et al.*, 2020a]. In this study, a model validation exercise was carried out using the data obtained from dry cask simulator testing in the vertical, aboveground configuration. Five modeling institutions – the U.S. NRC, Pacific Northwest National Laboratory (PNNL), Centro de Investigaciones Energéticas, MedioAmbientales y Tecnológicas (CIEMAT), and Empresa Nacional del Uranio, S.A., S.M.E. (ENUSA) in collaboration with Universidad Politécnica de Madrid (UPM) – were granted access to the input parameters from SAND2017-13058R, "Materials and Dimensional Reference Handbook for the Boiling Water Reactor Dry Cask Simulator" [Lindgren *et al*., 2017], and results from the vertical aboveground BWR dry cask simulator tests reported in NUREG/CR-7250, "Thermal-Hydraulic Experiments Using a Dry Cask Simulator" [Durbin and Lindgren, 2018]. With this information, each institution was tasked to calculate minimum, average, and maximum fuel axial temperature profiles for the fuel region as well as the axial temperature profiles of the DCS structures. Transverse temperature profiles and air mass flow rates within the dry cask simulator were also calculated. These calculations were done using modeling codes (ANSYS FLUENT, STAR-CCM+, or COBRA-SFS), each with their own unique combination of modeling assumptions and boundary conditions. For this validation study, four test cases of the vertical, aboveground dry cask simulator were considered, defined by two independent variables – either 0.5 kW or 5 kW fuel assembly decay heat, and either 100 kPa or 800 kPa internal helium pressure. However, this model validation activity was not fully blind in that all the modeling participants had access to complete data sets.

The DCS was moved to a horizontal configuration and an insulated sheet metal enclosure that simulates a concrete vault was built around the simulator to create the HDCS, as documented in the HDCS update report [Lindgren *et al*., 2019]. Axial and transverse temperatures as well as inlet duct air mass flow rates were measured for the dry cask simulator in the horizontal configuration for a range of simulated decay heats (0.5, 1.0, 2.5, and 5.0 kW), and for atmospheric (100 kPa) and elevated (800 kPa) pressures. In total,

ten test cases were explored, but data sets from two of the ten test cases (one helium case and one air case) were provided in the HDCS update report. The investigation found that the steady-state peak cladding temperatures for the components located inside the pressure vessel representing the canister were lower for the reported helium backfill case than for the reported air backfill case. The vertical and horizontal temperature profiles both indicate that the temperature gradients between the components inside the pressure vessel were lower for the helium case than for the air case.

The limited data set from the two test cases highlighted in the HDCS update report as well as the input parameters from the DCS Handbook [Lindgren and Durbin, 2017] were provided to three modeling institutions – the U.S. NRC, PNNL, and ENUSA – for model calibration in a blind modeling validation exercise [Pulido *et al*., 2020b]. In this exercise, data from the eight test cases not presented in the HDCS update report were purposely withheld from the modeling institutions – the only information given from those eight tests were the input parameters of power (representing decay heat), pressure, and ambient temperature. Peak cladding temperatures, axial and transverse temperature profiles, and air mass flow rates were used as comparison metrics, and root mean squares of the normalized errors between experimental and model results were calculated to quantify the goodness of fit of the model results to the experimental data. A more detailed comparison was made using uncertainty quantification for one of the models. A model validation criterion was established by dividing the root mean square of the normalized errors by the validation uncertainty, and it was determined that this model satisfies the model validation criterion, demonstrating the efficacy of codes in predicting the thermal response of a horizontal dry cask storage system.

1.2.2 Full Scale, Multi Assembly

Several full-scale, multi-assembly cask studies were also documented in the mid-1980s to early 1990s – one for a BWR cask with unconsolidated fuel assemblies [McKinnon *et al*., 1986] and the others for PWR casks with both consolidated and unconsolidated fuel [Dziadosz *et al*., 1986; McKinnon *et al*., 1987; Creer *et al*., 1987; McKinnon *et al*.,1989; Strope *et al*., 1990]. Only in the most recent study was a ventilated horizontal cask design tested. In all studies the cask or canister was studied with internal atmospheres ranging from vacuum up to 150 kPa using air, nitrogen, or helium.

1.2.2.1 Unventilated

In the first study [McKinnon *et al*., 1986], twenty-eight or fifty-two BWR assemblies with a total heat load of 9 or 15 kW, respectively, were contained in a REA 2023 prototype steel-lead-steel cask with a water-glycol neutron shield. Thirty-eight TCs were installed on the cask interior. Twenty-four of those were installed in direct contact with the center rod in seven assemblies at up to seven different elevations. Twelve were installed on the basket at three different elevations. Two TCs were installed in direct contact with a fuel rod located on the center outer face of an assembly. The cask was tested in an open environment in both a vertical and horizontal orientation with internal atmospheres of vacuum or nitrogen at 145 kPa (21.0 psia) average or helium at 152 kPa (22 psia) average.

In the earliest full-scale PWR cask study [Dziadosz *et al*., 1986], twenty-one PWR assemblies with a total heat load of 28 kW were contained in a Castor-V/21 cast iron/graphite cask with polyethylene rod neutron shielding. The interior of the cask was instrumented with sixty TCs deployed on ten lances located in eight guide tubes and two basket void spaces. Two of the assembly lances were installed into the center assembly. Note that with the use of TC lances inside of the assembly guide tubes, no direct fuel cladding temperatures were measured. The cask was tested in an open environment in both a vertical and horizontal orientation with internal atmospheres of vacuum or nitrogen at 57 kPa or helium at 52 kPa.

A relatively low total heat load of 12.6 kW was tested in a Westinghouse MC-10 cask with twenty-four PWR assemblies [McKinnon *et al*., 1987]. The MC-10 has a forged steel body and distinctive vertical carbon steel heat transfer fins around the outer circumference. The outer surface of the cask was instrumented with thirty-four TCs. The interior of the cask was instrumented with fifty-four TCs deployed

on nine TC lances in seven fuel assembly guide tubes and two basket void spaces. The cask was tested in an open environment in both a vertical and horizontal orientation and the interior atmosphere was either a vacuum or 150 kPa helium or air.

A pair of studies using the same TN-24 cask was tested with twenty-four PWR assemblies with 20.5 kW total output [Creer *et al*., 1987] or twenty-four consolidated fuel canisters with 23 kW total output [McKinnon *et al*., 1989]. The TN-24P has a forged steel body surrounded by a resin layer for neutron shielding. The resin layer is covered by a smooth steel outer shell. The TN-24P is a prototype version of the standard TN-24 cask with differences in the cask body thickness, basket material and neutron shield structure. The TN-24P also incorporates fourteen TCs into the basket structure. In either study, the fuel was instrumented with nine TC lances with six TCs per lance, seven in fuel guide tubes and two in simulated guide tubes in basket void spaces. The outside surface was instrumented with thirty-five TCs in the unconsolidated fuel study [Creer *et al*., 1987] and twenty-seven TCs in the consolidated fuel study [McKinnon *et al*.,1989]. In both studies the cask was tested in an open environment in both vertical and horizontal orientations with the interior atmosphere as either a vacuum or 150 kPa helium or air. A seventh test was conducted in the consolidated fuel study [McKinnon *et al*., 1989] for a horizontal orientation under vacuum with insulated ends to simulate impact limiters.

None of the previous studies discussed so far included or accounted for ventilation inside of a horizontal cask or vault. The three single assembly investigations that were carried out prior to the dry cask simulator studies and that included a horizontal orientation imposed constant temperature boundary conditions [Bates, 1986; Irino *et al.*, 1987; Canaan and Klein, 1996]. The four full scale cask studies [Dziadosz *et al*., 1986; McKinnon *et al*., 1987; Creer *et al*., 1987; McKinnon *et al*.,1989] only considered cask designs externally cooled in an open environment.

1.2.2.2 Ventilated

Performance testing of a commercial NUHOMS-07P horizontal PWR spent fuel storage system was conducted in the mid to late 1980s [Strope *et al*., 1990]. The NUHOMS-07P horizontal PWR spent fuel storage system is an early, much smaller version of modern horizontal systems in common use today. The system consists of a stainless steel dry storage canister (DSC) with a welded closure that is housed in a concrete vault, or horizontal storage module (HSM). Ventilation inlets and outlets in the HSM induce air flow over and around the DSC to passively remove heat. Eight NUHOMS-07P systems were constructed and loaded under a site-specific license for use at Duke Energy's H.B. Robinson independent spent fuel storage installation (ISFSI). Each unit stores seven 15×15 PWR assemblies. When the first three systems were fabricated, two of the vaults were instrumented with fifty-four type-J TCs, and two canisters were instrumented with twenty-five TCs each. Prior to loading with fuel, two test series were conducted using electric heaters to simulate the fuel. A single Chromalox Calrod was deployed in the center of each of the seven fuel basket tubes. Other than inputting the desired heat, the heater rod did not hydraulically or thermally simulate the prototypic nature of a spent fuel assembly.

The first test series was conducted with an instrumented DSC inside of an IF-300 spent fuel transportation cask. In this test series, temperatures were measured while the DSC, with heater rods, was flooded with water, vacuum dried, and backfilled with helium. No mock fuel assemblies were occupying any of the storage cells (referred to as fuel sleeves in the report), but five TC spears were located in the center of most storage cells. The seven heater rods were powered at 1 kW each for a total of 7 kW in the DSC. The maximum temperatures reported (during vacuum drying) was 255 °C for the top of the center fuel sleeve wall and 288 °C for the center of the empty center fuel sleeve.

The next test series was conducted with the electrically heated DSC located in the instrumented HSM. Under normal operation with a total DSC power of 7 kW, the maximum temperature reported was 201 °C for a fuel sleeve wall and 241 °C for the empty fuel sleeve centerline. Blocking the HSM air inlets and outlets increased these peak temperatures to 225 °C and 264 °C respectively. Increasing the total power

from 7 kW to 13 kW increased the fuel sleeve temperature to 291 °C and the empty sleeve centerline to 340 °C. Decreasing the power to 2.2 kW decreased these temperatures to 116 °C and 142 °C respectively.

For the final test series, the heater rods were removed and the dry canisters were loaded with nominally 5 kW of actual spent nuclear fuel. Unfortunately, when the spent fuel assemblies were loaded many of the TCs in the DSC were damaged. Only one TC spear that measured the upper fuel assembly centerline temperature survived. With all three HSMs loaded with spent fuel, the maximum fuel sleeve wall temperature was 156 °C and the maximum fuel temperature in the upper horizontal assembly was 180 °C.

Throughout the second and third test series conducted using an HSM, attempts were made to measure the flow of air into the HSM air inlet. Unfortunately, the data was found to be erratic and judged to be unreliable. The data from the air velocity measurements were not used in the evaluation. The usefulness of the performance data for model validation purposes is seriously compromised by the limited temperature data and the absence of the air flow data.

1.2.3 Uniqueness of Present Test Series

The present investigation uses a simplified, well-characterized single-assembly test apparatus that integrates the dominant physics in prototypic systems. This approach differs from previous studies in several major respects. Principal among these is that the ventilated boundary conditions for a horizontal configuration are explicitly considered. Accurate induced air flow rates were measured using the successful approach used in previous studies [Durbin and Lindgren, 2018]. Rather than striving to achieve prototypic peak clad temperatures by artificially imposing a temperature boundary condition on the canister wall, the present study incorporates relevant physics by including realistic boundary conditions.

Additionally, the apparatus contained a hydraulically and thermally prototypic mock assembly that can accommodate elevated pressures. The pressure vessel allowed testing at prototypic pressures of 100 and 800 kPa. Testing at a higher pressure was conducted in order to experimentally quantify the contribution of convection and evaluate the assumption that convective heat transfer inside the canister is negligible.

As was the case in the previous vertical DCS studies [Durbin and Lindgren, 2018] a scaling distortion in simulated assembly power is necessary to more closely match the thermal-hydraulic response of a full-sized spent fuel storage cask. This need for additional decay heat is reasonable given the higher external surface-area-to-volume ratio of a single assembly arrangement as in the HDCS compared to a modern canister with up to eighty-nine assemblies.

The HDCS update report [Lindgren *et al*. 2019] presented data from two of the ten previously run HDCS test cases using helium and air backfill gases, while the HDCS model validation report presented data from the other eight test cases as well as comparisons of this data to modeling results. The uniqueness of the present investigation is found in the new data presented in this report that focuses on the use of helium/air blends as backfill gases in the HDCS. These blends simulate various stages of the loss of helium backfill from a horizontal dry storage canister, and the measurements taken capture the thermal-hydraulic effects of this helium backfill loss.

2 APPARATUS AND PROCEDURES

2.1 General Construction

The core of the vertical dry cask simulator used in previous studies [Durbin and Lindgren, 2018] was modified for configuration to a horizontal orientation, as shown in Figure 2.1. The general design details with the required support modifications are shown in Figure 2.2. As was the case for the vertical DCS, an existing electrically heated and Incoloy-clad but otherwise prototypic 9×9 BWR test assembly was deployed inside of a representative storage basket and cylindrical pressure vessel that represents the canister. The pressure vessel representing the canister has been designed, fabricated, and pressure tested for a maximum allowable working pressure (MAWP) rating of 2,400 kPa at 400 °C. Transverse and axial temperature profiles (using TCs detailed in Section 2.4.1) as well as induced cooling air flow rates (using hotwire anemometers detailed in Section 2.4.4) have been measured for a wide range of decay power and canister pressures using helium/air blends as backfill gases and compared to the temperature profiles and air flow rates obtained using helium and air backfills, as detailed in Section 2.6.

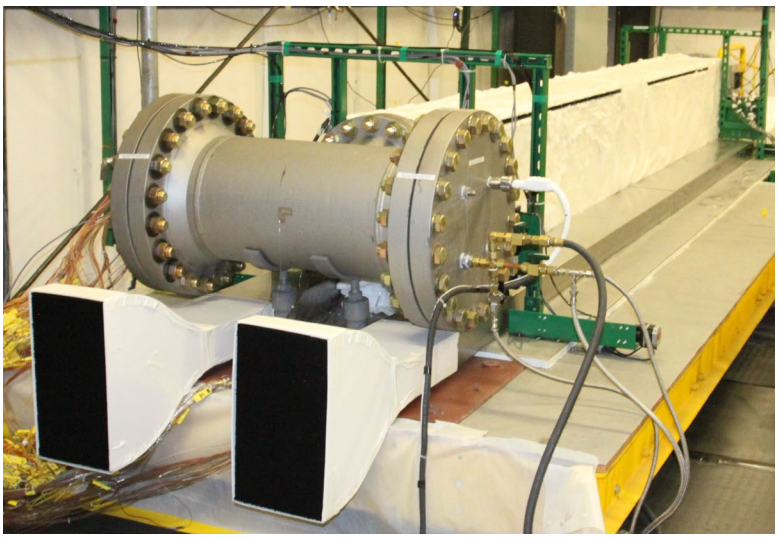

Figure 2.1 Photo of the HDCS system.

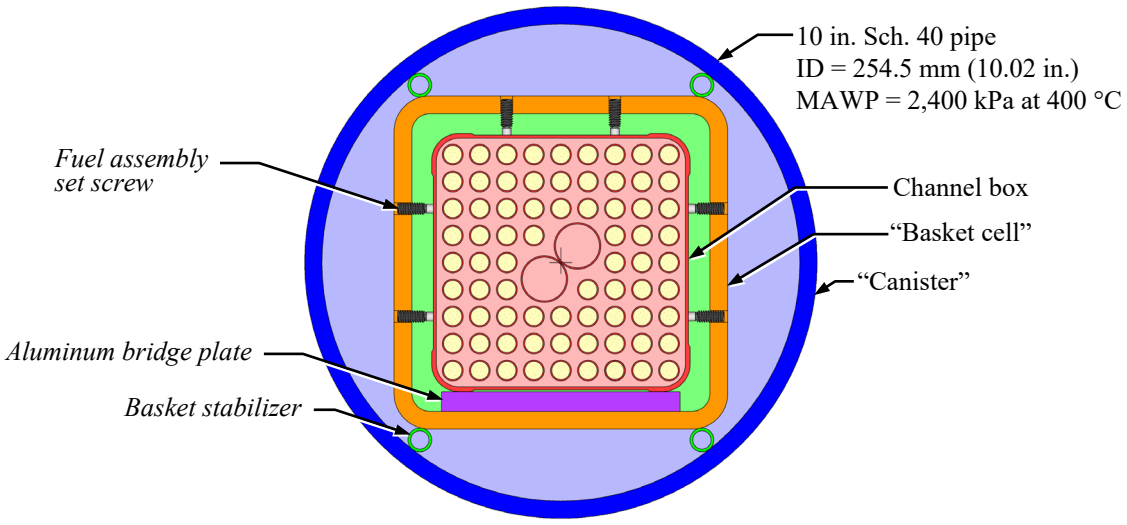

Figure 2.2 General design details of the dry cask simulator with *modifications*.

In prototypic horizontal systems, the assemblies are free to make direct contact with the bottom face of the basket. Due to existing mechanical fixturing and instrumentation at the fuel assembly base, the HDCS assembly used in this study is not free to make direct contact with the basket and must maintain concentricity to avoid damage during reorientation to a horizontal configuration. Therefore, a full-length aluminum (alloy 6061) bridge plate (127 mm (5 in.) wide and 9.6 mm (0.378 in.) thick) was installed between the assembly channel box and the inside face of the basket to establish a conductive pathway and maintain concentric spacing of the assembly. Set screws were also installed through the basket on the other three sides to center and stabilize the channel box. Geometric details of the contact between the aluminum plate and the channel box are shown in the HDCS update report [Lindgren *et al.*, 2019]. There is limited contact between the corners of the channel box and the aluminum bridge plate. Of the 127 mm width of the bridge plate, only a total of 13.4 mm (0.528 in.) makes contact with the channel box shoulders and the center 97 mm (3.82 in.) is separated by a 0.9 mm (0.0354 in.) gas gap.

Full-length stabilizing tubes along the corners of the basket provided limited conductive paths between the basket and the pressure vessel while keeping the basket centered in the pressure vessel and limiting convective cells as shown in Figure 2.3. The stainless steel 304 tubes had an outer diameter of 12.7 mm (0.500 in.) and wall thickness of 1.59 mm (0.0625 in.). The tubes were stitch welded to the basket at 0.61 m (24 in.) intervals from the basket bottom to the top. These stitch welds had a nominal length of 25.4 mm (1.00 in.). Once the pressure vessel was installed, these stabilizer tubes formed line contacts on both the basket and the pressure vessel.

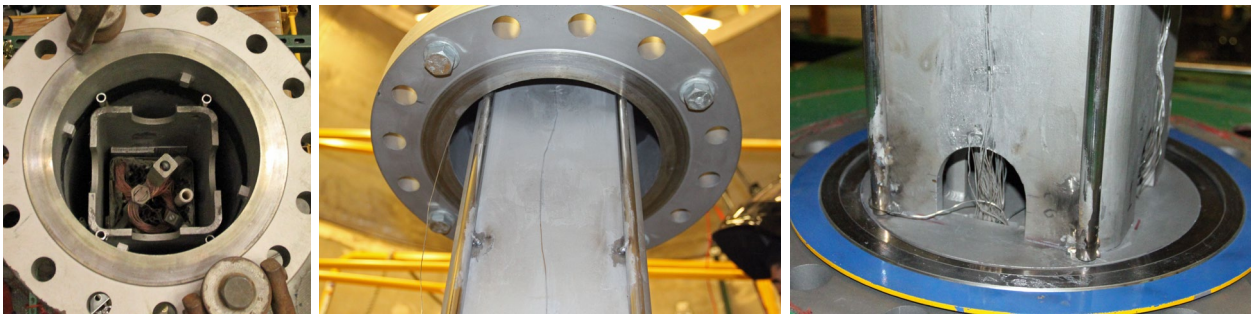

Top View **Middle View** **Bottom View**

Figure 2.3 Photographs of the test assembly showing the basket stabilizer rods.

The horizontal test apparatus is enclosed in an insulated stainless-steel sheet metal enclosure that simulates the concrete vault as shown partially exploded in Figure 2.4 and described in detail in Section 2.2. The vault is comprised of 11-gauge stainless steel sheet metal components. Three side ribs on each side support two side panels and two top panels. Panels on each end enclose the pressure vessel pipe. Inlet and outlet vents to the vault enclosure are located on the top and bottom of each of the four side panels. The vault inlets are supplied by rectangular ducts in which the induced flow is measured using hot wire anemometers. Because the induced flow for the HDCS is expected to be similar to that measured in the aboveground vertical DCS study, the inlet ducts are designed to be the same size. The flow area of the vault inlet and outlet vents also match the flow area of the inlet ducts. The exterior of the sheet metal is covered with a thin layer of insulation (not shown) to mimic the thermal resistance of the walls in a commercial concrete vault (see Section 2.2 for details).

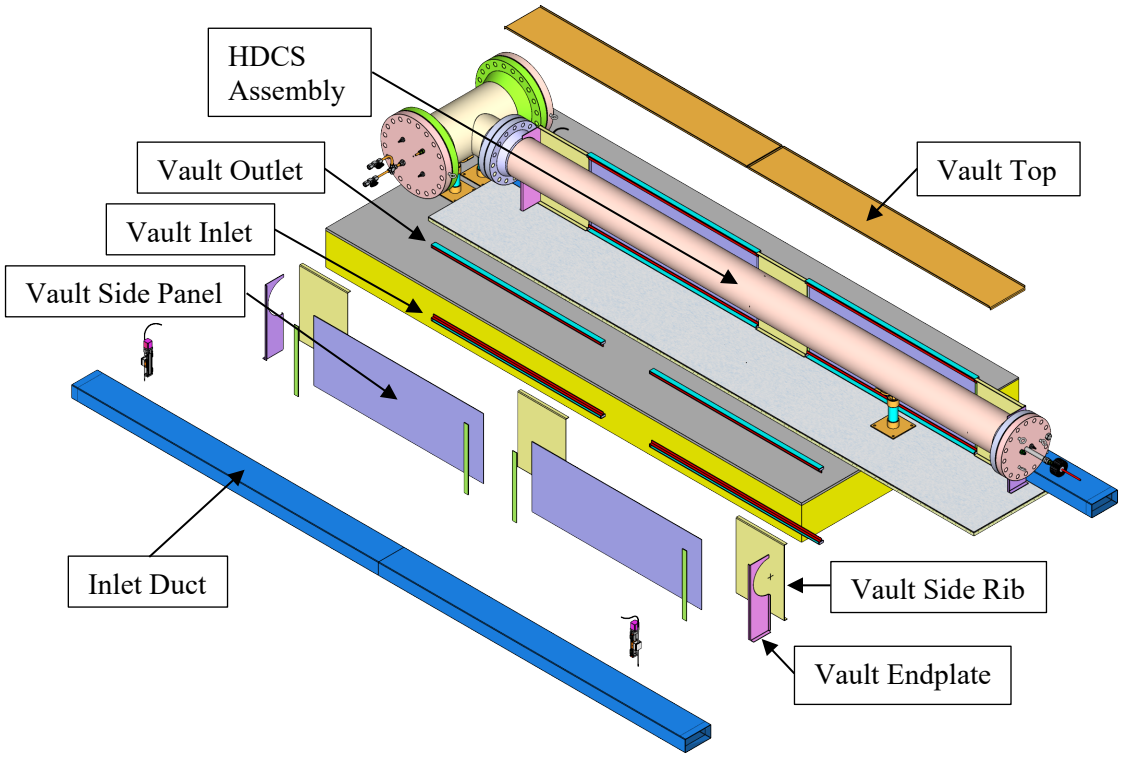

Figure 2.4 HDCS and partially exploded sheet metal vault components.

The new test configuration was assembled and operated inside of the Cylindrical Boiling (CYBL) test facility, which is the same facility used for earlier fuel assembly studies [Lindgren and Durbin, 2013; Durbin and Lindgren, 2018]. The apparatus was lifted out of the CYBL vessel and rotated to a horizontal orientation on a platform on the third (top) floor of the CYBL building. Figure 2.5 shows a scaled diagram of the CYBL facility with the DCS inside. The stainless-steel vault enclosure was assembled around the pressure vessel after it was laid in the horizontal position.

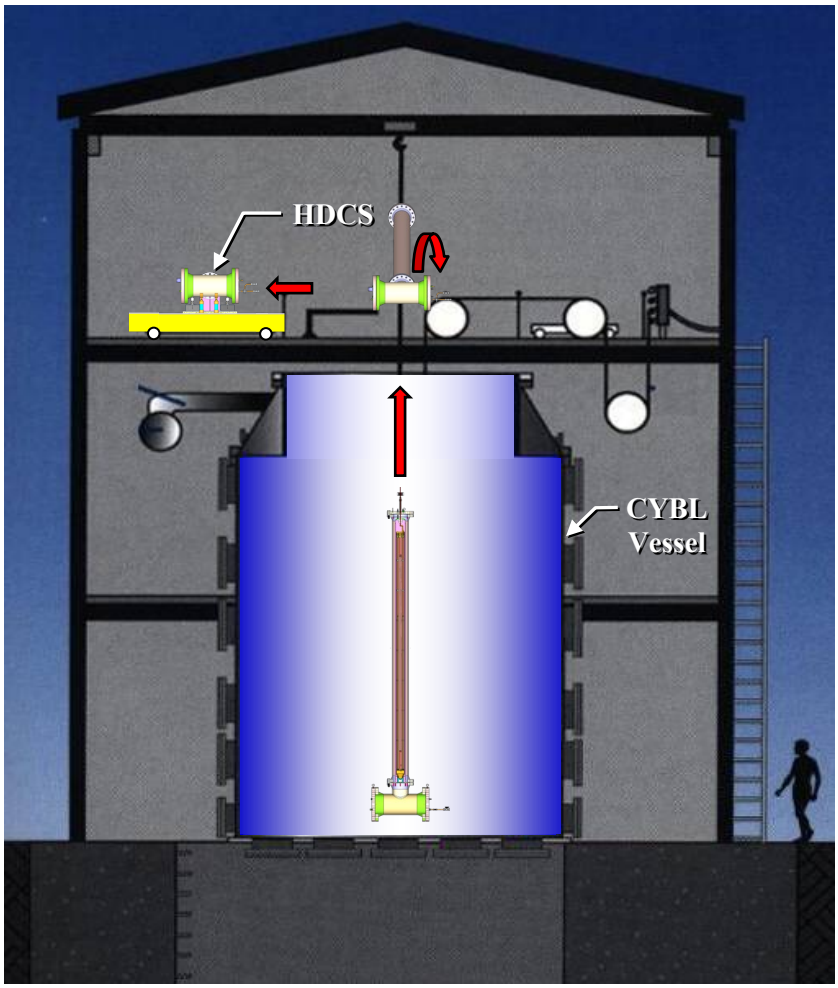

Figure 2.5 CYBL facility housing dry cask simulator testing.

2.2 Design of Vault

The HDCS enclosure was scaled to a NUHOMS HSM Model 80 and Model 102 vault containing a NUHOMS 61BT canister by the blockage ratio (BR). This ratio is defined as the ratio of the diameter of the canister to the inside width of the vault as shown in Figure 2.6. For design purposes, the air mass flow rate for the HDCS was assumed from values measured during similar, vertical test conditions [Durbin and Lindgren, 2018]. This assumption was justified by observing the comparability in the air mass flows calculated by the modeling of two prototypic systems. The systems considered were the NUHOMS HSM (0.25 kg/s), which is in a horizontal configuration, and the Holtec HI-STORM 100 (0.32 kg/s), which is in a vertical configuration; the calculations were carried out using computational fluid dynamics [Solis and Zigh, 2015]. Thus, the inlets and outlets to the vault enclosure were designed to have a flow area that matched the aboveground, vertical DCS apparatus. As with the aboveground vertical case, the HDCS had four inlet ducts each with inside dimensions of 0.102 m (4.02 in.) by 0.229 m (9.02 in.) and air velocity anemometers were used to measure the inlet air flow rate. Computer-controlled stages were used to automatically traverse across the inlet opening to measure the flow field.

A simple analysis using one-dimensional thermal resistances for combined heat transfer was performed for the vault side walls and top of an HSM and the HDCS. This analysis showed that the combined thermal resistance of the HSM vault from the heat shield to the outside of the concrete wall was equivalent to the stainless steel HDCS vault wall backed with 6.4 mm (0.25 in.) of high-temperature,

alumina-silica insulation. Thus, the analysis includes the effects of the heat shield from radiation and convection. The equivalency of a relatively thin layer of insulation to 0.51 m (20 in.) of reinforced concrete with a heat shield may be realized in large part because the thermal conductivity of the insulation is roughly 30 times less than that of the concrete. Therefore, the two systems will lose thermal energy through the vault walls at the same rate for the same temperature on the HSM heat shield as on the HDCS vault interior wall.

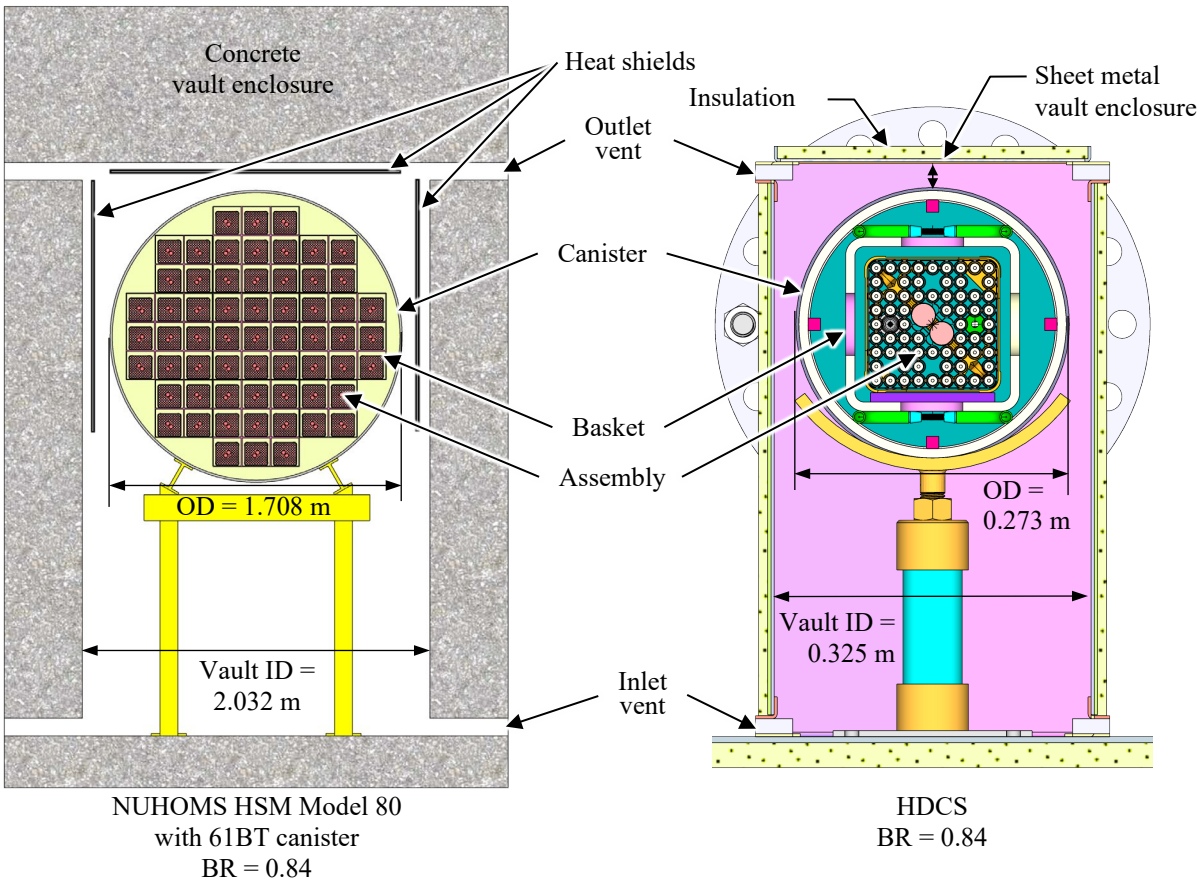

Figure 2.6 Cross sections of a NUHOMS HSM Model 80 and the Horizontal Dry Cask Simulator.

Table 2.1 gives the key parameters for the HDCS at two simulated decay heats and a commercial horizontal storage system. As in previous studies [Durbin and Lindgren, 2018], a known scaling distortion in simulated assembly power is necessary to more closely match the thermal-hydraulic response of a full-sized spent fuel storage cask. This need for additional decay heat is reasonable given the higher external surface-area-to-volume ratio of a single-assembly arrangement as in the HDCS compared to a modern canister with up to eighty-nine assemblies. The average velocity, U_{avg}, is calculated by assuming uniform air flow in the vault below the canister. The characteristic length for convection was defined as the canister height from previous vertical testing with the DCS assembly and matched well with vertical, commercial systems. For the current testing in a horizontal configuration, the characteristic length is defined by the outer canister diameter, $D_{canister}$. The significant difference between the HDCS and the commercial canister diameters introduces additional scaling distortions as described next by dimensional analyses.

Table 2.1 Comparison of key dimensional quantities for the HDCS and commercial systems.

Parameter	HDCS		Cask
Power (W)	500	5,000	24,000
$\dot{m}_{Air}$ (kg/s)	0.026	0.069	0.251
$D_{canister}$ (m)	0.273	0.273	1.708
U_{avg} (m/s)	0.019	0.049	0.021

Table 2.2 gives the critical dimensionless groups of the HDCS and a commercial system, namely Reynolds, modified Rayleigh, and Nusselt numbers. As previously noted, the disparity in the canister diameters causes scaling distortions. However, closer examination of the Reynolds numbers indicates that the HDCS and commercial canisters do share the same flow regime. This irregular regime is generally defined for cylinders with $270 < Re_D < 5{,}000$ and is characterized by irregular shedding of von Kármán vortex streets in the cylinder wake. For $Re_D < 1{,}000$ in the irregular regime, the vortices in the near-wake exhibit laminar behavior whereas turbulent dissipation is observed in these vortices for $Re_D > 1{,}000$ [Noack, 1999]. The impact of this difference is expected to be mitigated by the proximity of the vault walls and ceiling.

The modified Rayleigh number is preferred for these analyses because the canister boundary condition is more closely approximated by a uniform heat flux than an isothermal wall temperature. Three-dimensional separation of the cylinder wake defines the onset of the transition to turbulence. Visualization experiments have shown that this important transition occurs when the modified Rayleigh number exceeds 3.5×10^9 [Misumi *et al.*, 2003]. Therefore, the highest power planned for HDCS tests will be transitional if not turbulent as in a commercial system. Power-law fits of Nusselt number to the Rayleigh number are a common treatment for cylinders. Sparrow and Pfeil [Sparrow and Pfeil, 1984] offer a series of correlations for symmetrically confined cylinders between vertical walls. These Nusselt numbers for confined cylinders are within an order of magnitude of each other.

Table 2.2 Comparison of dimensionless groups for the HDCS and commercial systems.

Dimensionless Group	HDCS		Cask
Power (W)	500	5,000	24,000
Re_D	280	730	2,000
Ra_D^*	1.3×10^9	1.3×10^{10}	1.4×10^{13}
$Nu_{D,\ Confined}$	30	50	170

2.3 Details of the Heated Fuel Bundle

The highly prototypic fuel assembly was modeled after a 9×9 BWR. Commercial components were purchased to create the assembly including the top and bottom tie plates, spacers, water rods, channel box, and all related assembly hardware (see Figure 2.7). Incoloy heater rods were substituted for the fuel rods for heated testing. Due to fabrication constraints, the diameter of the Incoloy heaters was slightly smaller than prototypic rods, 10.9 mm (0.430 in.) versus 11.2 mm (0.440 in.). The slightly simplified Incoloy mock fuel rods were fabricated based on drawings and physical examples from the nuclear component supplier. The dimensions of the assembly components are listed in Table 2.3. The assembly was hydraulically characterized in a previous study [Lindgren and Durbin, 2013].

Table 2.3 Dimensions of assembly components in the mock 9×9 BWR.

Description	Lower (Full) Section	Upper (Partial) Section
Number of rods	74	66
Full heater rod length (m)	3.96	
Partial heater rod length (m)	2.61	
Heater OD (mm)	10.9	
Rod pitch (mm)*	14.4	
Rod separation (mm)	3.5	
Water rod OD (main section) (mm)*	24.9	
Water rod ID (mm)*	23.4	
Channel box length (m)	4.13	
Channel box ID (mm)*	134	
Channel box OD (mm)*	139	
Corner channel box wall (mm)*	2.5	

*[Yamamoto *et al.,* 2002]

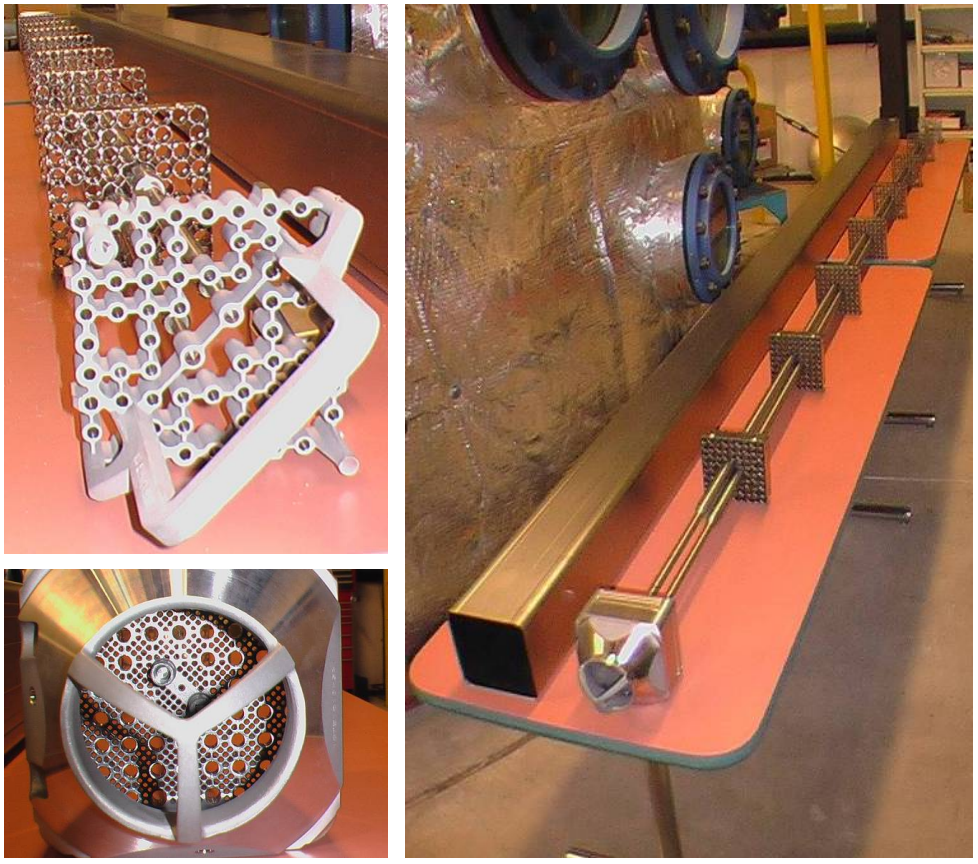

Figure 2.7 Typical 9×9 BWR components used to construct the test assembly including top tie plate (upper left), bottom tie plate (bottom left) and channel box and spacers assembled onto the water rods (right).

2.4 Instrumentation

The test apparatus was instrumented with thermocouples for temperature measurements, pressure transducers for internal gas pressure monitoring, and hot wire anemometers for flow velocity measurements in the exterior ducting. Voltage, amperage, and electrical power transducers were used to monitor electrical energy input to the test assembly.

Ninety-two TCs were previously installed on the BWR test assembly. The TCs used are ungrounded junction type-K with an Incoloy sheath diameter of 0.762 mm (0.030 in.) held in intimate contact with the cladding by thin Nichrome shims. These shims are spot welded to the cladding as shown in Figure 2.8. The TC attachment method allows the direct measurement of the cladding temperature. Details of the BWR test assembly and TC locations are described below and elsewhere [Lindgren *et al*., 2019, Lindgren and Durbin, 2013]. Additional TCs were installed on the other major components of the test apparatus such as the channel box, storage basket, canister wall, and exterior air ducting. TC placement on these components was designed to correspond with the existing TC placement in the BWR assembly.

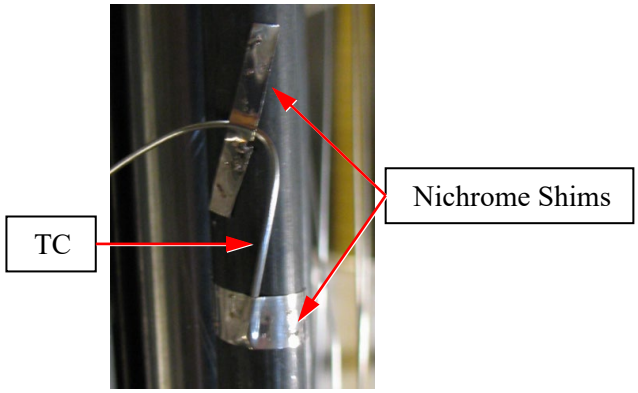

Figure 2.8 Typical TC attachment to heater rod.

Hot wire anemometers were chosen to measure the inlet flow rate because this type of instrument is sensitive and robust while introducing almost no unrecoverable flow losses. Due to the nature of the hot wire measurements, best results are achieved when the probe is placed in an isothermal, unheated gas flow. Hot wires were used to map the two-dimensional flow field across the inlet ducts. As implemented in the previous study [Durbin and Lindgren, 2018], these hot wires were traversed with computer-controlled stages.

2.4.1 Thermocouples

2.4.1.1 BWR Assembly TC Locations

The existing electrically heated and Incoloy-clad but otherwise prototypic BWR test assembly was previously instrumented with thermocouples in a layout shown in Figure 2.9. The TC naming convention is based on the alpha-alpha grid shown along the top and right-hand sides of the plan views shown in Figure 2.9b. As examples, the locations are shown for the TC on heater rod CS and the TC on the water rod at EU (WEU). Also shown with the plan views are the relative location of the four quadrants and the elevations applicable for each of the three plan views.

The assembly TCs are arranged in axial and transverse arrays. The axial cross-section is depicted in Figure 2.9a and transverse cross-sections are shown in Figure 2.9b.

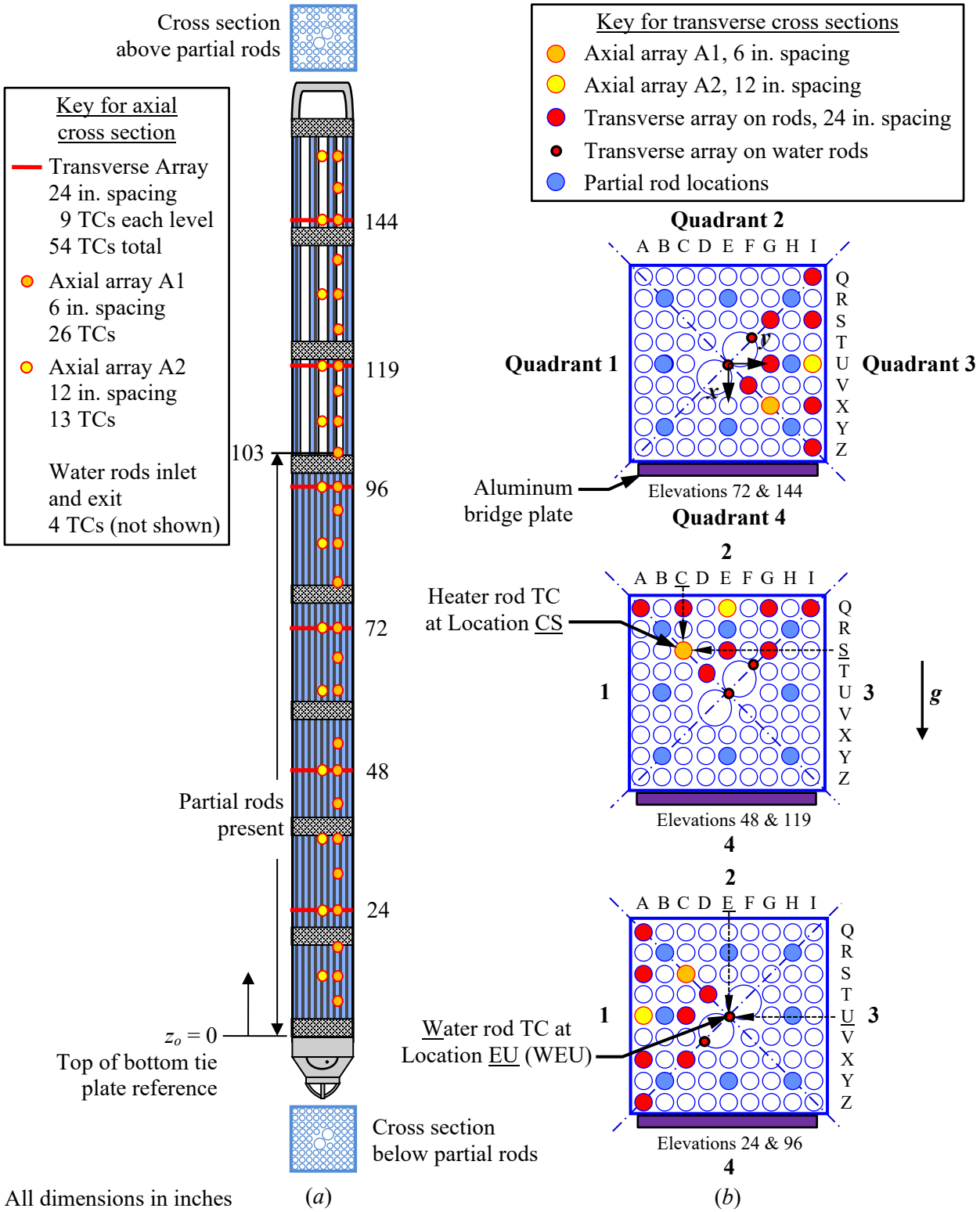

Figure 2.9 Experimental BWR assembly showing as-built *a*) axial and *b*) transverse thermocouple locations.

The axial array A1 has TCs nominally spaced every 0.152 m (6 in.) starting from the top of the bottom tie plate ($z_o = 0$ reference plane). Axial array A2 has TCs nominally spaced every 0.305 m (12 in.) and the transverse arrays are nominally spaced every 0.610 m (24 in.). The spacings are referred to as nominal due to a deviation at the 3.023 m (119 in.) elevation because of interference by a spacer. Note that the TCs in the axial array intersect with the transverse arrays.

Based on the need to optimally balance the TC routing through the assembly, the axial and transverse arrays of TCs were distributed among three separate quadrants relying on the assumption of axial symmetry that was valid for the initial, vertical orientation studied previously. However, the assumption of axial symmetry is not valid in the horizontal orientation. Based on the previous vertical orientation of the test apparatus inside of the CYBL vessel, the assembly was laid on the aluminum bridge plate on Quadrant 4, which lacks any TCs in the tube bundle. In the horizontal orientation, there is symmetry between Quadrants 1 and 3, and the peak cladding temperature was expected to be in Quadrant 2.

Figure 2.10 shows the definition of the reference coordinate system. The reference origin is defined as the center of the top surface of the bottom tie plate. The *x*-axis is positive in the direction of Quadrant 4, which points in the same direction as gravity, and negative in the direction of Quadrant 2. The *y*-axis is positive in the direction of Quadrant 3 and negative in the direction of Quadrant 1. The *z*-axis is along the axial direction.

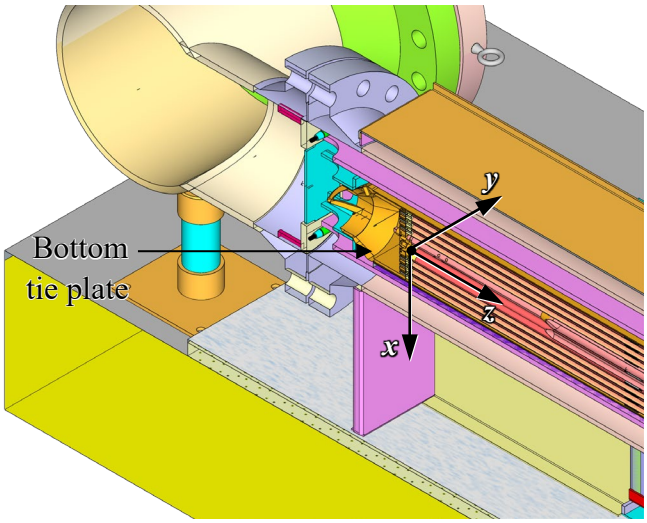

Figure 2.10 Definition of coordinate references in test apparatus.

2.4.1.2 BWR Channel Box TC Locations

The BWR channel box was instrumented with 25 TCs as depicted in Figure 2.11. Twenty-one of the TCs are on the channel faces, three are on the corners and one is on the pedestal. The TCs on the faces of the channel box are nominally located at $|x|, |y| = 0.069, 0$ m (2.704, 0 in.) or $|x|, |y| = 0, 0.069$ m (0, 2.704 in.) depending on the quadrant in which they are placed. TCs on the corners are nominally located at $|x|, |y| =$ 0.065, 0.065 m (2.564, 2.564 in.). The reference plane, z_o, is measured from the top of the bottom tie plate, the same as the BWR assembly. In the horizontal orientation, Quadrant 4 is down.

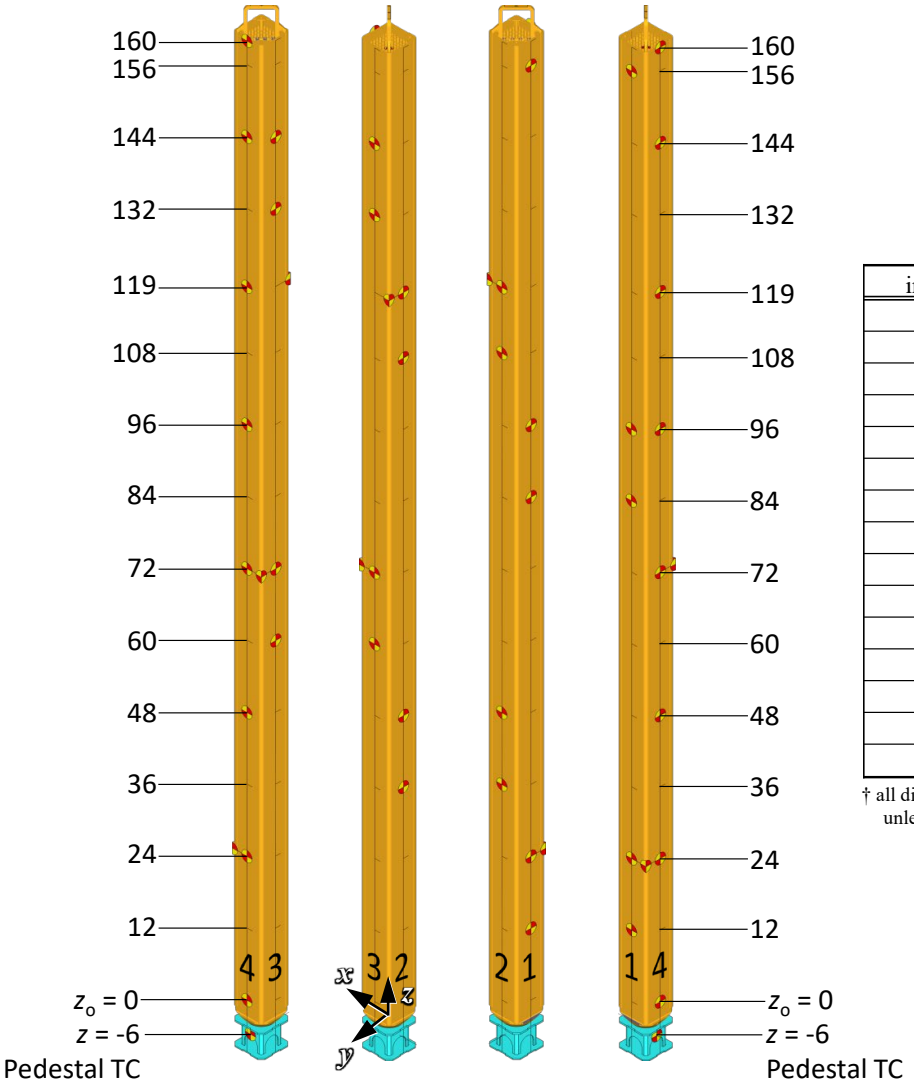

in.†	m
160	4.064
156	3.962
144	3.658
132	3.353
119	3.023
108	2.743
96	2.438
84	2.134
72	1.829
60	1.524
48	1.219
36	0.914
24	0.610
12	0.305
-6	-0.152

† all dimensions are in inches unless otherwise noted

Figure 2.11 BWR channel box showing thermocouple locations.

2.4.1.3 Storage Basket TC Locations

The storage basket is instrumented with 26 TCs as depicted in Figure 2.12. Twenty-one of the TCs are on the basket faces at the same positions as on the channel box, four are on the corners (the corner TC at the 4.191 m (165 in.) level does not correspond to a channel box TC) and one is on the basket face at the elevation of the pedestal. TCs located on the basket faces are nominally located at $|x|$, $|y|$ = 0, 0.089 m (0, 3.5 in.) and $|x|$, $|y|$ = 0.089, 0 m (3.5, 0 in.). TCs on the corners are nominally located at $|x|$, $|y|$ = 0.083, 0.083 m (3.281, 3.281 in.) The reference plane, z_o, is measured from the top of the bottom tie plate. The coordinates given are with respect to the test apparatus reference origin, as shown in Figure 2.10.

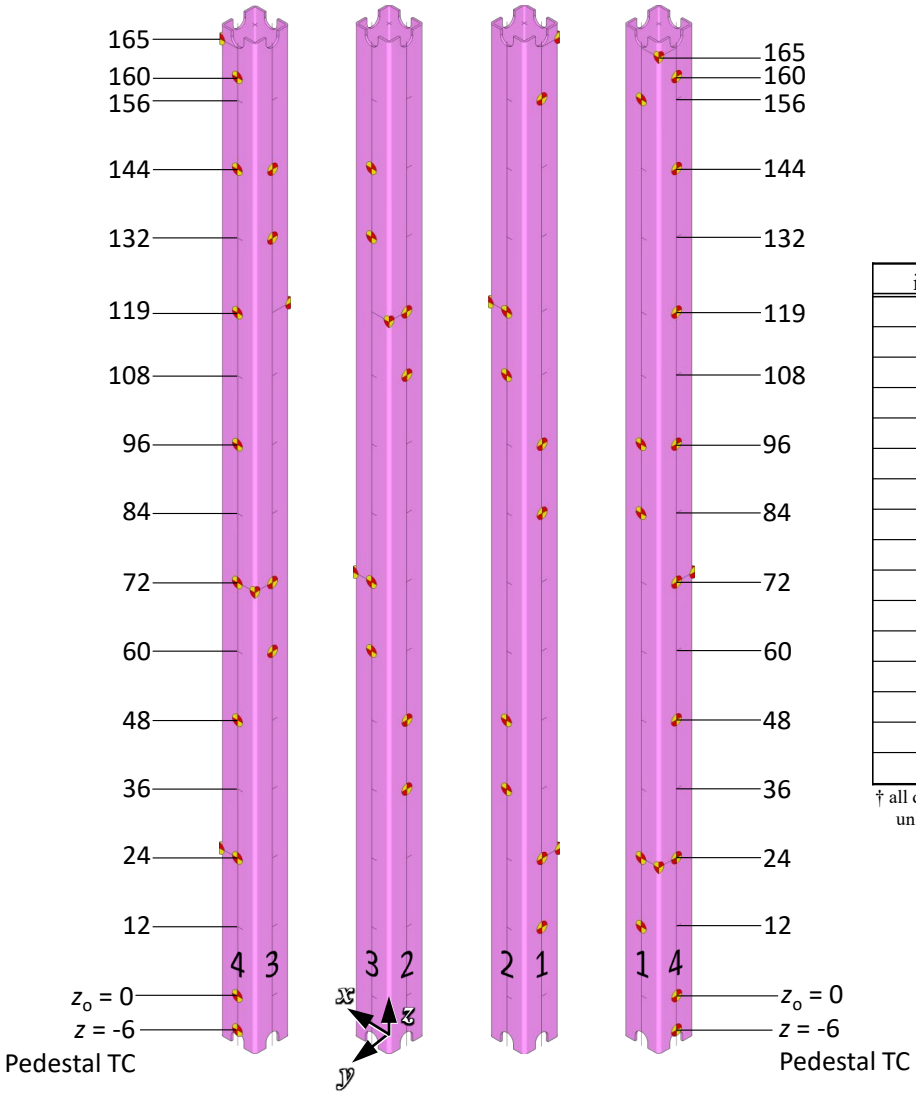

in.†	m
165	4.191
160	4.064
156	3.962
144	3.658
132	3.353
119	3.023
108	2.743
96	2.438
84	2.134
72	1.829
60	1.524
48	1.219
36	0.914
24	0.610
12	0.305
-6	-0.152

† all dimensions are in inches unless otherwise noted

Figure 2.12 Storage basket showing thermocouple locations.

2.4.1.4 Pressure Vessel TC Locations

The pressure vessel was instrumented with 27 TCs as depicted in Figure 2.13. Twenty-four of the TCs are aligned with the TCs on the storage basket faces and three are aligned with the TCs on the storage basket corners. TCs aligned with the storage basket faces are nominally located at $|x|$, $|y|$ = 0, 0.137 m (0, 5.375 in.) and $|x|$, $|y|$ = 0.137, 0 m (5.375, 0 in.). TCs aligned with the storage basket corners are nominally located at $|x|$, $|y|$ = 0.097, 0.097 m (3.801, 3.801 in.). The reference plane, z_o, is measured from the top of the bottom tie plate. The coordinates given are with respect to the test apparatus reference origin, as shown in Figure 2.10.

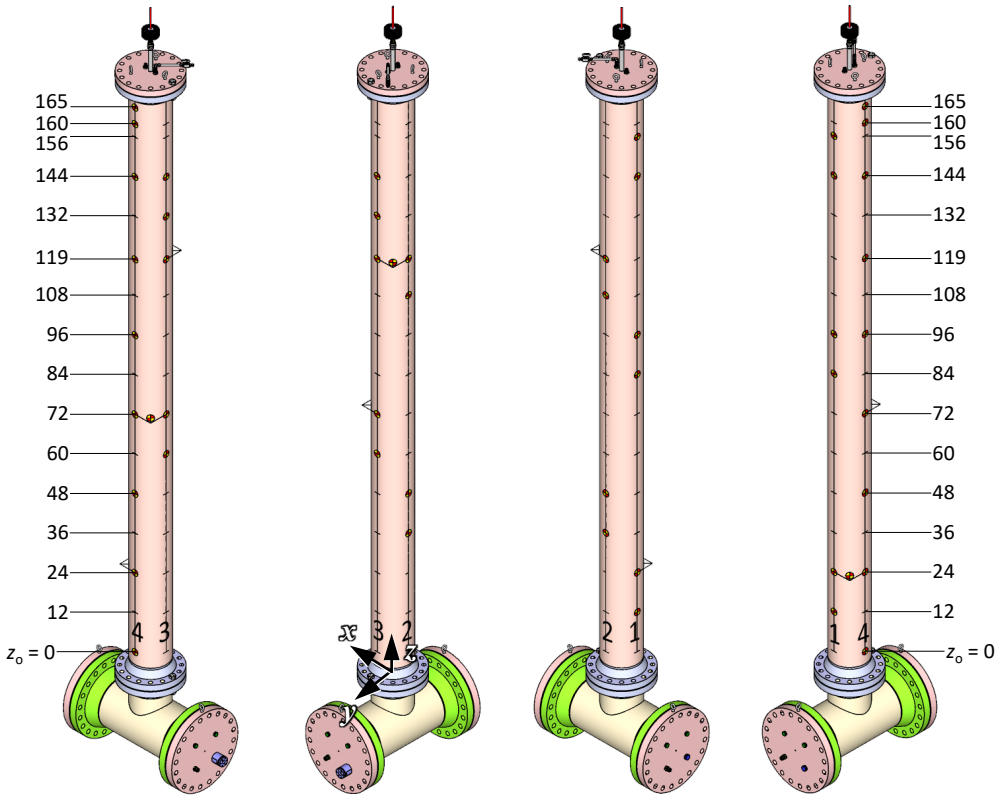

in.†	m
165	4.191
160	4.064
156	3.962
144	3.658
132	3.353
119	3.023
108	2.743
96	2.438
84	2.134
72	1.829
60	1.524
48	1.219
36	0.914
24	0.610
12	0.305

† all dimensions are in inches unless otherwise noted

Figure 2.13 Pressure vessel showing thermocouple locations.

2.4.1.5 Vault Enclosure and External TC Locations

The vault enclosure and the external ambient temperature regions are instrumented with 106 TCs, with some TCs shown in Figure 2.14 and Figure 2.15 and a comprehensive list included in Appendix B. Fourteen of the TCs are aligned along the centerline of the top lid at 0.305 m (12.0 in.) spacing. Twelve TCs are arranged in eight vertical arrays on the external side of the vault at nominally 0.610 m (24.0 in.) spacing. Twelve more TCs are placed on the opposite external side at nominally 0.610 m (24.0 in.) as well. The alternating, one-two TC layout pattern on the vertical side in Figure 2.14 is reversed (two-one) on the vertical side not shown. The TC locations for both sides of the vault are shown in Appendix B. Three TCs are placed internal to the vault at z = 2.13 m (84.0 in.) – two of these TCs are placed on the internal side of the side ribs at this axial location, and the remaining TC is placed on the internal side of the top lid. Nine TCs are placed along the baseplate that forms the bottom of the vault, as observed in Figure 2.15. One TC is placed on each of the four endplates of the vault (which adds up to 4 TCs total on all endplates). Ten gas TCs are placed around the pressure vessel, baseplate, and vault. Twenty gas TCs are placed internally within the vault inlets and outlets. Four TCs are placed around the HDCS instrumentation, and eighteen TCs are placed external to the vault to measure ambient temperatures. The reference plane, z_o, is measured from the top of the bottom tie plate.

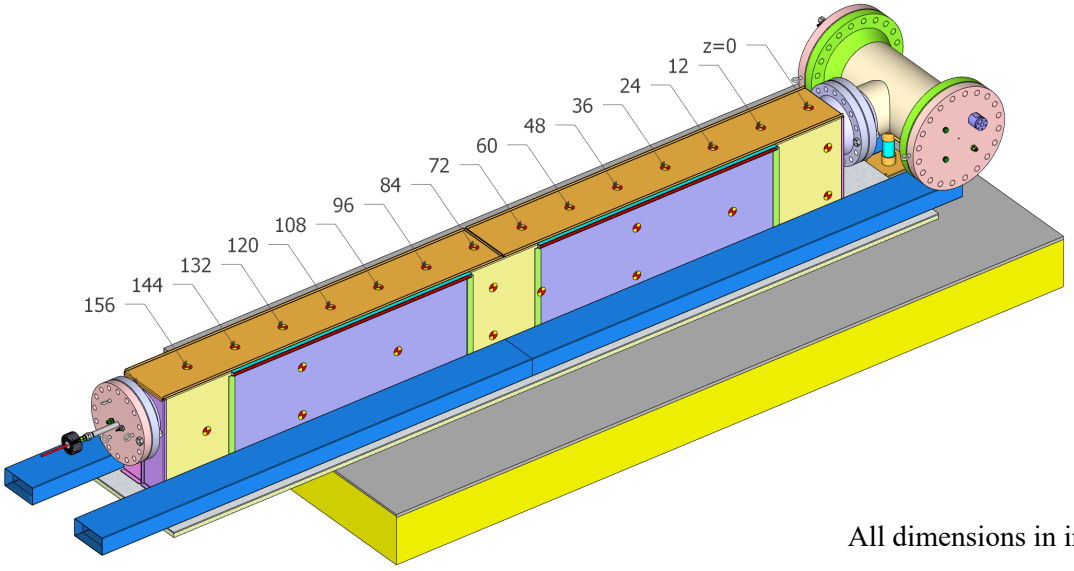

Figure 2.14 Vault without insulation showing thermocouple locations on the top and north sides.

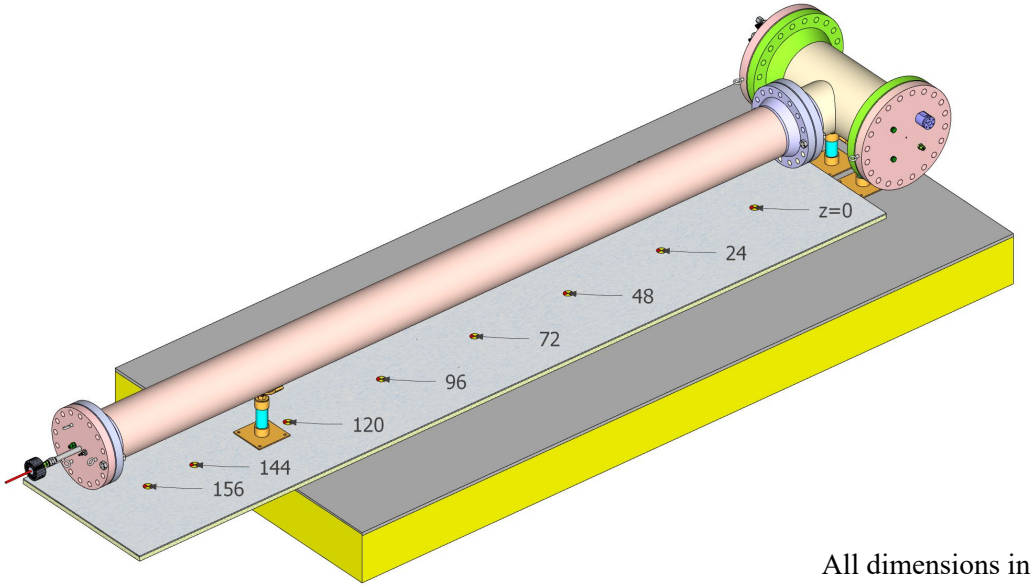

Figure 2.15 Base plate thermocouple locations.

2.4.2 Pressure and Pressure Vessel Leak Rates

Two high-accuracy 0 to 1,034 kPa (0 to 150 psia) absolute pressure transducers (Setra Systems ASM1-150P-A-1M-2C-03-A-01) are installed in the instrument well. The pressure measurements are made in duplicate due of the importance of the measurement. The experimental uncertainty associated with these gauges is ±0.05% of full scale, or ±0.52 kPa (±0.075 psi).

All penetrations and fittings were selected for the apparatus to have helium leak rates of 1×10^{-6} std. cm^3/s or better at 100 kPa. In addition, spiral-wound gaskets capable of leak rates of better than 1×10^{-7} std. cm^3/s were used to form the seals at each flange. The ANSI N14.5 leak rate of 1×10^{-4} std. cm^3/s [ANSI, 2014] would result in an observable pressure drop of 0.03 kPa (4×10^{-3} psi) after a one-week period, which is far below the experimental uncertainty of 0.52 kPa (0.075 psi). During previous testing, leaks in the as-

built apparatus were identified and repaired as best as possible [Durbin and Lindgren, 2018]. Ultimately, a small leak path of undetermined origin remains, and a positive pressure control system was implemented to maintain pressure as described next.

2.4.2.1 Pressure Control

A pressure control system has been implemented using the high-accuracy, absolute-pressure transducers, three low-flow needle valves, and three positive-shutoff actuator valves under control of the LabView data acquisition (DAQ) system (Figure 2.16). Two actuator valves (vent) control flow out of the vessel, and the third valve (fill) controls the fill gas flow into the vessel. As the vessel heats up, the expanding backfill gas vents out of the first actuator and needle valve to maintain a constant pressure. A second vent valve (overflow) activates if the vessel continues to pressurize. As steady state is reached, the small leak will slowly reduce the backfill pressure, at which point the control system opens the third actuator valve (fill) to allow a small flow through the third needle valve. Overall, a similar pressure control system used in past testing was able to maintain the vessel pressure constant to within ±0.3 kPa (0.044 psi).

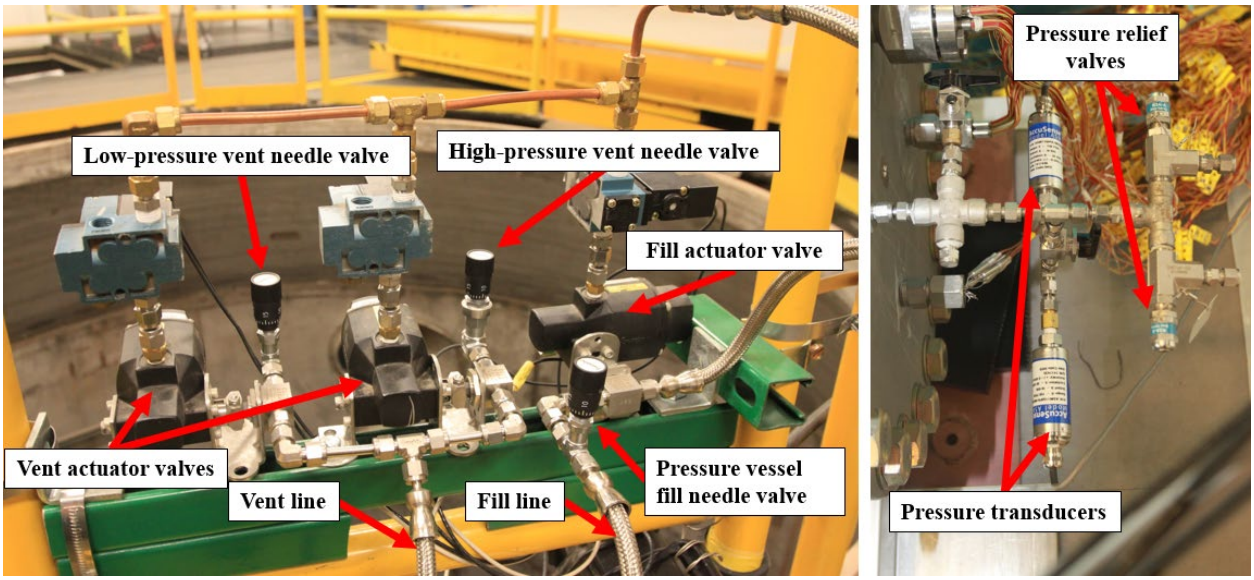

Figure 2.16 HDCS pressure control system.

2.4.2.2 Pressure Vessel Internal Volume Measurement

The pressure vessel internal volume was measured during previous testing [Durbin and Lindgren, 2018]. The total internal volume was determined to be 252.0 liters, with an uncertainty of ±2.6 liters. This measurement includes the volume of the instrument well that is insulated from the heated test section.

2.4.3 Power Control

A diagram of the test assembly power control system is shown in Figure 2.17 and the details inside the instrument panel are shown in Figure 2.18. The electrical voltage and current delivered to the test assembly heaters is controlled to maintain a constant power by a digital silicon-controlled rectifier (SCR). The DAQ system provides a power setpoint to the SCR that is constantly compared to the measured output power. The power, voltage, and current measurements are collected by the DAQ. The details of the instrumentation used to control and measure the electrical power are provided in Table 2.4. A special calibration schedule of thirty-two points was ordered for the power diagnostic (Ohio Semitronics PTB-112D1PCY48). The observed 95% uncertainty bounds based off the Student's t-value and the standard error of the regression for this instrument give an uncertainty of $U_{Watt} = \pm 13$ W. Additional details may be found in Appendix A.

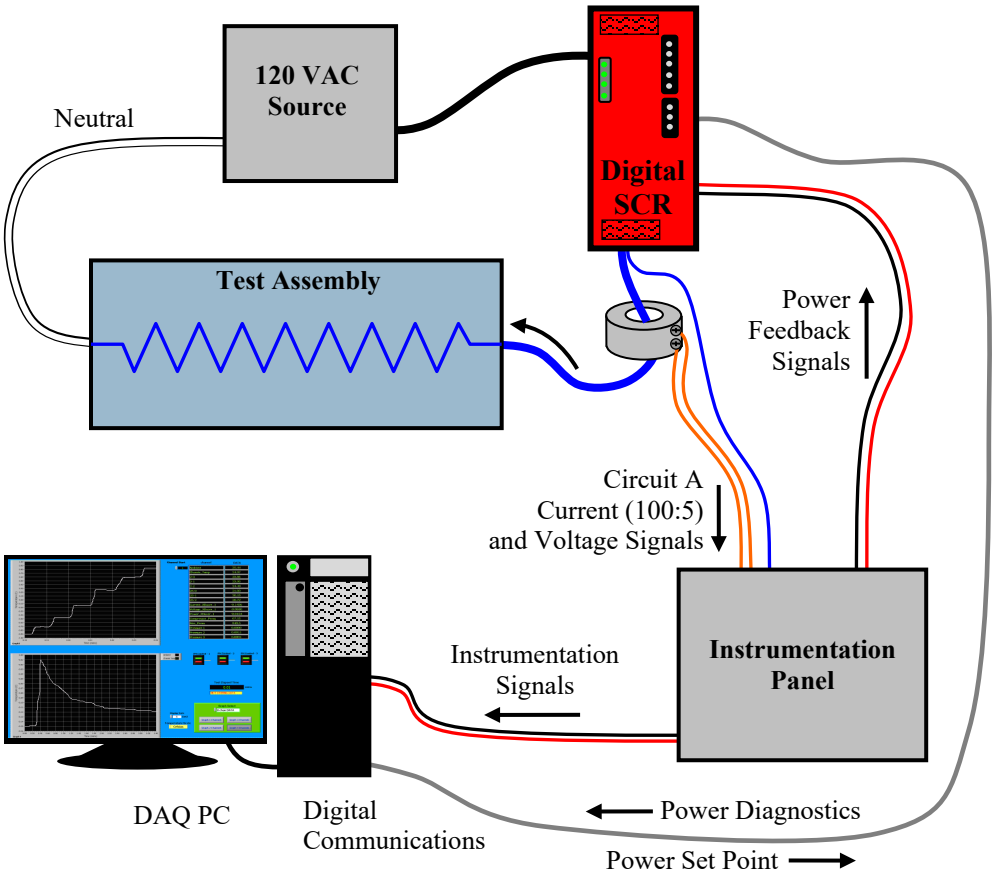

Figure 2.17 Power control system and test circuits.

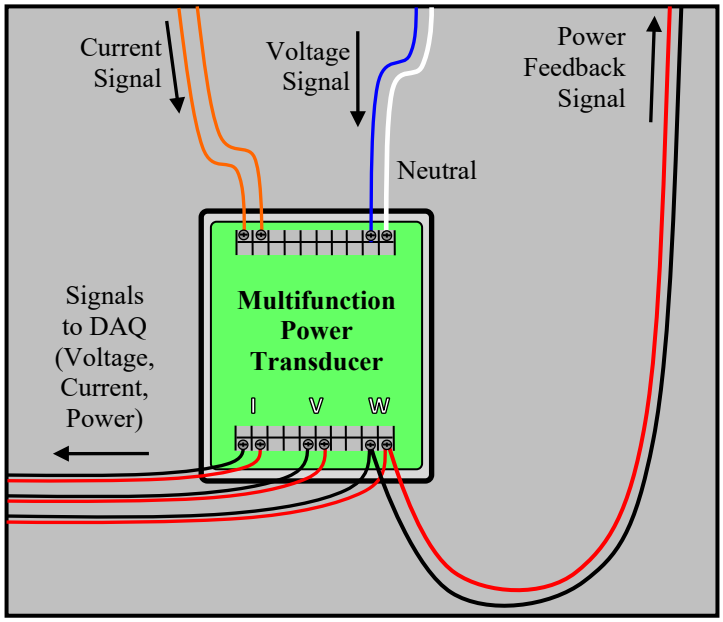

Figure 2.18 Schematic of the instrumentation panel for voltage, current, and power measurements.

Table 2.4 List of power control equipment.

Description	Manufacturer	Model
Power Test Board (PTB) – Measures Volts, Amps, Watts	Ohio Semitronics	PTB-112D1PCY48
Digital SCR Power Controller	Control Concepts	uF1HXLGI-130-P1RSZ

2.4.4 Hotwires

The hotwire anemometers used are TSI model 8455 where the tip detail is shown in Figure 2.19. For scale, the largest shaft diameter shown is 6 mm (0.25 in.). The sensing element of the model 8455 is protected inside of an open cage and is sensitive to flows down to 0.13 m/s (25 ft/min) with a response time of 0.2 seconds. The instrument uncertainty in the air mass flow rate per duct was calculated to be $U_{\dot{m},\,\text{per duct}} = \pm 1.5 \times 10^{-4}$ kg/s. The combined error in the total air mass flow rate across all four ducts is $U_{\dot{m},\,\text{Total}} = \pm 3.0 \times 10^{-4}$ kg/s. Additional details may be found in Appendix A.

Figure 2.19 Photograph of the hot wire anemometer tip.

2.5 Air Mass Flow Rate

Figure 2.20 shows the air flow pattern through the HDCS vault. Cold air is drawn into the air inlet ducts and flows into the vault inlets on the sides of the enclosure. The air heats as it passes between the vault and the simulated canister. The hot air exhausts at the top of the enclosure sides via the vault outlets. The hotwires are mounted on motorized stages (Velmex Stage XN10-0040-M02-71, Motor PK245-01AA). The data acquisition computer communicates with the stage controller (Velmex Controller VXM-4) to identify and verify hot wire positioning.

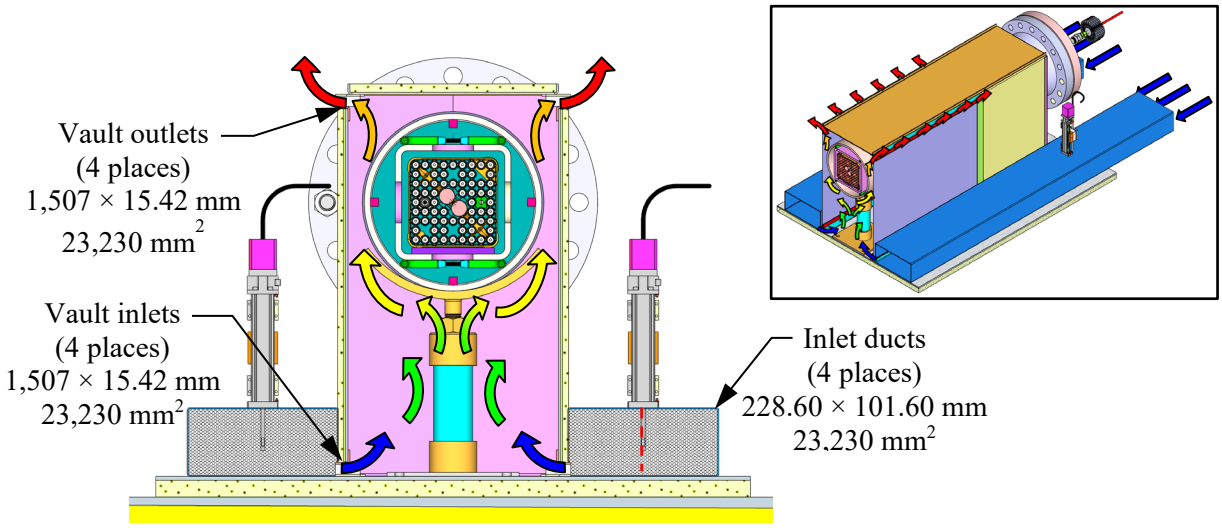

Figure 2.20 Air flow pattern in the HDCS from natural convection.

The methods for determining the induced air flow in the HDCS are based on the successful methods developed in the previous aboveground and belowground, vertical DCS studies [Durbin and Lindgren, 2018]. The methods used hot wire anemometers to measure inlet air velocity and subsequently calculate an overall air mass flow rate.

2.5.1 Flow Straightening

To obtain the most stable and repeatable measurements possible, a honeycomb element is inserted into all four assembly inlets to align the flow in the desired direction and reduce any flow disturbances on the hot wire anemometers. As shown in Figure 2.21, a plastic honeycomb element was chosen with a cell diameter, wall thickness, and flow length of 3.8, 0.1, and 25.8 mm (0.150, 0.004, and 1.015 in.), respectively. This type of flow straightening element has been found to provide the greatest reduction in hot wire fluctuations while introducing the smallest pressure drop to the system. The effective frictional coefficient for this honeycomb material was found to be $D = 2.7 \times 10^6$ m^{-2} for porous media in CFD simulations.

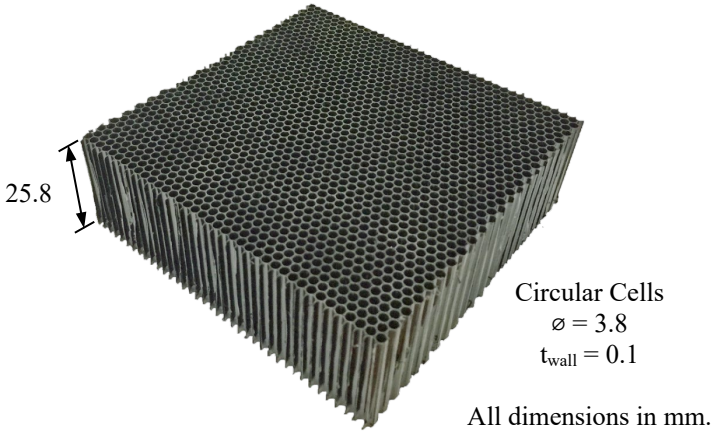

Figure 2.21 Photograph of the honeycomb element used for flow straightening.

As depicted in Figure 2.22, the flow straightener section featured a convergent nozzle made of corrugated fiberboard and scrim-backed, pressure-sensitive tape. This nozzle minimized the flow losses associated with the honeycomb element by increasing the flow area by a factor of four. The honeycomb dimensions used in each of the four inlets was 0.425 m (16.7 in.) tall by 0.233 m (9.2 in.) wide and 0.0258 m (1.02 in.) thick for a flow area of 0.099 m^2. The nozzle design included two straight sections to accommodate the honeycomb and the assembly inlet. Long-sweep arcs with matching tangents at the inflection point were chosen to provide a smooth transition from the honeycomb section to the assembly inlet.

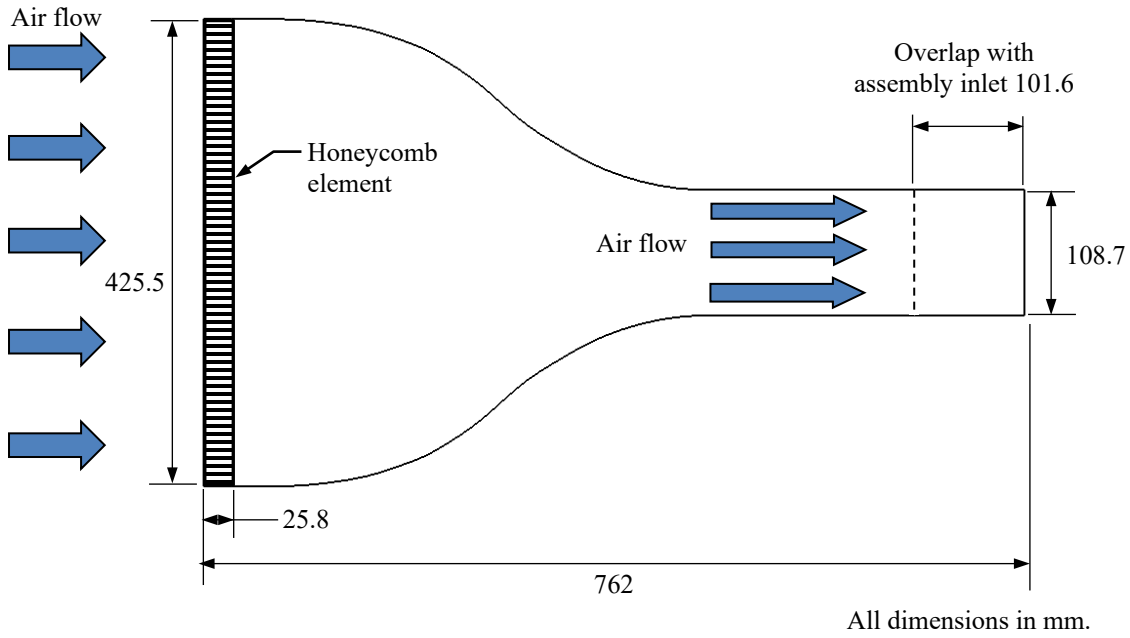

Figure 2.22 Cutaway schematic of the flow straightener.

2.5.2 Air Flow Measurement

The inlet flow straightening nozzles and hot wire anemometer locations for the HDCS are depicted in Figure 2.23. After the four convergent nozzles, rectangular ducts with nominal cross-sectional dimensions of 0.229 m (9.00 in.) by 0.102 m (4.00 in.) convey the inlet flow into the simulated vault. Multiple hot wire anemometers are located nominally 0.5400 m (21.25 in.) downstream from the inlet of each duct to map the inlet air flow. Shown in Figure 2.23 are representative motorized stages and hot wire anemometers on two ducts.

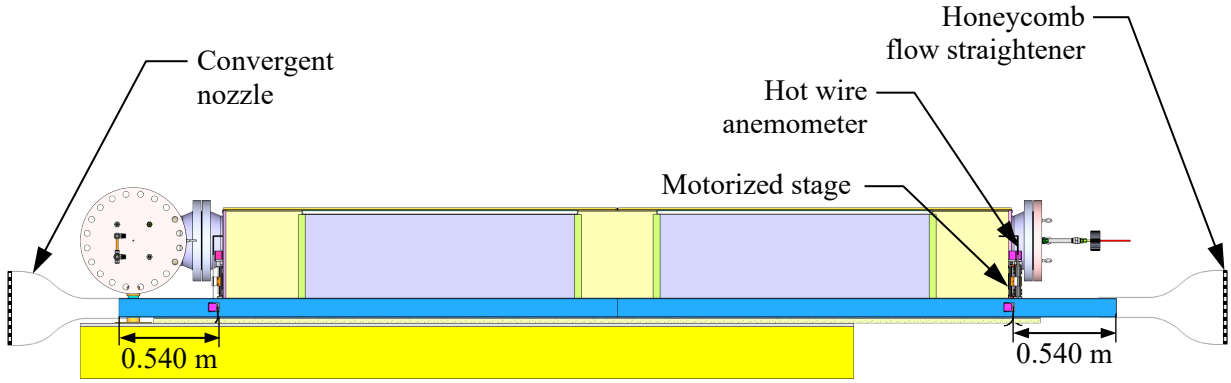

Figure 2.23 Flow straightening nozzles and hot wire anemometer locations in the inlet ducts.

As illustrated in Figure 2.24, in each duct there are at least three (and in one duct four) hot wire anemometers on motorized stages. Each duct has a vertical hot wire anemometer that traverses across the center of the duct in the *x*-direction and a horizontal hot wire anemometer that traverses across the center of the duct in the *y*-direction 25.4 mm (1.00 in.) farther downstream. Additionally, the NE duct and the

SW duct have a vertical hot wire anemometer that traverses in the *x*-direction 9.5 mm (0.38 in.) from the outer duct wall, the NW duct has a vertical hot wire anemometer that traverses in the *x*-direction 9.5 mm (0.38 in.) from the inner duct wall, and the SE duct has two additional vertical hot wire anemometers that traverses in the *x*-direction 9.5 mm (0.38 in.) from both the inner and outer duct walls.

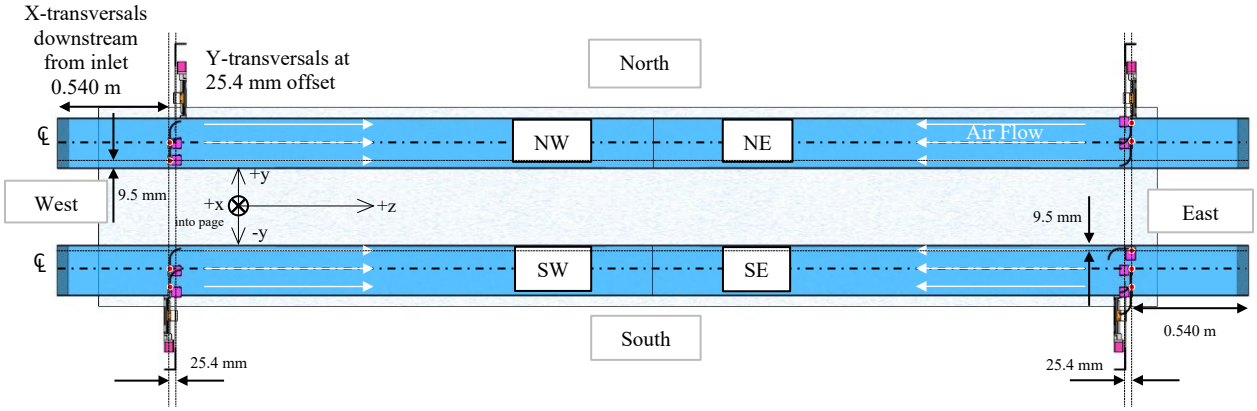

Figure 2.24 Plan view location details of hotwire anemometers in the inlet ducts.

The measured steady-state velocities in all four ducts were averaged and used to determine a 2-dimensional distribution of average duct velocity across the duct flow area. The duct flow area is discretized into rectangular elements with a flow velocity determination associated with the center of each element as illustrated in Figure 2.25. The values shown in green are derived from the vertical traverses. The values shown in blue are derived from the horizontal traverse. The values shown in yellow are derived by similarity with the horizontal and vertical velocity profile measurements. The region shown in red on the periphery is the no-slip region with no flow along the outer walls.

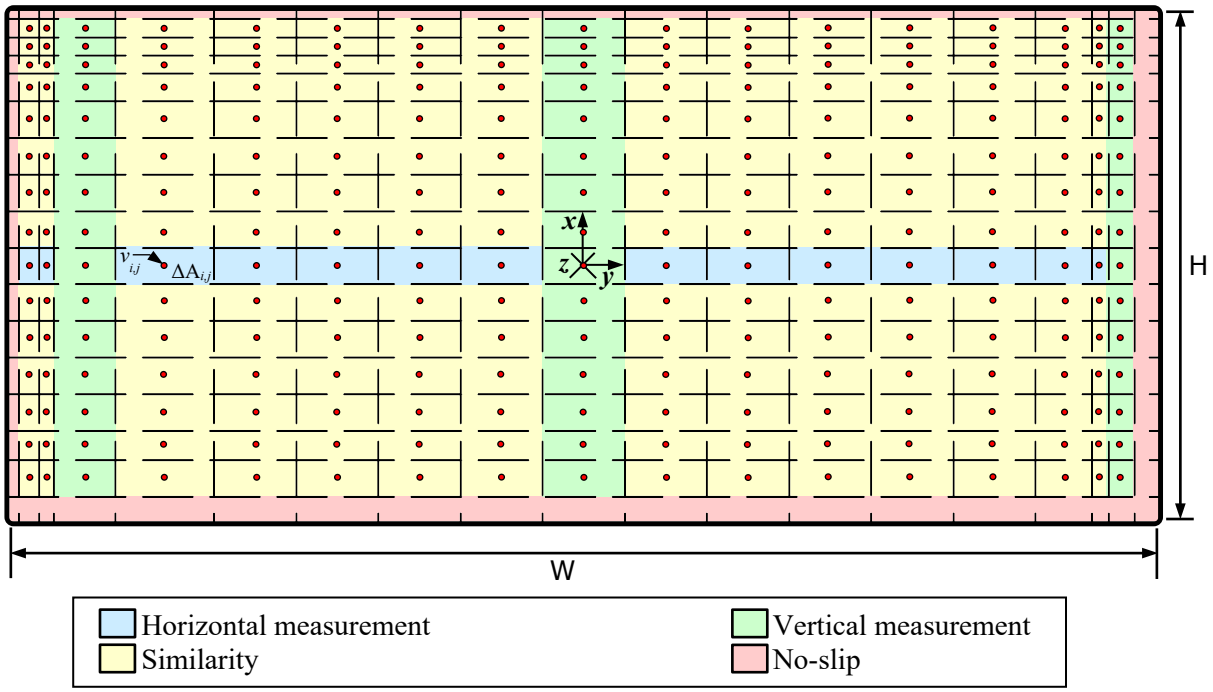

Figure 2.25 Diagram showing the integration scheme for the calculation of air mass flow rate at the inlet.

Each velocity was assumed to be constant across the differential area, $\Delta A_{i,j}$, defined by the coordinates of $\left(\frac{x_i+x_{i-1}}{2}, \frac{y_j+y_{j-1}}{2}\right)$ and $\left(\frac{x_i+x_{i+1}}{2}, \frac{y_j+y_{j+1}}{2}\right)$ where i is the x-coordinate index and j is the y-coordinate index. The integrated, natural air mass flow rate is given in Equation 2-1.

$$\dot{m}_{\text{Tot}} = \sum_{j=1}^{17} \sum_{i=1}^{19} \rho_{\text{ref}} \cdot \Delta A_{i,j} \cdot v_{i,j} \qquad 2\text{-}1$$

The reference density is defined by the standard conditions for the TSI hot wires, or ρ_{ref} = 1.2 kg/m^3 at 21.1 °C and 101.4 kPa. Using this midpoint approximation scheme, the no-slip condition is assumed to apply to the area half-way between the wall and the nearest available velocity values. Applying the no-slip condition in this manner equates to assuming the velocity varies linearly between zero at the wall to the nearest measured value, which is expected to underestimate the flow rate based on comparisons with boundary layer theory.

Table 2.5 gives differential area, $\Delta A_{i,j}$, by location in the inlet. These differential areas are used for all calculations of air mass flow rate as defined in Equation 2-1. The measured locations of the hot wire anemometers were used to determine each differential area.

Table 2.5 Differential areas for the calculation of air mass flow rate.

All values in mm^2.

y (mm) / *x* (mm)	-113.2	-110.2	-106.1	-104.6	-81.6	-65.3	-49.0	-32.6	-16.3	0.0	16.3	32.6	49.0	65.3	81.6	97.9	104.1	104.6	111.8
50.4	4	7	5	22	36	30	30	30	30	30	30	30	30	30	30	21	6	9	9
47.7	7	15	10	45	72	60	60	60	60	60	60	60	60	60	60	41	12	19	18
44.0	7	15	10	45	72	60	60	60	60	60	60	60	60	60	60	41	12	19	18
40.3	7	15	10	45	72	60	60	60	60	60	60	60	60	60	60	41	12	19	18
36.7	11	22	15	67	108	90	90	90	90	90	90	90	90	90	90	62	18	28	27
29.3	15	30	21	90	144	120	120	120	120	120	120	120	120	120	120	82	24	37	35
22.0	15	30	21	90	144	120	120	120	120	120	120	120	120	120	120	82	24	37	35
14.7	15	30	21	90	144	120	120	120	120	120	120	120	120	120	120	82	24	37	35
7.3	15	30	21	90	144	120	120	120	120	120	120	120	120	120	120	82	24	37	35
0.0	15	30	21	90	144	120	120	120	120	120	120	120	120	120	120	82	24	37	36
-7.3	15	30	21	90	144	120	120	120	120	120	120	120	120	120	120	82	24	37	36
-14.7	15	30	21	90	144	120	120	120	120	120	120	120	120	120	120	82	24	37	35
-22.0	15	30	21	90	144	120	120	120	120	120	120	120	120	120	120	82	24	37	35
-29.3	15	30	21	90	144	120	120	120	120	120	120	120	120	120	120	82	24	37	35
-36.7	12	24	17	72	116	96	96	96	96	96	96	96	96	96	96	66	20	30	29
-41.1	15	30	21	90	144	120	120	120	120	120	120	120	120	120	120	82	24	37	35
-48.8	10	21	14	62	100	83	83	83	83	83	83	83	83	83	83	57	17	26	25

2.6 Test Matrix

The HDCS test series presented in this report expands upon the series shown in the HDCS update report [Lindgren *et al*., 2019] with the inclusion of tests using helium/air blends as backfill gases. The test series in this report is comprised of twenty tests as summarized in Table 2.6. Of these twenty, eight are from the HDCS update report – namely, the helium and air tests at 100 kPa fill pressure. In this report, the backfill gases are reported as a function of mole concentration of helium (He), balanced by air, so the helium and air backfill tests are denoted as 1.0 and 0.0 He, respectively. The other twelve tests are the new tests with helium/air blends, using the following mole fractions of helium, balanced by air: 0.9, 0.5, and 0.1 He. For each of the backfill gases, the assembly was powered at four power levels: 0.50, 1.00, 2.50, and 5.00 kW. The steady-state comparison metrics used to quantify the thermal-hydraulic effects of the loss of helium backfill in a horizontal dry storage system are shown in Table 2.7.

Table 2.6 HDCS loss of helium backfill test matrix.

Power (kW)	Mole Fraction He, Balance Air
0.50	1.0
1.00	1.0
2.50	1.0
5.00	1.0
0.50	0.9
1.00	0.9
2.50	0.9
5.00	0.9
0.50	0.5
1.00	0.5
2.50	0.5
5.00	0.5
0.50	0.1
1.00	0.1
2.50	0.1
5.00	0.1
0.50	0.0
1.00	0.0
2.50	0.0
5.00	0.0

Table 2.7 Steady-state comparison metrics used for examination of the effects of loss of helium backfill in the HDCS.

Metric	Notes
Peak Cladding Temperature	PCT
Air mass flow rate	$\dot{m}_{Air}$
Centerline fuel axial temperature profile	T(z) at WEU (5 locations)
Canister axial temperature profile	T(z) along Quadrant 4 of canister surface (9 locations)
Transverse x-axis temp. profile	T(x) at z = 48 in. (11 locations)
Transverse y-axis temp. profile	T(y) at z = 72 in. (7 locations)
Canister/Ambient Temperature Difference	T_{can} - T_{amb} vs. mole fraction helium
Inlet/Outlet Duct Temperature Difference	T_{out} - T_{in} vs. mole fraction helium

3 STEADY-STATE RESULTS

A total of twenty tests were conducted where the HDCS achieved steady state for various assembly powers. The power levels tested were 0.50, 1.00, 2.50, and 5.00 kW. All tests were run at 100 kPa vessel pressure. The backfill gases used in these tests consisted of the following mole fractions of helium, balanced by air: 1.0, 0.9, 0.5, 0.1, and 0.0 He.

The criterion for steady state was considered met when the first derivative with respect to time of most TCs in the test apparatus was ≤ 0.3 K/h. The steady-state values reported here represent the average of data collected from the point this criterion was met in the majority of data channels to the end of the test.

3.1 Results Summary

Table 3.1 through Table 3.4 show the steady-state results for all tests considered in this report. The tables lists the average, maximum, and minimum values for the applied power, peak temperatures of the cladding, channel box, storage basket, pressure vessel, vault enclosure, and ambient, as well as the total induced cooling air flow rate. The average steady-state powers for all tests were all to within 3 W of the anticipated result. The induced flows across the tests for any given power were all similar and the differences were within experimental error, $U_{\dot{m},\,\mathrm{Total}} = \pm 3\times10^{-4}$ kg/s. The steady-state peak temperatures for the components inside the pressure vessel increased steadily as the helium concentration decreases. The greatest difference was in the fuel bundle, and the difference decreased for components moving outward. The steady-state peak temperatures for the vault enclosure were within the largest experimental uncertainty ($U_T = \pm 1\%$ of the maximum temperature in K) across the tests for any given power. The tables also list the axial location of the peak temperature and the rod or quadrant that the peak temperature occurred (see Figure 2.9 for rod and quadrant naming convention). For most cases, the PCT was located at z = 1.22 m, while for some of the higher power cases the PCT was located at z = 0.61 m. The PCT was either located on rod ES in Quadrant 2, which is located on the upward face, or on rod DT, which lies on the boundary between Quadrant 1 and Quadrant 2 according to Figure 2.10 and is close to rod ES. The peak temperatures for the channel box were located on either Quadrant 2 or Quadrant 3. For the basket, the peak temperature was located either in Quadrant 2 or on the bottom face (Quadrant 4). For the vault enclosure, the peak temperature was always located in Quadrant 2 (the top face).

Table 3.1 Steady-state results for various components for the 0.50 kW tests for all helium/air gas backfill compositions.

Mole Fraction He, Balance Air		Power (W)	Pressure (kPa)	PCT (K)	Channel (K)	Basket (K)	Vessel (K)	Vault (K)	Ambient (K)	Tot. Flow Rate (kg/s)
1.0	**Average**	**499**	**99.8**	**373.3**	**357.7**	**344.4**	**332.2**	**314.8**	**295.3**	**0.0165**
	Max	503	100.0	373.5	357.9	344.6	332.6	316.2	298.3	0.0166
	Min	493	99.6	372.8	357.4	344.1	331.8	314.4	294.1	0.0159
	Rod or Quadrant #			ES	2	4	2	2 (top)		
	z-Location (m)			1.22	1.22	1.22	1.22	1.52		
0.9	**Average**	**500**	**99.8**	**376.0**	**358.2**	**343.9**	**330.8**	**314.9**	**296.7**	**0.0149**
	Max	503	100.0	377.1	359.3	344.9	331.8	315.9	298.4	0.0157
	Min	492	99.6	374.5	356.9	342.5	329.5	313.2	294.7	0.0137
	Rod or Quadrant #			ES	2	4	2	2 (top)		
	z-Location (m)			1.22	1.22	1.22	1.22	1.52		
0.5	**Average**	**500**	**99.8**	**392.6**	**367.6**	**347.0**	**329.4**	**313.4**	**295.7**	**0.0146**
	Max	506	100.0	393.3	368.1	347.8	330.3	314.8	297.9	0.0157
	Min	483	99.6	390.9	365.9	345.4	328.1	312.3	294.4	0.0132
	Rod or Quadrant #			ES	3	4	2	2 (top)		
	z-Location (m)			1.22	1.52	1.83	1.22	1.52		
0.1	**Average**	**500**	**99.8**	**414.6**	**378.4**	**351.4**	**330.0**	**314.0**	**296.1**	**0.0142**
	Max	507	100.0	415.4	379.2	352.2	330.8	314.7	297.5	0.0156
	Min	487	99.6	413.0	376.7	349.9	329.0	312.8	294.0	0.0132
	Rod or Quadrant #			ES	3	4	2	2 (top)		
	z-Location (m)			1.22	1.52	1.83	1.22	1.52		
0.0	**Average**	**500**	**99.8**	**426.6**	**385.7**	**354.0**	**331.5**	**315.2**	**296.6**	**0.0141**
	Max	503	100.0	427.4	386.4	354.8	332.4	316.3	298.2	0.0149
	Min	495	99.6	426.4	385.4	353.9	331.0	314.3	295.0	0.0131
	Rod or Quadrant #			ES	2	4	2	2 (top)		
	z-Location (m)			1.22	1.22	1.83	1.22	1.52		

Table 3.2 Steady-state results for various components for the 1.00 kW tests for all helium/air gas backfill compositions.

Mole Fraction He, Balance Air		Power (W)	Pressure (kPa)	PCT (K)	Channel (K)	Basket (K)	Vessel (K)	Vault (K)	Ambient (K)	Tot. Flow Rate (kg/s)
1.0	**Average**	**1000**	**99.8**	**433.0**	**404.2**	**381.3**	**359.2**	**331.2**	**297.8**	**0.0195**
	Max	1011	100.0	433.1	404.5	381.5	359.5	332.0	300.8	0.0208
	Min	989	99.6	432.7	403.9	381.1	359.1	330.9	296.6	0.0185
	Rod or Quadrant #			ES	3	4	2	2 (top)		
	z-Location (m)			1.22	1.52	1.22	1.22	1.22		
0.9	**Average**	**1000**	**99.8**	**433.7**	**403.2**	**378.8**	**355.4**	**328.5**	**296.5**	**0.0199**
	Max	1020	100.0	434.6	404.1	379.7	356.5	329.8	298.4	0.0206
	Min	981	99.6	432.7	402.2	377.9	354.5	327.3	294.6	0.0189
	Rod or Quadrant #			ES	3	4	2	2 (top)		
	z-Location (m)			1.22	1.52	1.22	1.22	1.22		
0.5	**Average**	**1000**	**99.8**	**459.6**	**417.0**	**384.4**	**354.3**	**327.3**	**296.2**	**0.0196**
	Max	1018	100.1	460.3	417.4	384.9	354.8	328.1	298.2	0.0204
	Min	991	99.6	458.5	416.2	383.4	353.5	326.9	294.7	0.0188
	Rod or Quadrant #			ES	3	4	2	2 (top)		
	z-Location (m)			1.22	1.52	1.22	1.22	1.22		
0.1	**Average**	**1000**	**99.8**	**487.5**	**432.0**	**388.1**	**353.0**	**326.3**	**295.9**	**0.0194**
	Max	1016	100.0	488.1	432.5	388.5	353.5	327.0	298.4	0.0201
	Min	990	99.6	485.5	430.2	386.1	351.4	325.1	293.9	0.0181
	Rod or Quadrant #			ES	2	4	2	2 (top)		
	z-Location (m)			1.22	1.22	1.22	1.22	1.22		
0.0	**Average**	**1000**	**99.8**	**501.4**	**442.5**	**393.4**	**356.4**	**328.8**	**296.4**	**0.0194**
	Max	1013	100.0	502.4	443.0	393.8	356.8	329.4	298.7	0.0202
	Min	992	99.6	499.6	441.0	392.2	355.6	328.2	294.4	0.0188
	Rod or Quadrant #			ES	2	4	2	2 (top)		
	z-Location (m)			1.22	0.91	1.83	1.22	1.22		

Table 3.3 Steady-state results for various components for the 2.50 kW tests for all helium/air gas backfill compositions.

Mole Fraction He, Balance Air		Power (W)	Pressure (kPa)	PCT (K)	Channel (K)	Basket (K)	Vessel (K)	Vault (K)	Ambient (K)	Tot. Flow Rate (kg/s)
1.0	**Average**	**2503**	**99.8**	**558.6**	**505.8**	**463.5**	**420.6**	**367.7**	**296.7**	**0.0283**
	Max	2518	100.1	559.4	506.7	464.7	422.3	370.1	302.3	0.0286
	Min	2492	99.6	557.8	504.8	462.5	419.4	366.3	294.0	0.0273
	Rod or Quadrant #			DT	2	4	2	2 (top)		
	z-Location (m)			1.22	1.22	1.22	1.22	1.22		
0.9	**Average**	**2500**	**99.8**	**561.8**	**504.9**	**460.9**	**414.4**	**364.0**	**296.8**	**0.0280**
	Max	2521	100.1	562.2	505.7	461.5	415.2	364.8	298.9	0.0284
	Min	2487	99.6	560.8	504.1	459.9	413.4	362.9	294.7	0.0277
	Rod or Quadrant #			DT	2	4	2	2 (top)		
	z-Location (m)			1.22	1.22	1.22	1.22	1.22		
0.5	**Average**	**2500**	**99.8**	**595.1**	**525.7**	**469.1**	**413.6**	**363.5**	**296.8**	**0.0272**
	Max	2539	100.0	595.8	526.2	469.7	414.5	364.5	299.1	0.0277
	Min	2449	99.6	594.1	525.2	468.0	412.2	362.1	294.8	0.0268
	Rod or Quadrant #			ES	3	4	2	2 (top)		
	z-Location (m)			1.22	1.52	1.22	1.22	1.22		
0.1	**Average**	**2500**	**99.8**	**623.3**	**545.9**	**478.1**	**415.6**	**364.2**	**297.0**	**0.0273**
	Max	2527	100.0	625.8	546.2	478.7	416.3	365.0	299.2	0.0276
	Min	2473	99.6	623.1	545.6	477.2	414.8	363.5	294.9	0.0269
	Rod or Quadrant #			DT	2	4	2	2 (top)		
	z-Location (m)			1.22	0.91	1.22	1.22	1.22		
0.0	**Average**	**2500**	**99.8**	**647.0**	**562.5**	**485.9**	**420.0**	**367.2**	**296.7**	**0.0277**
	Max	2519	100.0	647.1	562.7	486.1	420.5	367.9	300.9	0.0280
	Min	2484	99.6	646.9	562.4	485.6	419.6	366.6	294.7	0.0268
	Rod or Quadrant #			DT	2	2	2	2 (top)		
	z-Location (m)			0.61	0.91	1.22	1.22	1.22		

Table 3.4 Steady-state results for various components for the 5.00 kW tests for all helium/air gas backfill compositions.

Mole Fraction He, Balance Air		Power (W)	Pressure (kPa)	PCT (K)	Channel (K)	Basket (K)	Vessel (K)	Vault (K)	Ambient (K)	Tot. Flow Rate (kg/s)
1.0	**Average**	**5002**	**99.8**	**694.0**	**618.3**	**555.3**	**492.5**	**416.1**	**293.7**	**0.0354**
	Max	5054	100.1	694.3	618.5	555.6	492.9	416.7	296.9	0.0358
	Min	4976	99.6	693.7	617.8	554.9	491.9	415.6	292.3	0.0350
	Rod or Quadrant #			DT	2	4	2	2 (top)		
	z-Location (m)			1.22	1.22	1.22	0.91	1.22		
0.9	**Average**	**5000**	**99.8**	**703.4**	**625.3**	**560.4**	**492.5**	**415.5**	**297.3**	**0.0370**
	Max	5032	100.1	704.3	625.9	560.8	492.9	416.8	301.5	0.0374
	Min	4974	99.6	702.6	624.6	560.2	491.9	414.0	295.1	0.0365
	Rod or Quadrant #			DT	2	4	2	2 (top)		
	z-Location (m)			1.22	0.91	1.22	0.91	1.22		
0.5	**Average**	**5000**	**99.8**	**733.4**	**643.7**	**567.4**	**488.6**	**414.4**	**297.0**	**0.0352**
	Max	5035	100.0	733.8	644.0	567.6	488.9	414.9	299.8	0.0358
	Min	4948	99.6	733.0	643.3	566.7	487.9	413.4	294.8	0.0347
	Rod or Quadrant #			DT	2	4	2	2 (top)		
	z-Location (m)			0.61	0.91	1.22	0.91	1.22		
0.1	**Average**	**5000**	**99.8**	**762.4**	**664.5**	**576.6**	**490.2**	**415.8**	**297.5**	**0.0355**
	Max	5063	100.0	763.0	664.8	577.3	491.3	417.0	300.9	0.0359
	Min	4960	99.6	761.9	663.9	575.5	488.6	414.2	295.5	0.0351
	Rod or Quadrant #			DT	2	2	2	2 (top)		
	z-Location (m)			0.61	0.91	1.22	1.22	1.22		
0.0	**Average**	**5000**	**99.8**	**781.9**	**678.0**	**585.4**	**496.5**	**420.9**	**298.6**	**0.0359**
	Max	5021	100.0	782.6	678.6	585.9	497.7	422.0	305.0	0.0363
	Min	4969	99.6	781.2	677.5	584.6	495.4	419.9	296.0	0.0351
	Rod or Quadrant #			DT	2	2	2	2 (top)		
	z-Location (m)			0.61	0.91	1.22	1.22	1.22		

3.2 Temperature Profiles

3.2.1 Centerline Fuel Axial Temperature Profile – T*(z)*

Figure 3.1 shows an example centerline fuel axial temperature profile, on which all axial temperature profiles in this section are based. This axial temperature profile is from the 2.50 kW, 100 kPa helium test. This figure is provided to visualize the locations of the thermocouples used to produce the axial temperature profile. As indicated on the inset of the fuel bundle cross-section shown in the figure, the profiles are produced along the axial length of the center of the assembly, at the water rod at location EU (see rod-naming convention in Figure 2.9).

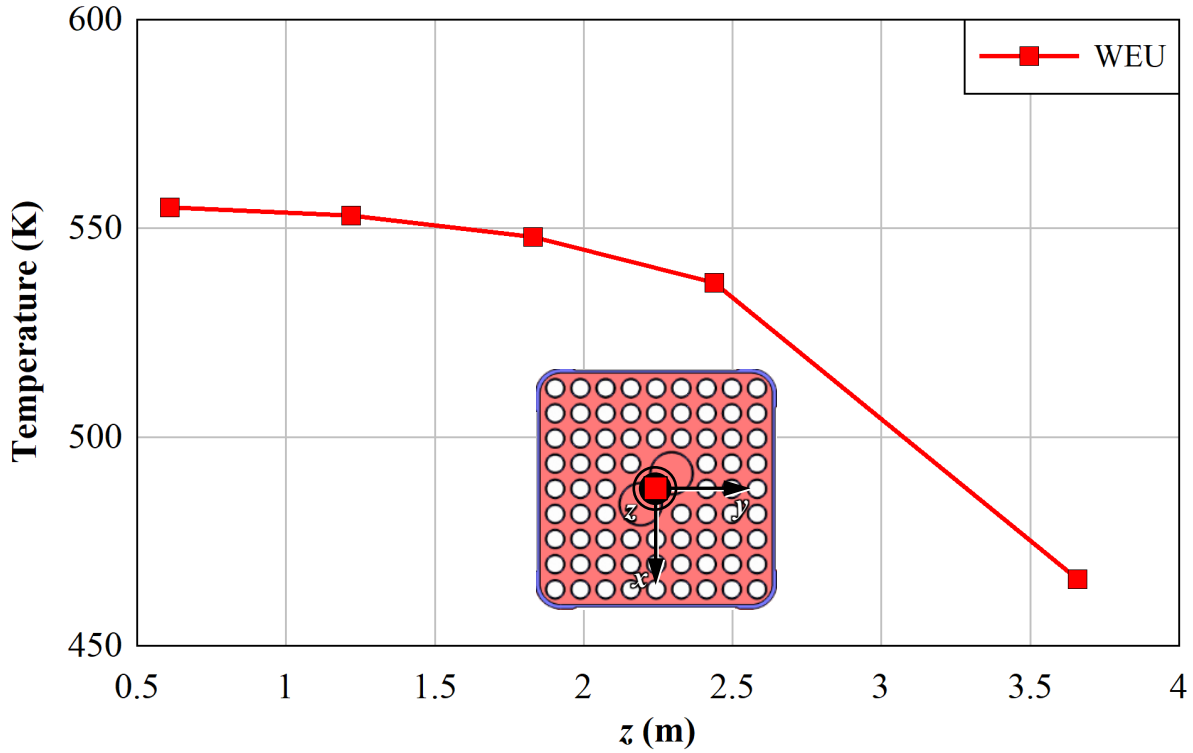

Figure 3.1 Example centerline fuel axial temperature profile including the position label for the TC at WEU.

The steady-state centerline fuel axial temperature profiles for the 0.50, 1.00, 2.50, and 5.00 kW tests are shown in Figure 3.2, Figure 3.3, Figure 3.4, and Figure 3.5, respectively. The data presented in the figures is tabulated in Appendix D.1. The water rod at location EU was chosen for comparison of the results between tests using different helium/air concentrations. This location was chosen previously when comparing experimental data to modeling results in the HDCS model validation exercise (Pulido *et al.*, 2020b), so the same location was chosen in this report for consistency.

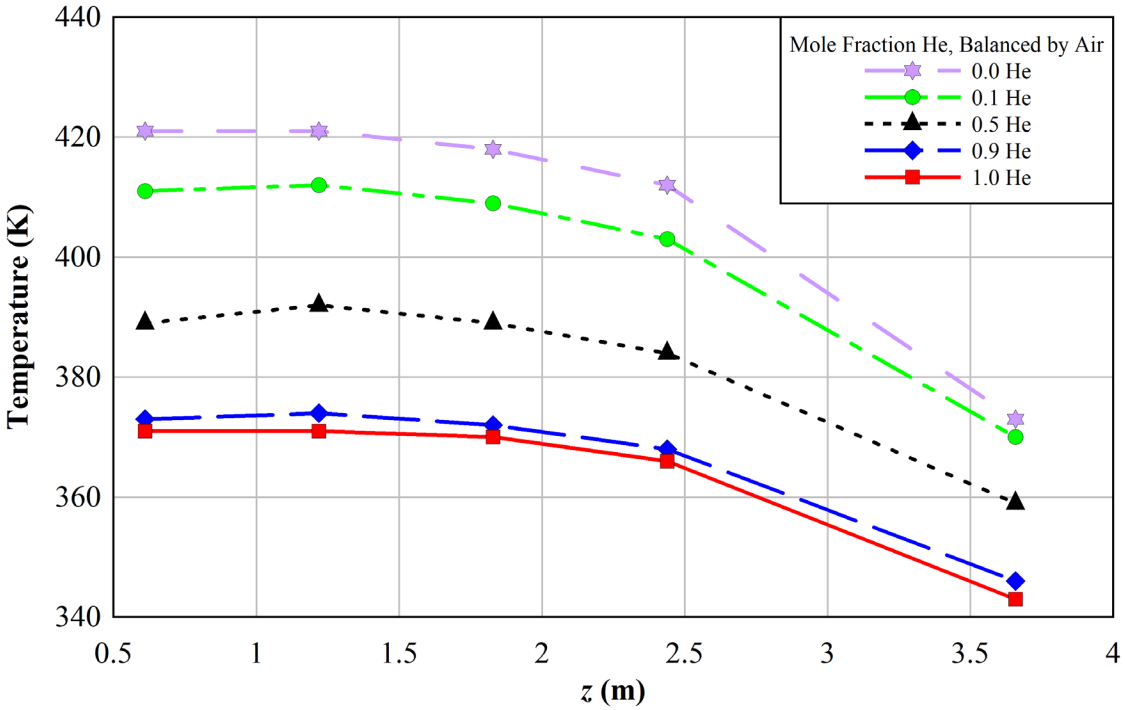

Figure 3.2 **Centerline fuel temperature profile as a function of z for 0.50 kW and all helium/air backfill compositions at 100 kPa.**

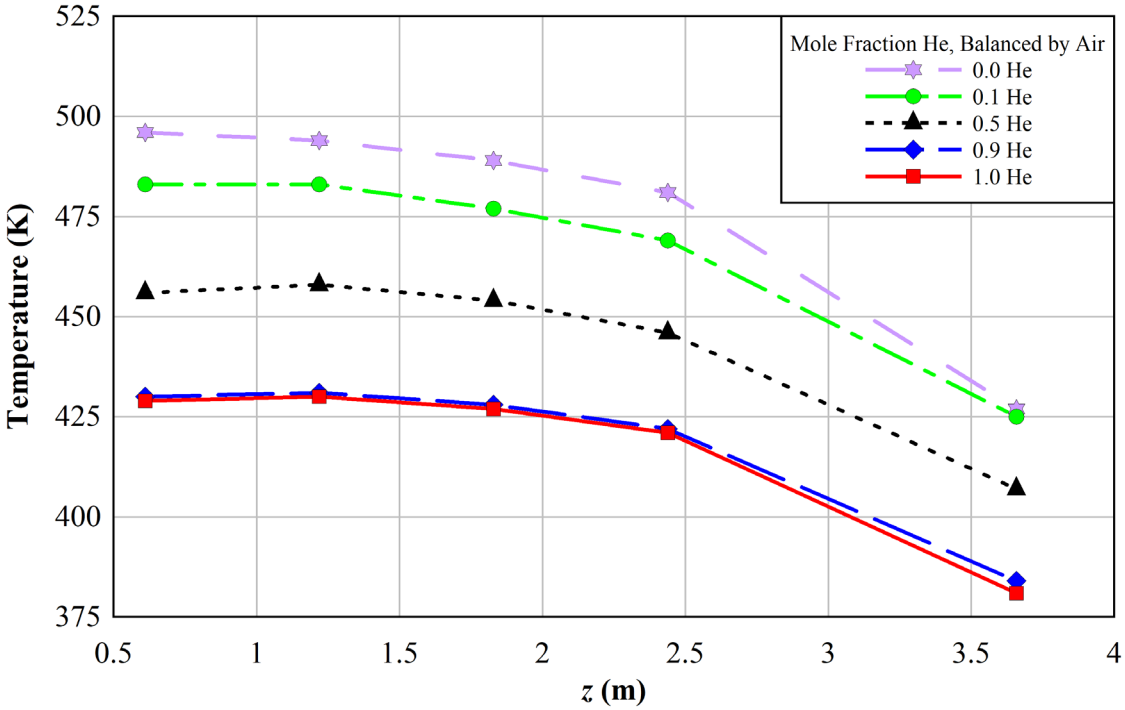

Figure 3.3 **Centerline fuel temperature profile as a function of z for 1.00 kW and all helium/air backfill compositions at 100 kPa.**

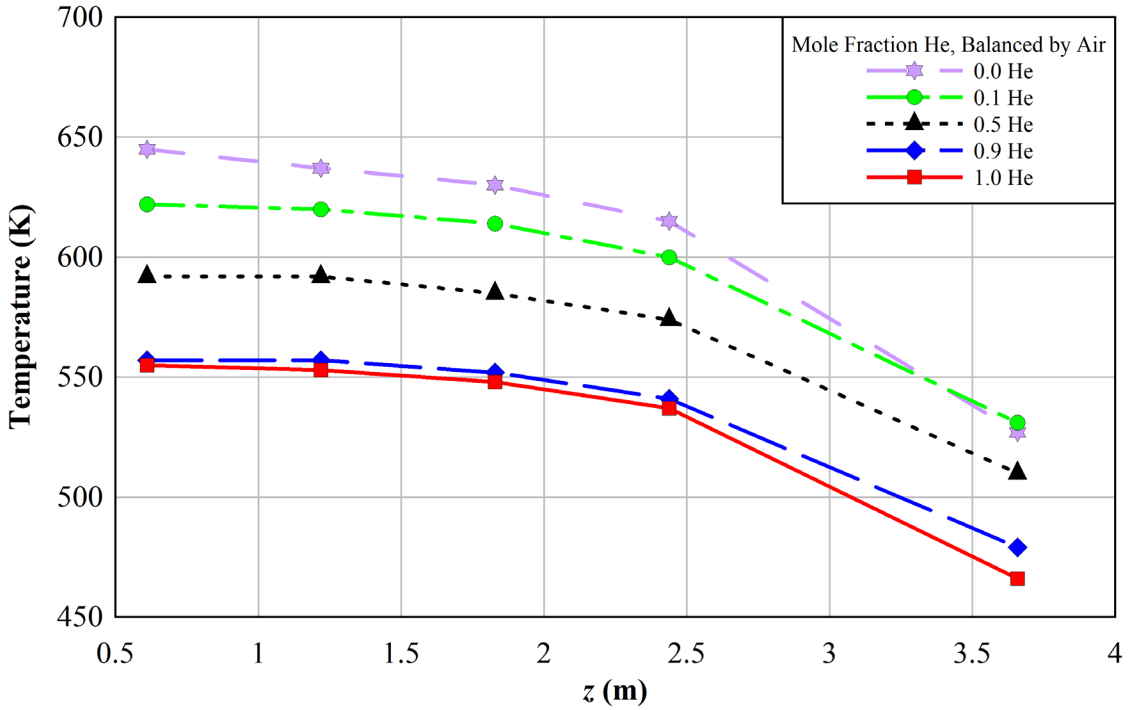

Figure 3.4 **Centerline fuel temperature profile as a function of z for 2.50 kW and all helium/air backfill compositions at 100 kPa.**

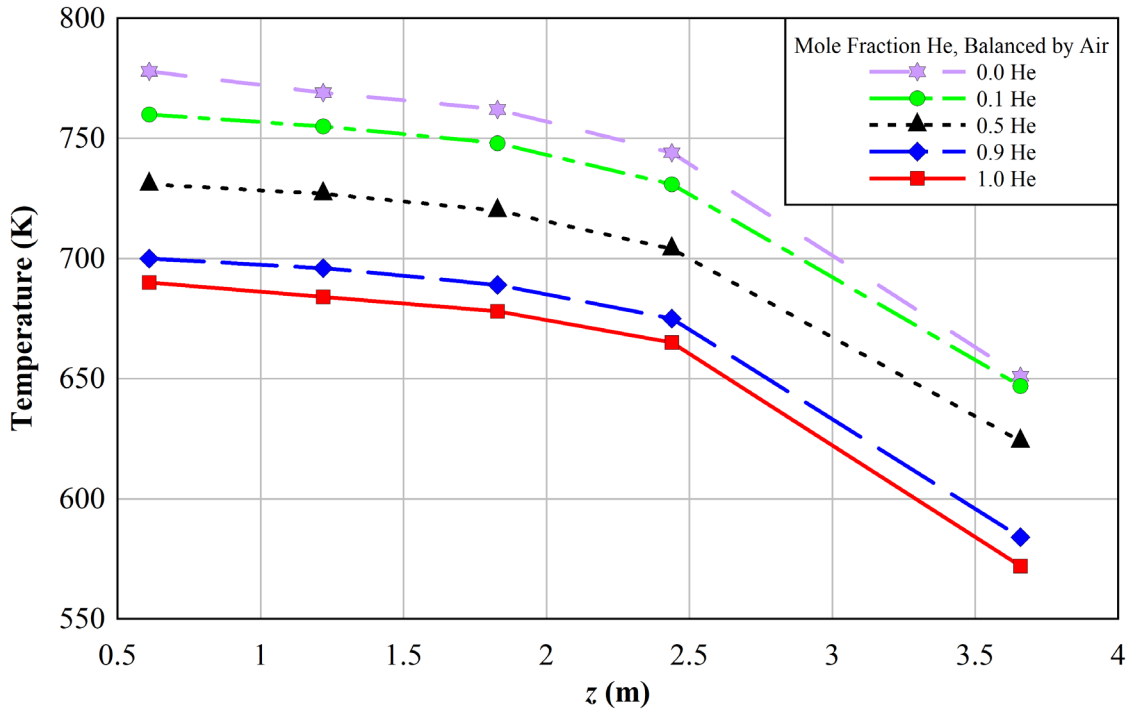

Figure 3.5 **Centerline fuel temperature profile as a function of z for 5.00 kW and all helium/air backfill compositions at 100 kPa.**

The temperatures in the fuel bundle steadily increased with decreasing helium concentration for all powers. This was expected, due to helium's superior thermal conductivity over air (155.7 versus 26.4 mW/m·K at 300 K) [Huber and Harvey, 2011]. It can thus be inferred, then, that during a loss of helium backfill from a horizontal dry storage system, the temperatures within the fuel bundle across its axial length will increase. The shapes of the axial profiles are similar across all tests, with the highest temperatures located towards the z = 0 m axial location, and the temperature gradient steadily decreasing towards the z = 4 m mark due to the partial-length rods. As noted in Section 2.3, these partial-length rods run two-thirds the length of the assembly and end at z = 2.6 m.

3.2.2 Canister Axial Temperature Profile – T*(z)*

The temperatures on the surface of the canister along its axial length are explored in this section. These temperatures were investigated to look into the possibility of detecting changes in the thermal properties of the components interior to the canister based on changes in the surface temperatures.

Figure 3.6 shows an example of a canister axial temperature profile. This profile is from the 2.50 kW, 100 kPa helium test. The inset indicates the locations of the TCs along the canister and the orientation of gravity. The axial temperature profiles are generated from the thermocouples placed along the bottom of the canister (Quadrant 4), which faces towards the floor of the vault (see Figure 2.10 for quadrant naming convention). Quadrant 4 was chosen since it had the most uniform TC distribution among all quadrants (see Figure 2.13 for TC locations on the pressure vessel representing the canister).

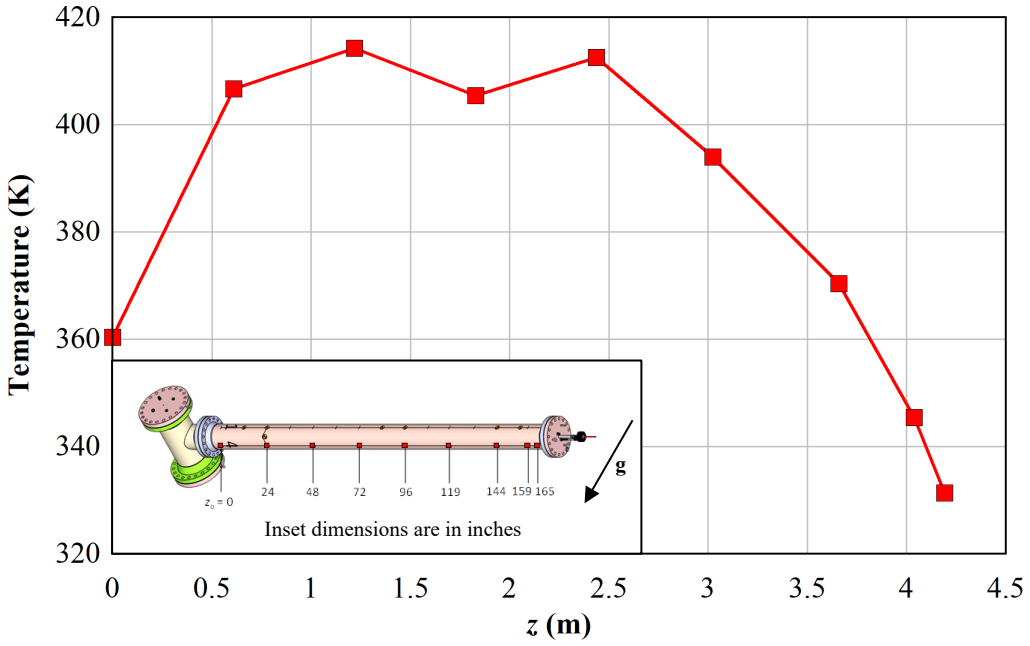

Figure 3.6 Example canister axial temperature profile, with the thermocouple locations generating temperature data for the profile indicated in the inset.

The steady-state internal fuel bundle axial temperature profiles for the 0.50, 1.00, 2.5, and 5.00 kW tests are shown in Figure 3.7, Figure 3.8, Figure 3.9, and Figure 3.10, respectively. The data presented in the figures is tabulated in Appendix D.2. The uncertainty bars are the uncertainties in temperature for those tests, based on 1% of the maximum canister surface temperature for a given power (see Appendix A for details and for the uncertainty values). These uncertainties are plotted for the 0.0 He results, which, for a given power, have the maximum uncertainties across helium mole fractions.

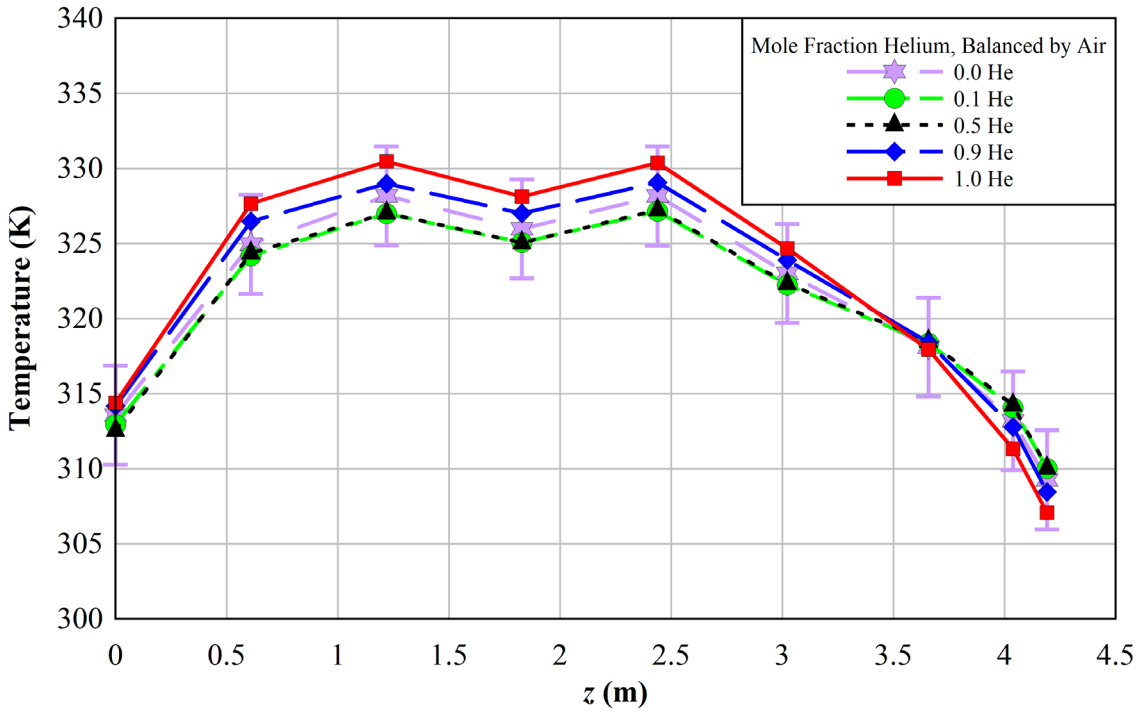

Figure 3.7 Canister axial temperature profile for 0.50 kW and all helium/air backfill compositions at 100 kPa.

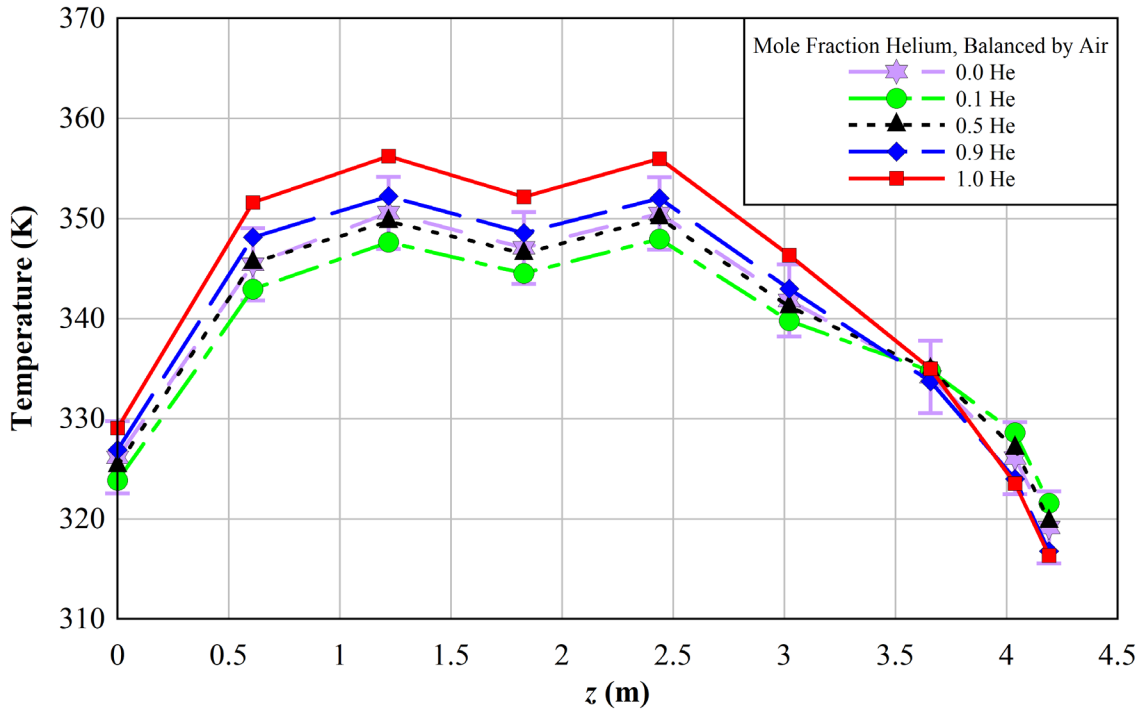

Figure 3.8 Canister axial temperature profile for 1.00 kW and all helium/air backfill compositions at 100 kPa.

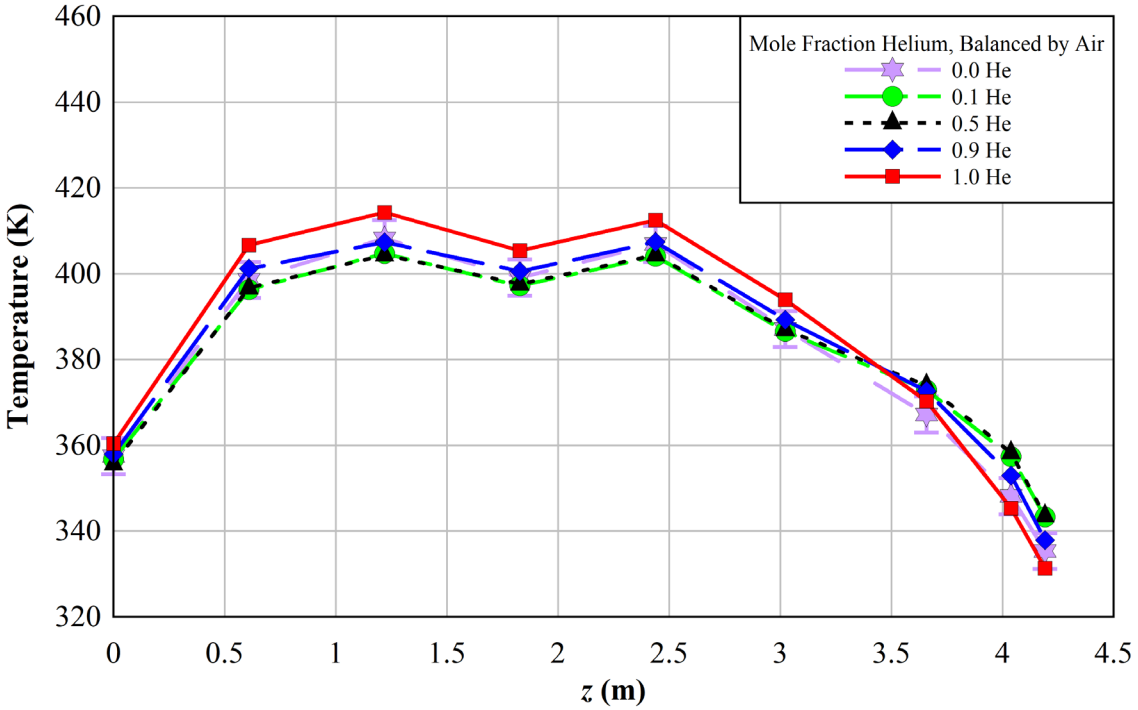

Figure 3.9 Canister axial temperature profile for 2.50 kW and all helium/air backfill compositions at 100 kPa.

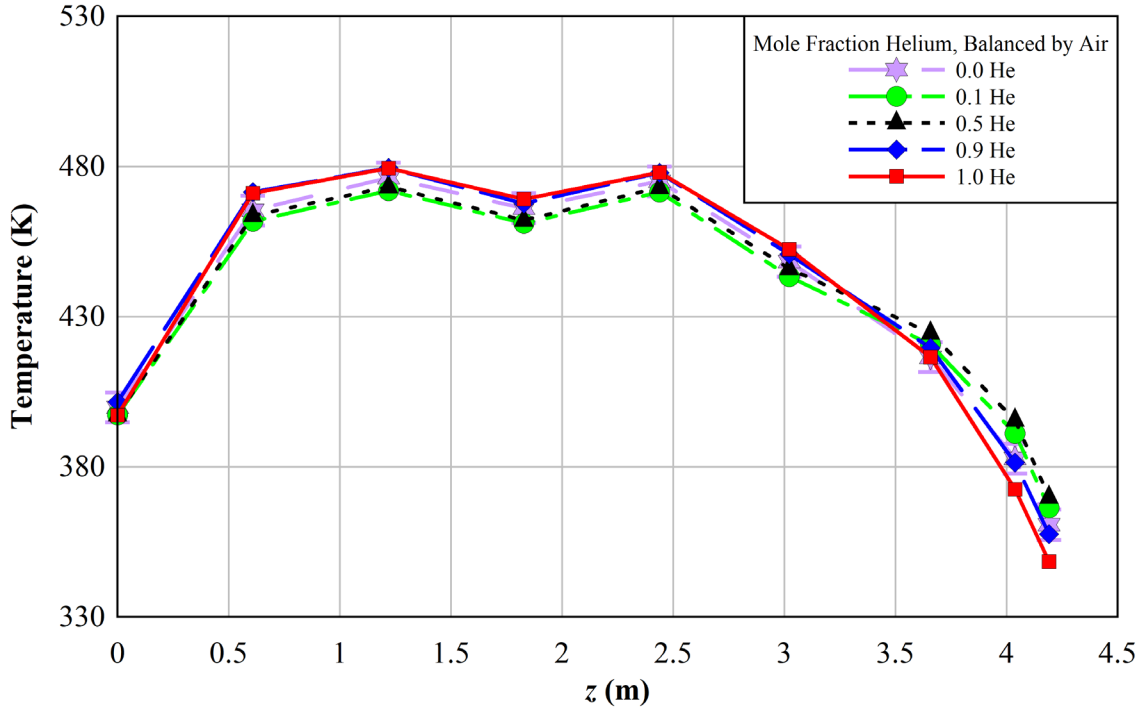

Figure 3.10 Canister axial temperature profile for 5.00 kW and all helium/air backfill compositions at 100 kPa.

These plots show that across all canister axial temperature profiles, the results are largely the same across helium mole fractions for any given power, and the majority of data points across helium mole fractions for a given power at any given location are bounded by the upper and lower uncertainty bounds from the 0.0 He tests. Based on these results, monitoring canister surface temperatures may be inadequate for detecting changes in temperature within the fuel assembly as helium backfill is lost and subsequently replaced by air, since the temperatures stay largely similar at the majority of data points (especially for the highest temperatures along the profiles) regardless of helium mole fraction.

3.2.3 Vertical Temperature Profile – T*(x)*

An example vertical temperature profile is provided in Figure 3.11. The scaled inset figure on the right shows the location of the thermocouples. The profile passes through the center line of the apparatus along the *x*-axis at $z = 1.219$ m. TCs are located on the top and bottom of the vault enclosure, pressure vessel, storage basket and channel box. TCs are also located inside the assembly on the water rods and heater rods, ES and EQ (see Figure 2.9 for heater rod naming convention).

The vertical temperature profiles for the 0.50, 1.00, 2.50, and 5.00 kW test cases are shown in Figure 3.12, Figure 3.13, Figure 3.14, and Figure 3.15 respectively. The data used to generate these plots is tabulated in Appendix D.2. Note that Figure 3.12 through Figure 3.15 have different temperature scales in order to distinguish the profile features in each plot.

The uncertainty bars at each data point are the uncertainties in temperature at each location, which is 1% of the measured temperature. For all powers, the uncertainties are plotted for the 0.0 He tests, which have the highest fuel temperatures across all tests for a given power.

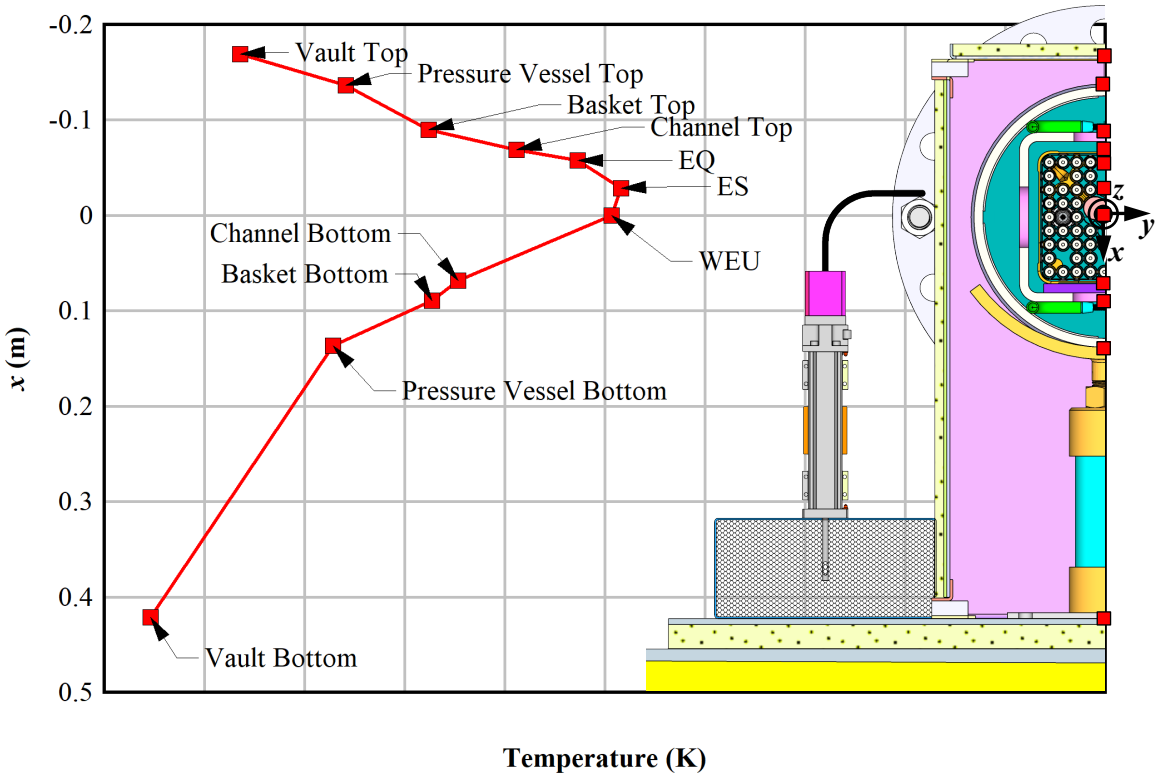

Figure 3.11 Example vertical temperature profile including measurement location labels.

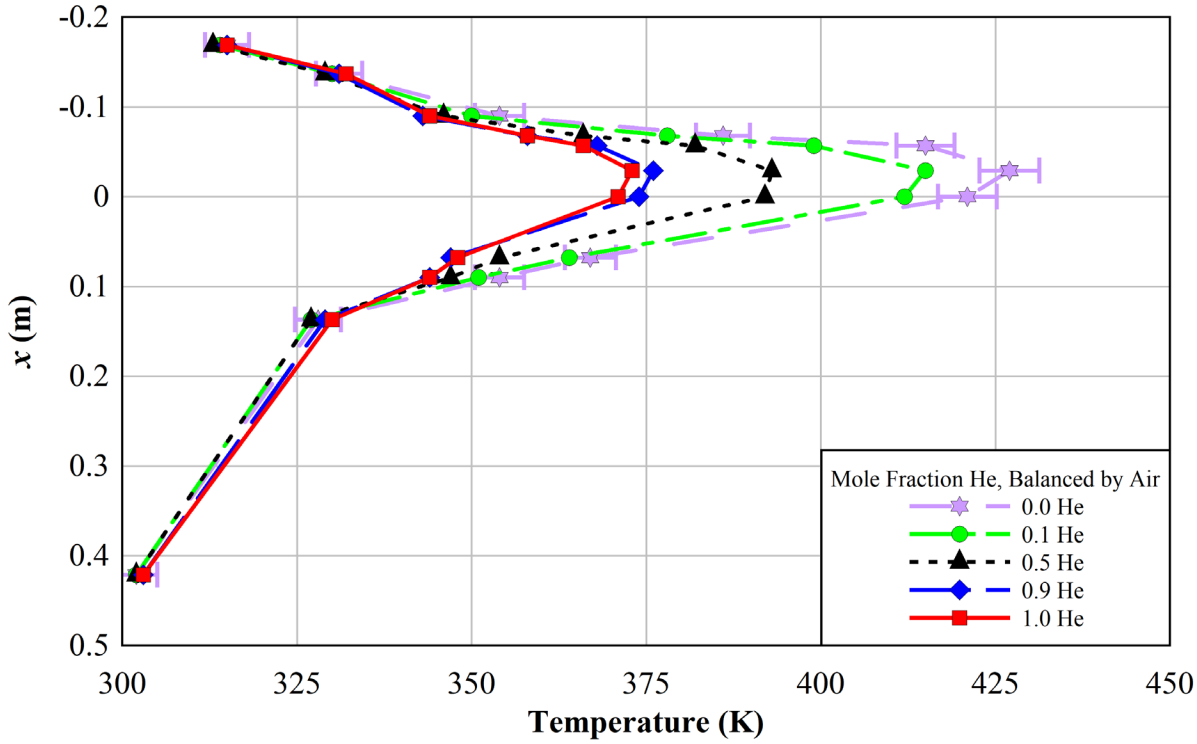

Figure 3.12 Vertical temperature profile for the 0.50 kW tests at z = 1.219 m (48.0 in.).

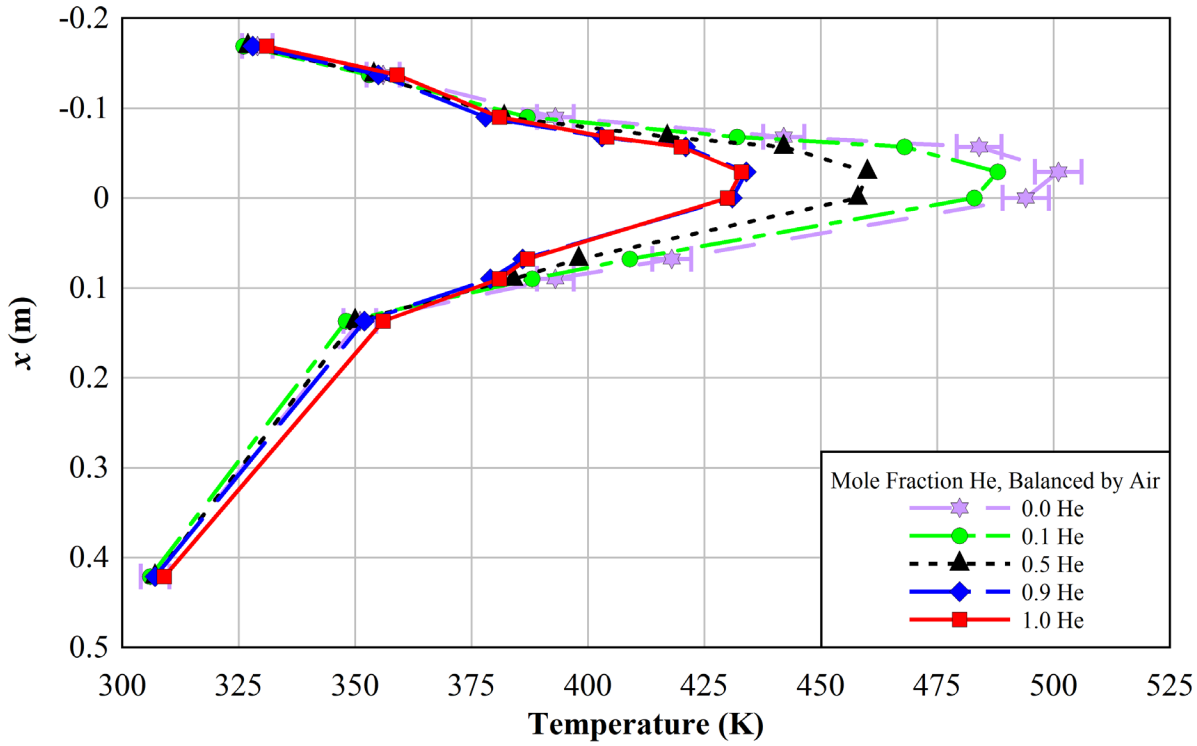

Figure 3.13 Vertical temperature profile for the 1.00 kW tests at z = 1.219 m (48.0 in.).

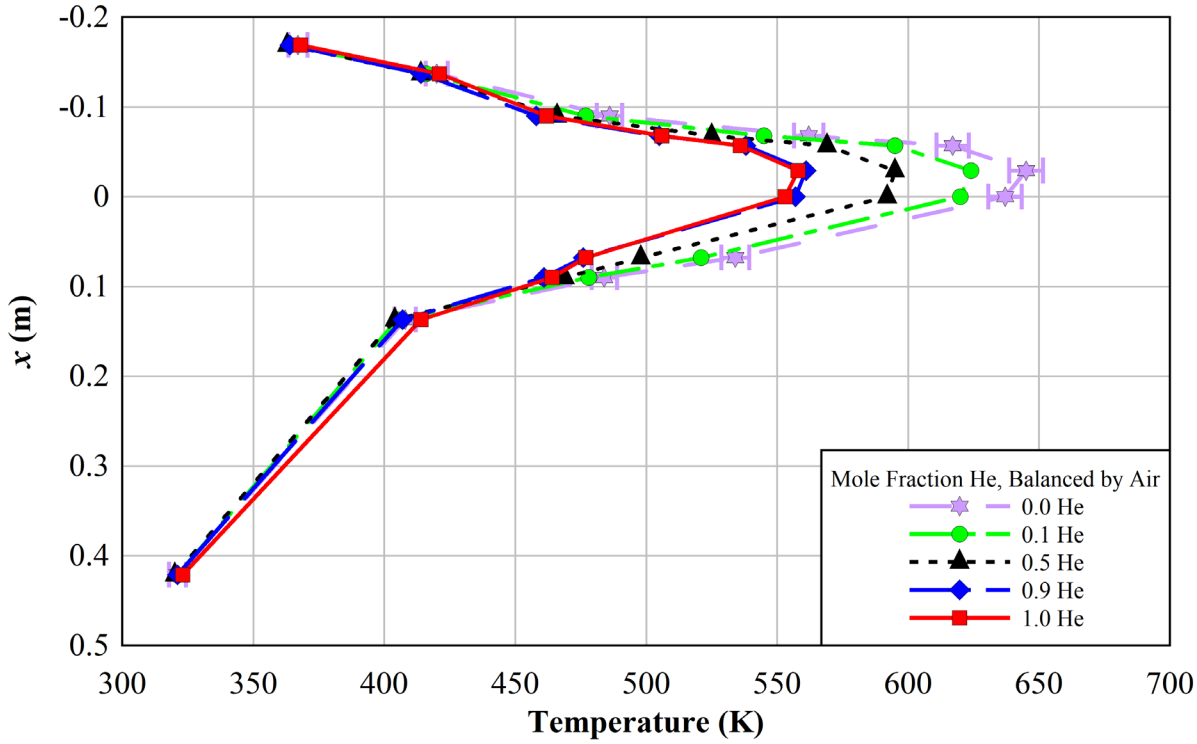

Figure 3.14 Vertical temperature profile for the 2.50 kW tests at z = 1.219 m (48.0 in.).

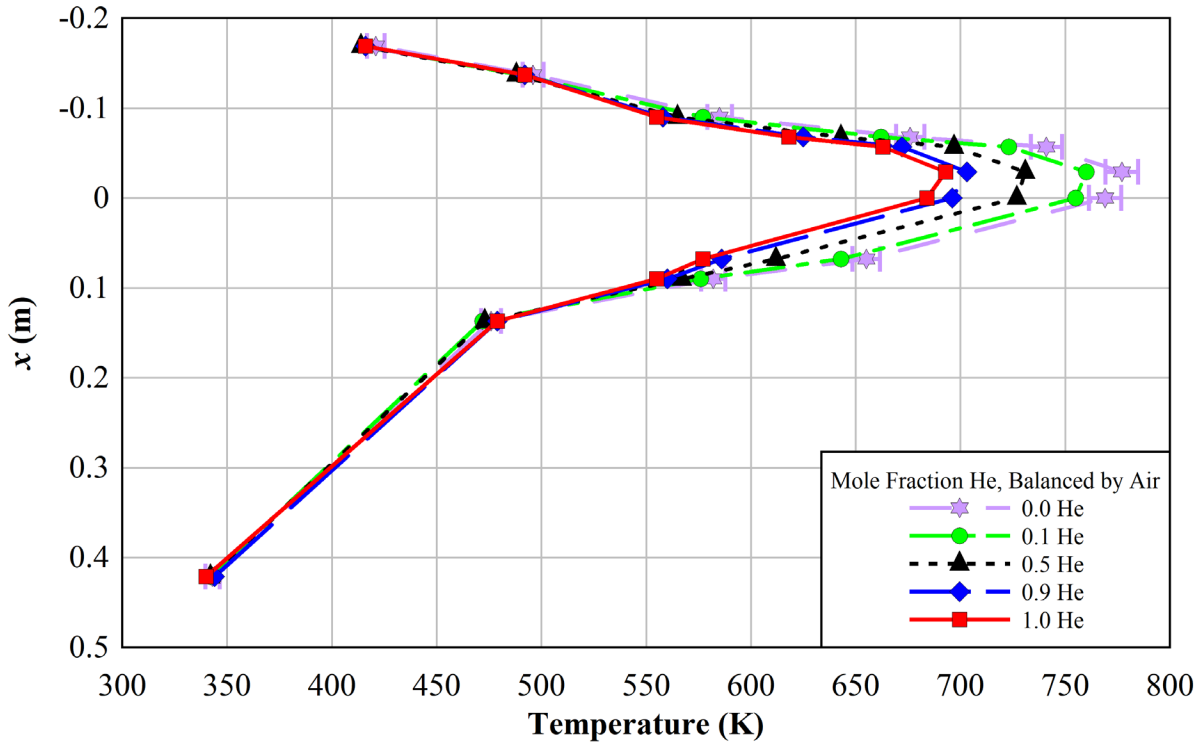

Figure 3.15 Vertical temperature profile for the 5.00 kW tests at z = 1.219 m (48.0 in.).

The peak temperature for all cases was located on rod ES. For all test cases, the basket top temperature is higher than the basket bottom temperature, although the differences are minor. More significant is the temperature difference between the bottom of the storage basket and the bottom of the channel box. As the helium mole fraction decreases, this temperature difference increases, indicating much better thermal coupling by the aluminum bridge plate when the gap between the bridge plate and the channel box (see Figure 2.2) has more helium. The temperature differences between tests with different helium mole fractions diminish at the pressure vessel for all powers, suggesting that the pressure vessel temperatures are independent of helium mole fraction and depend primarily on the power. This is evidenced by the majority of temperature data points at the pressure vessel and vault being bounded by the uncertainty bars from the 0.0 He tests.

3.2.4 Horizontal Temperature Profile – T*(y)*

An example of the horizontal temperature profiles measured for all tests is shown in Figure 3.16. The unscaled inset figure in the bottom left shows the locations of the thermocouples. The profile passes through the center line of the apparatus along the *y*-axis at $z = 1.829$ m. The profile starts in the center of the assembly and proceeds out through Quadrant 3 in the positive *y*-direction. The TCs shown in the plot are located on a water rod near the center of the fuel assembly, heater rods GU and IU (see Figure 2.9 for heater rod naming convention), as well as the channel box, basket, pressure vessel, and vault wall.

The horizontal temperature profiles for the 0.50, 1.00, 2.50, and 5.00 kW tests are shown in Figure 3.17, Figure 3.18, Figure 3.19, and Figure 3.20, respectively. The data used to generate these plots are tabulated in Appendix D.4.

The uncertainty bars at each data point are the uncertainties in temperature at each location, which is 1% of the measured temperature. For all powers, the uncertainties are plotted for the 0.0 He tests, which have the highest fuel temperatures across all tests for a given power.

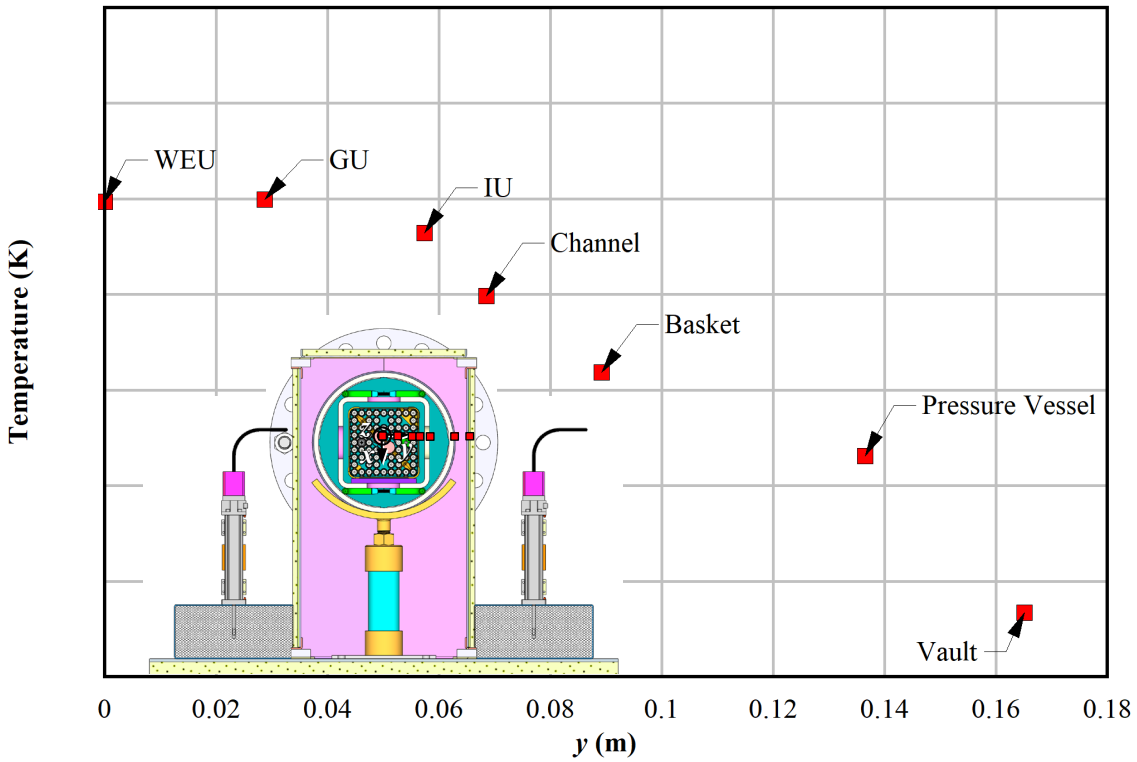

Figure 3.16 Example horizontal temperature profile including position labels.

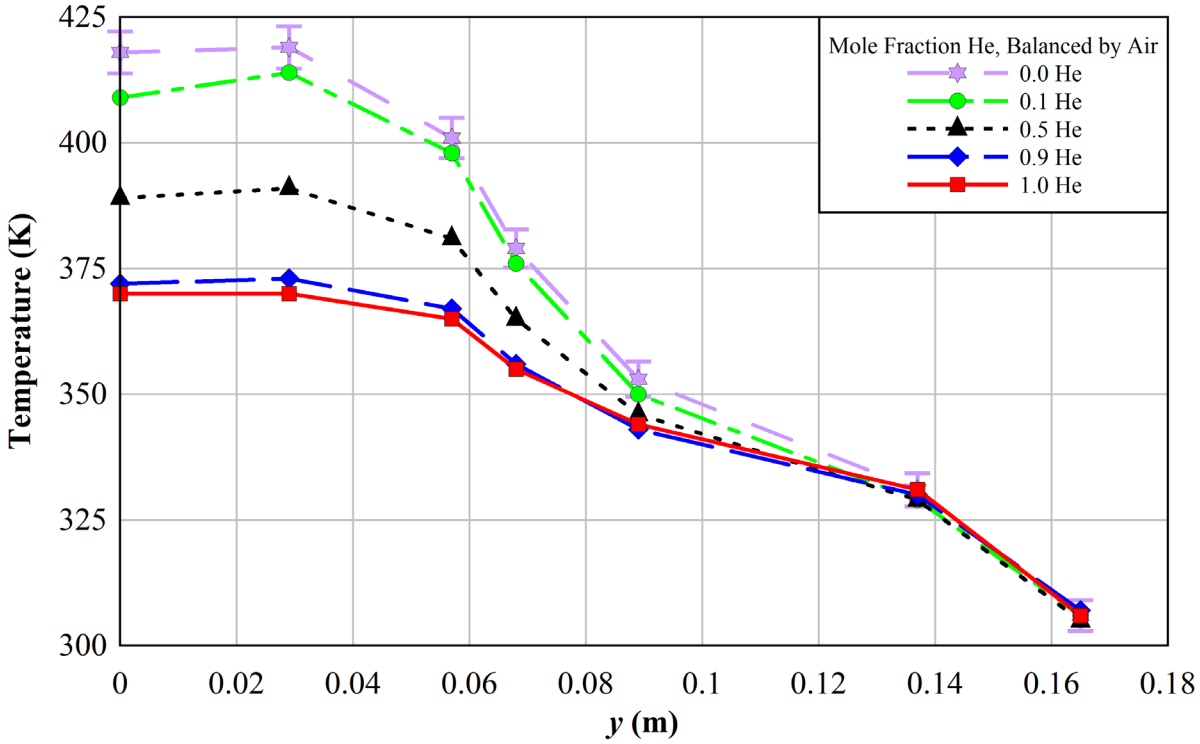

Figure 3.17 Horizontal temperature profiles for the 0.50 kW tests at z = 1.829 m (72.0 in.).

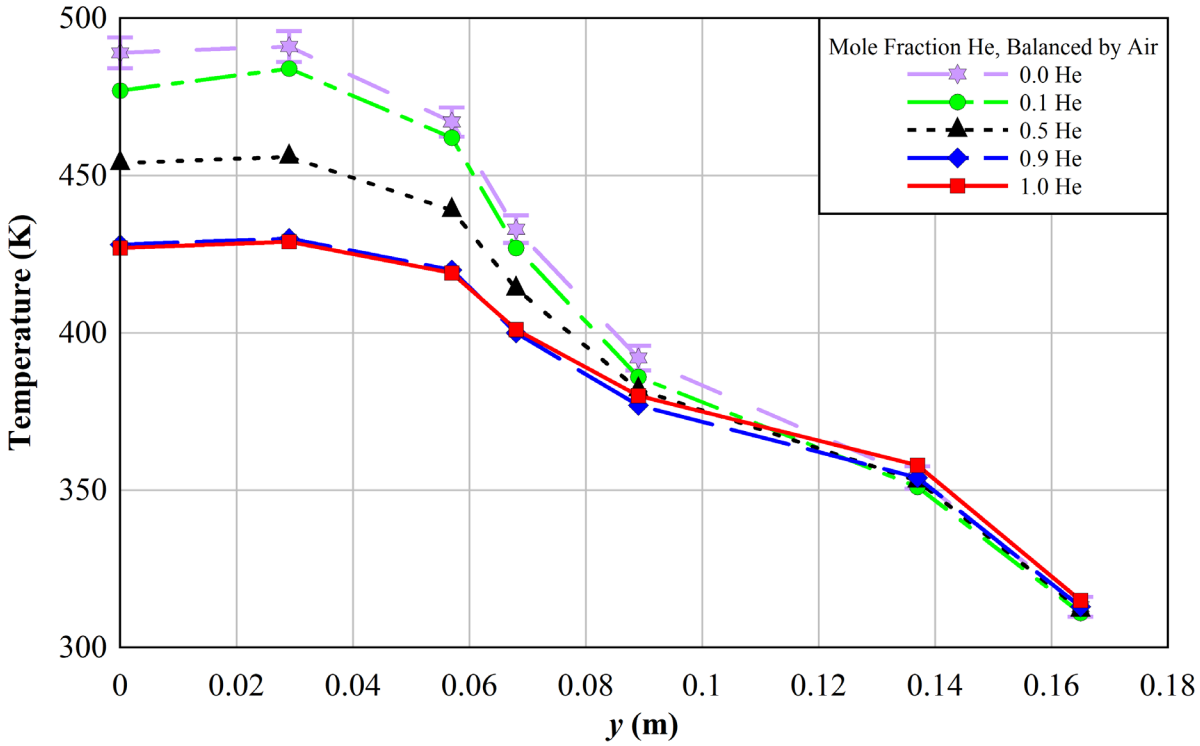

Figure 3.18 Horizontal temperature profiles for the 1.00 kW tests at z = 1.829 m (72.0 in.).

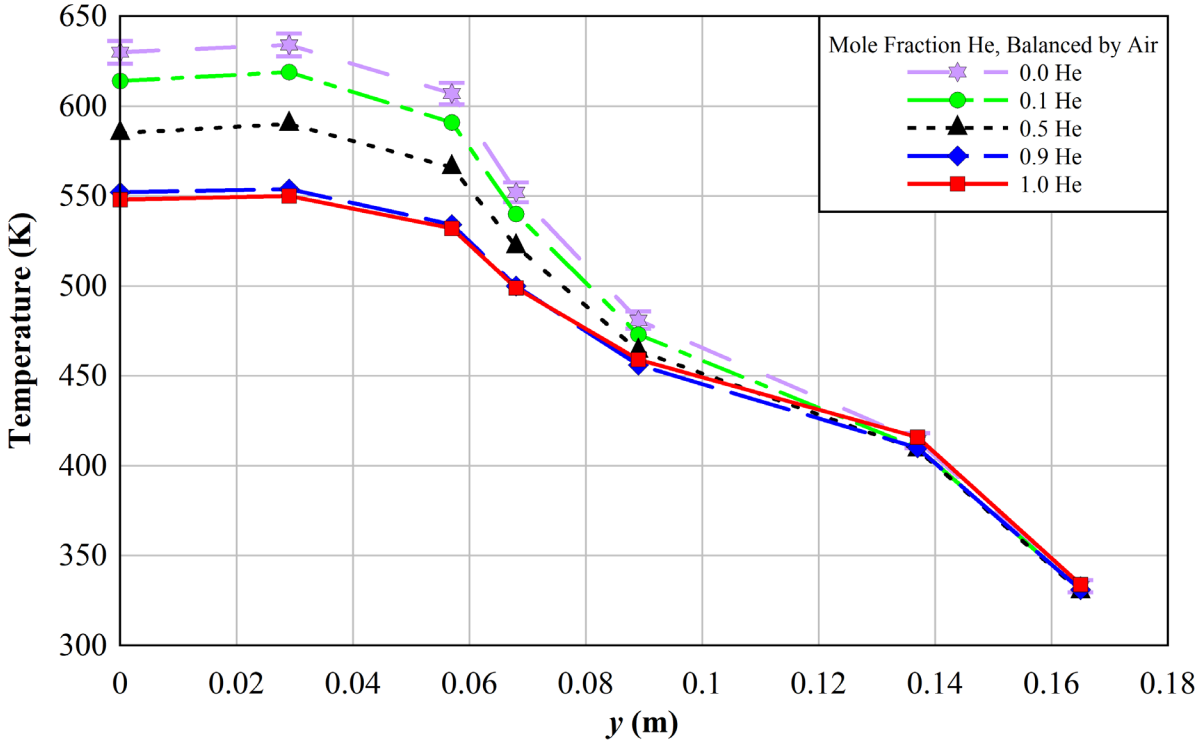

Figure 3.19 Horizontal temperature profiles for the 2.50 kW tests at z = 1.829 m (72.0 in.).

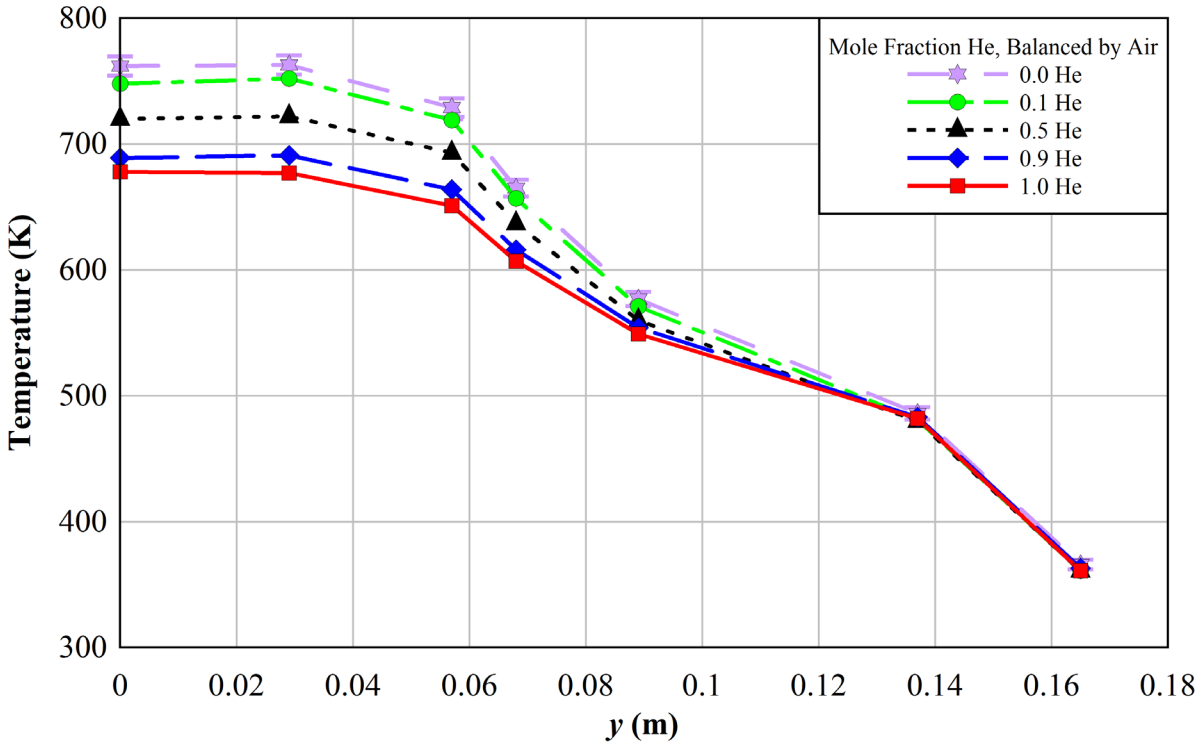

Figure 3.20 Horizontal temperature profiles for the 5.00 kW tests at z = 1.829 m (72.0 in.).

As was the case with the vertical temperature profiles, the temperature differences between tests of different mole fractions of helium for a given power are largest for the fuel region. These differences diminish as the horizontal temperature profile approaches the outlying structures. The temperature differences are essentially eliminated once the profiles reach the pressure vessel (canister), as evidenced by the majority of temperature data points at the pressure vessel and vault being bounded by the uncertainty bars from the 0.0 He tests. This suggests that the pressure vessel temperatures are independent of helium mole fraction and depend primarily on the power.

3.3 Key Comparison Metrics Versus Mole Fraction Helium

As observed in the previous sections of this chapter, the primary thermal-hydraulic effect associated with a loss of helium backfill in a horizontal dry storage canister is an increase in temperatures within the fuel assembly as helium is replaced by air. This effect drops off in regions outside of the fuel, where the temperatures are largely the same at the pressure vessel (canister) for tests using a given power. The key comparison metrics versus mole fraction helium are further explored in this section.

3.3.1 Peak Cladding Temperature Versus Helium Mole Fraction

Figure 3.21 shows the peak cladding temperature from each test considered in this report versus helium mole fraction. Here, a zero helium mole fraction means that only air is present inside the canister, and this is representative of a complete loss of helium backfill. The four data sets are the four powers considered in this report's test series, while the data points represent the PCT at each helium mole fraction. The lower and upper uncertainty bounds are unique for each power and are representative of the maximum uncertainty (1% of the PCT) across all mole fractions of helium for a given power, which occurs when the mole fraction of helium is zero (refer to Appendix A for those uncertainties). The differences in the temperatures for a given power across the mole fractions of helium, which between the 1.0 He and the 0.0 He test cases as well as between the 0.9 He and the 0.1 He test cases are larger than the uncertainties, show that the PCT undergoes a significant change based on the mole fraction of helium in the canister. This implies that a loss of helium backfill results in increased temperatures within the fuel assembly.

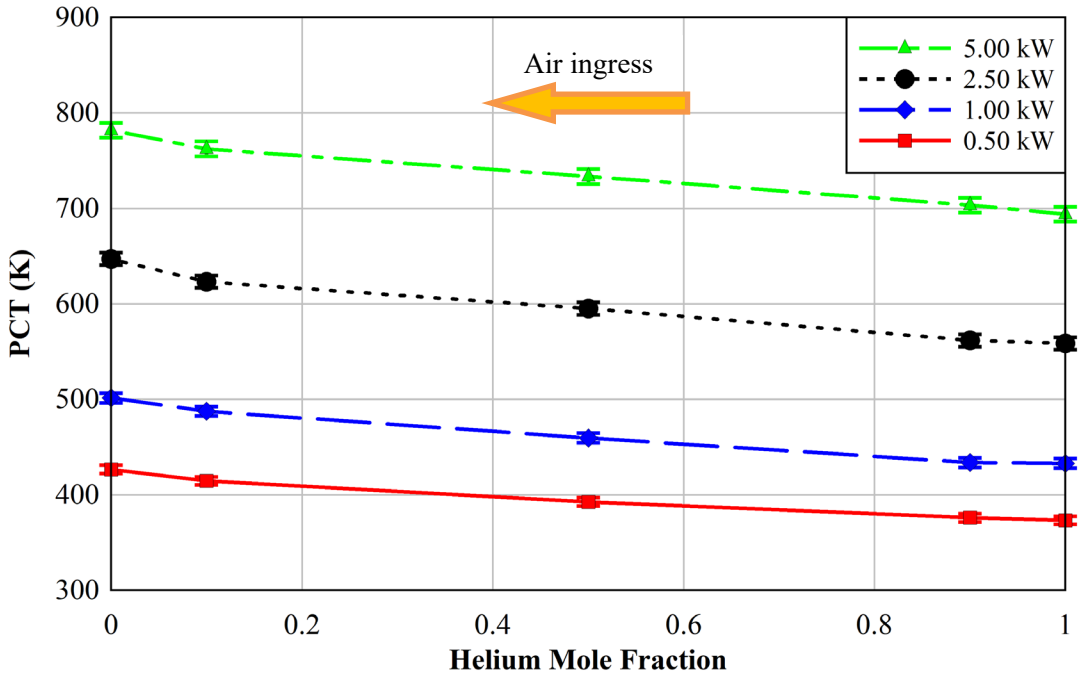

Figure 3.21 Peak cladding temperature versus helium mole fraction.

3.3.2 Total Air Mass Flow Rate Versus Helium Mole Fraction

Figure 3.22 shows total air mass flow rate versus helium mole fraction for the twenty test cases. The upper and lower uncertainty bounds shown are the uncertainty in the total air mass flow rate, $U_{\dot{m},\,Total} = \pm 3.0 \times 10^{-4}$ kg/s (see Appendix A for details). The overlap in uncertainty bounds between data points representing different mole fractions of helium for a given power (data points of the same color) show that the total air mass flow rate is independent of the mole fraction of helium, and the total air mass flow rate increases with increasing power and subsequent increasing thermal gradient between the fuel assembly and the surrounding environment.

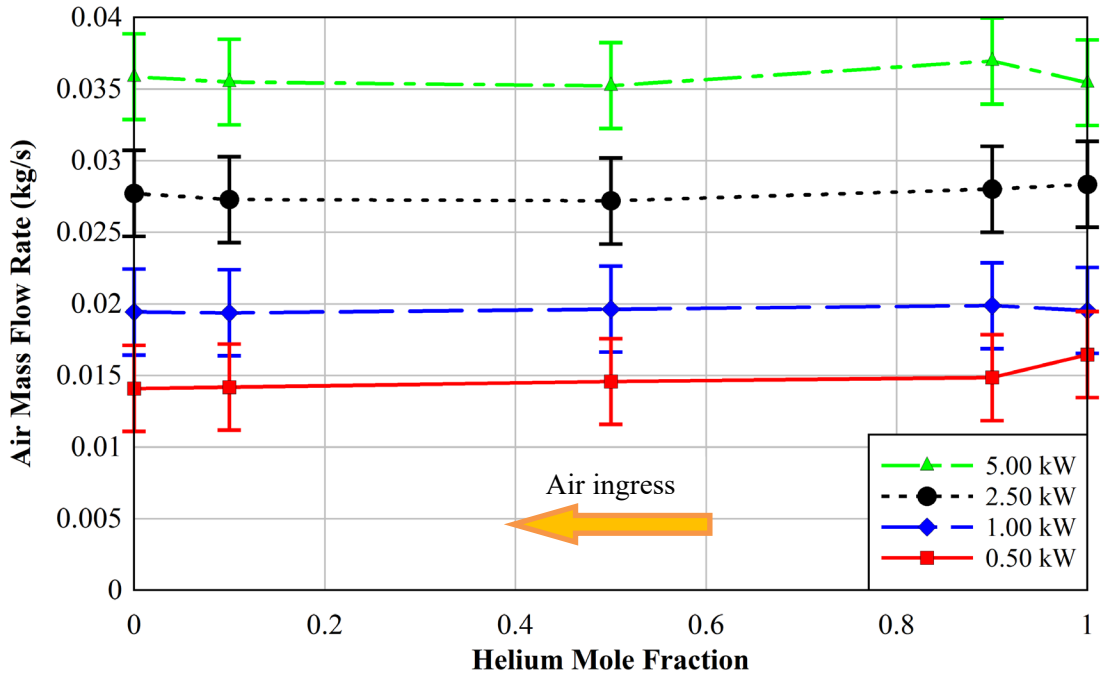

Figure 3.22 Total air mass flow rate versus helium mole fraction.

3.3.3 Canister/Ambient Temperature Difference Versus Helium Mole Fraction

The convective potential is explored further in Figure 3.23, which shows the temperature difference between the canister surface and the ambient temperatures for each of the twenty test cases. This parameter was investigated in order to note any similarities or differences in the temperature differences outside of the fuel assembly. The uncertainty bounds are defined as previously for the PCT – they are given as the maximum uncertainty in temperature (1% of the maximum canister temperature measurement for a given power across all helium mole fractions). For all powers, the uncertainty was calculated using 1% of the maximum canister temperature of the air test, since the air tests had the highest temperatures. As was the case with the total air mass flow rate, the overlap in uncertainty bounds between test cases for a given power show that the canister/ambient temperature difference is also independent of the mole fraction of helium. Larger temperature differences are associated with larger powers – these larger differences are associated with higher assembly temperatures versus ambient temperatures, because the ambient temperatures differed only by a few degrees Kelvin across all tests.

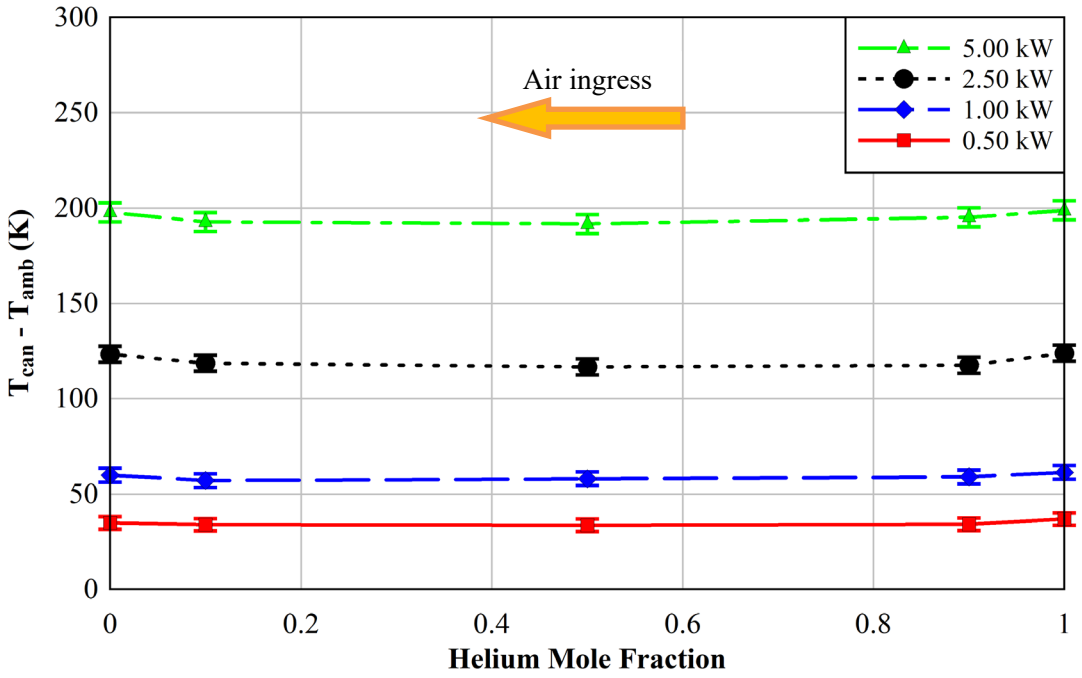

Figure 3.23 Canister/ambient temperature difference versus helium mole fraction.

3.3.4 Inlet/Outlet Duct Temperature Difference Versus Helium Mole Fraction

Figure 3.24 gives a measure of the sensible heat of the cooling air flow for the twenty test cases – this plot analyzes the temperature difference between the inlet and outlet ducts of the vault enclosure. The uncertainty bounds are the maximum uncertainty in temperature (1% of the maximum of the inlet and outlet duct temperatures, which for all test cases was 1% of the outlet duct temperatures) across the tests with varying mole fractions of helium for a given power. The outlet duct temperatures were largely the same across helium mole fractions for a given power, as shown by the similar uncertainties in outlet duct temperatures (Table A.3 in Appendix A). For consistency with the previous plot, the uncertainties in temperature were plotted for the 0.0 He tests for each power. As with the previous two plots, the overlapping uncertainty bounds across all tests for a given power show that this temperature difference is independent of the helium mole fraction. The larger temperature differences for larger powers once again show the effects of higher fuel assembly temperatures resulting from a decrease in helium mole fraction, which introduce larger temperature gradients between the fuel assembly and the outlying structures.

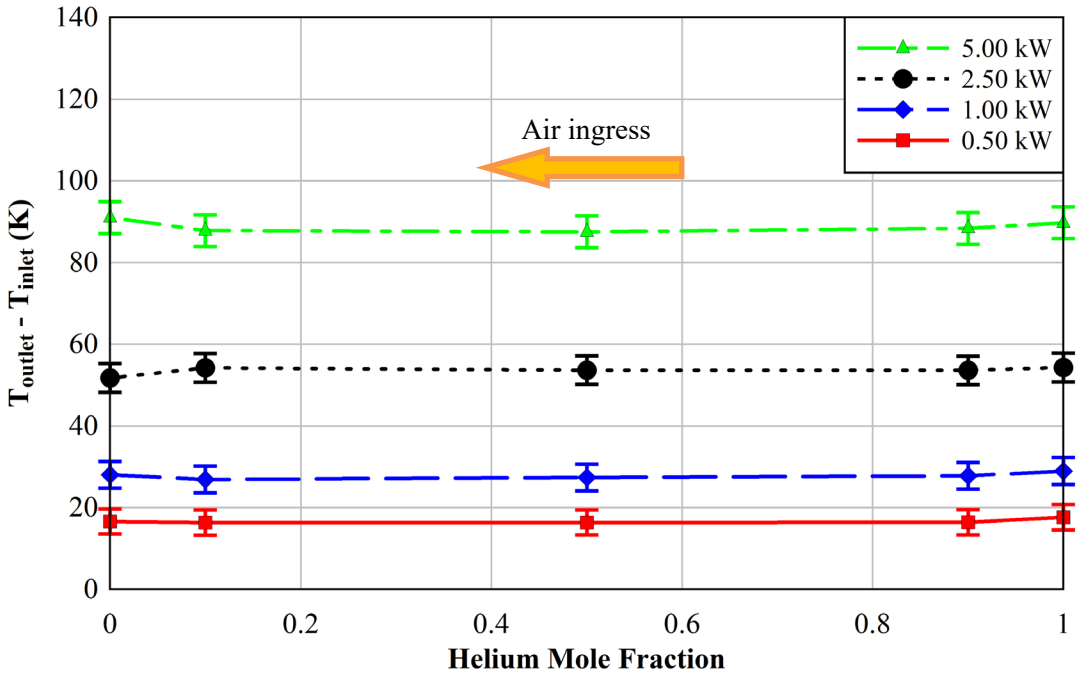

Figure 3.24 Inlet/outlet duct temperature difference versus helium mole fraction.

This page is intentionally left blank.

4 SUMMARY

The investigation described in this report documents data sets from the horizontal dry cask simulator that can be used to benchmark the codes and best practices presently used to determine cladding temperatures and induced cooling air flows in modern horizontal dry storage systems. These new data setsare from tests using helium/air blends as representative canister backfill gases. These data sets complement the existing database by simulating various stages of loss of helium backfill from a horizontal storage module and quantifying the resulting thermal response and induced air flow.

The HDCS has been designed to generate this benchmark data and add to the existing knowledge base. The pressure vessel representing the canister has been designed, fabricated, and pressure tested for a MAWP rating of 2,400 kPa at 400 °C. An existing electrically heated and Incoloy-clad but otherwise prototypic BWR test assembly has been deployed inside of a representative storage basket and canister. An insulated sheet metal enclosure is used to mimic the thermal properties of the concrete vault enclosure used in a modern horizontal storage system. Transverse and axial temperature profiles along with induced cooling air flow are measured for a wide range of decay heat powers and representative (and higher) canister pressures using helium, air, and helium/air blends as backfills.

The single assembly geometry with well-controlled boundary conditions simplifies computational requirements while preserving relevant physics. The test apparatus integrates all the underlying thermal-hydraulics important to defining the performance of a modern horizontal storage system. These include combined-mode heat transfer from the electrically-heated assembly to the canister walls and the primarily natural-convective heat transfer from the canister to the cooling air flow passing through the horizontal vault enclosure.

The HDCS update report [Lindgren *et al*. 2019] presented data from two of the ten previously run HDCS test cases using helium and air backfill gases, while the HDCS model validation report [Pulido *et al*., 2020b] presented data from the other eight test cases as well as comparisons of this data to modeling results. The uniqueness of the present investigation is found in the new data presented in this report that focuses on the use of helium/air blend backfill gases in the HDCS. These blends simulate various stages of the loss of helium backfill from a horizontal dry cask storage system, and the measurements taken capture the thermal-hydraulic effects of the concentration of helium versus air in a horizontally-oriented dry storage canister.

A total of twenty tests were conducted where the HDCS achieved steady state for various assembly powers and helium/air backfill gas compositions. The axial, vertical, and horizontal temperature profiles presented in this report showed that helium mole concentration primarily affects the temperatures within the fuel assembly, with decreasing helium mole concentration and subsequent increasing air mole concentration resulting in higher fuel assembly temperatures. The temperature differences between tests of varying helium/air concentrations for a given power dropped off as the transverse temperature profiles approached the outlying structures, and the temperatures at the canister and the vault were largely similar across all tests for a given power.

The effects of a loss of helium backfill from a horizontal storage canister were also recorded by examining other system responses. These included comparisons of PCT, total air mass flow rate, canister/ambient temperature delta, and vault inlet/outlet temperature data versus helium concentration. A comprehensive uncertainty analysis was part of this analysis. The total air mass flow rate and the canister surface-to-ambient temperature differences were independent of helium concentration. Relative helium/air concentrations for a given power within a canister were observed to primarily affect the temperatures in the assembly, including the peak cladding temperature. Decreasing helium concentration, which represents a loss of helium backfill, led to higher fuel assembly temperatures in the HDCS. This implies that these fuel temperature increases from a loss of helium backfill would be similarly observed in the fuel inside a commercial horizontal dry storage canister.

This page is intentionally left blank.

REFERENCES

American National Standards Institute, "American National Standard for Radioactive Materials – Leakage Tests on Packages for Shipment," ANSI N14.5-2014, New York, NY, June 2014.

ASTM International, "Standard Specification for Temperature-Electromotive Force (emf) Tables for Standardized Thermocouples," E230/E230M-17, West Conshohocken, PA, November 2017.

Bates, J.M., "Single PWR Spent Fuel Assembly Heat Transfer Data for Computer Code Evaluations," PNL-5571, Pacific Northwest Laboratory, Richland, WA, January 1986.

Canaan, R.E. and D.E. Klein, "An Experimental Investigation of Natural Convection Heat Transfer Within Horizontal Spent-Fuel Assemblies," Nuclear Technology, 116:3, 306-318, July 1996.

Creer, J.M., T.E. Michener, M.A. McKinnon, J.E. Tanner, E.R. Gilbert, R.L. Goodman, "The TN-24P PWR Spent Fuel Storage Cask: Testing and Analyses", EPRI NP-5128 Proj. 2406-4, PNL-6054, Electric Power Research Institute, Palo Alto, CA, April 1987.

Durbin, S.G. and E.R. Lindgren, "Thermal-Hydraulic Experiments Using a Dry Cask Simulator," NUREG/CR-7250, Nuclear Regulatory Commission, Washington, D.C., October 2018.

Dziadosz, D., E.V. Moore, J.M. Creer, R.A. McCann, M.A. McKinnon, J.E. Tanner, E.R. Gilbert, R.L. Goodman, D.H. Schoonen, M Jensen, and C. Mullen, "The Castor-V/21 PWR Spent-Fuel Storage Cask: Testing and Analyses," EPRI NP-4887, Project 2406-4, PNL-5917, UC-85, Electric Power Research Institute, Palo Alto, CA, November 1986.

Hanson, B., H. Alsaed, C. Stockman, D. Enos, R. Meyer, and K. Sorenson, "Gap Analysis to Support Extended Storage of Used Nuclear Fuel Rev. 0," FCRD-USED-2011-000136 Rev. 0, PNNL-20509, Pacific Northwest National Laboratory, Richland, WA, January 2012.

Huber, M.L. and A.H. Harvey, "Thermal Conductivity of Gases," CRC Handbook of Chemistry and Physics, 92nd Ed., Boca Raton, FL, June 2011.

Ifan, H. and T. Hughes, Measurements And Their Uncertainties: A Practical Guide To Modern Error Analysis, Oxford University Press, 1st Ed., October 2010.

Irino, M., M. Oohashi, T. Irie, and T. Nishikawa, "Study on Surface Temperatures of Fuel Pins in Spent Fuel Dry Shipping/Storage Casks," IAEA-SM-286/139P, Proceedings of Packaging and Transportation of Radioactive Materials (PATRAM '86), Volume 2, p. 585, International Atomic Energy Agency, Vienna, Austria, 1987.

Lindgren, E.R. and S.G. Durbin, "Characterization of Thermal-Hydraulic and Ignition Phenomena in Prototypic, Full-Length Boiling Water Reactor Spent Fuel Pool Assemblies after a Complete Loss-of-Coolant Accident", NUREG/CR-7143, SAND2007-2270, Nuclear Regulatory Commission, Washington, D.C., March 2013.

Lindgren, E.R. and S.G. Durbin, "Materials and Dimensional Reference Handbook for the Boiling Water Reactor Dry Cask Simulator," SAND2017-13058R, Sandia National Laboratories, Albuquerque, NM, November 2017.

Lindgren, E.R., S.G. Durbin, R.J.M. Pulido, and A. Salazar, "Update on the Thermal Hydraulic Investigations of a Horizontal Dry Cask Simulator," SAND2019-11688R, Sandia National Laboratories, Albuquerque, NM, September 2019.

McKinnon, M.A., J.W. Doman, J.E. Tanner, R.J. Guenther, J.M. Creer and C.E. King, "BWR Spent Fuel Storage Cask Performance Test, Volume 1, Cask Handling Experience and Decay Heat, Heat Transfer, and Shielding Data," PNL-5777 Vol. 1, Pacific Northwest Laboratory, Richland, WA, February 1986.

McKinnon, M.A., J.M. Creer, C. L. Wheeler, J.E. Tanner, E.R. Gilbert, R.L. Goodman, D.P. Batala, D.A. Dziadosz, E.V. Moore, D.H. Schoonen, M.F. Jensen, and J.H. Browder, "The MC-10 PWR Spent Fuel Storage Cask: Testing and Analysis," EPRI NP-5268, Electric Power Research Institute, Palo Alto, CA, July 1987.

McKinnon, M.A., T.E. Michener, M.F. Jensen, G.R. Rodman, "Testing and Analyses of the TN-24P Spent Fuel Dry Storage Cask Loaded with Consolidated Fuel," EPRI NP-6191 Proj. 2813-16, PNL-6631, February 1989.

Misumi, T., Suzuki, K., and Kitamura, K., "Fluid Flow and Heat Transfer of Natural Convection Around Large Horizontal Cylinders: Experiments with Air," Heat Trans. – Asian Res., 32 (4), 293-305, 2003.

Nakos, J.T., "Uncertainty Analysis of Thermocouple Measurements Used in Normal and Abnormal Thermal Environment Experiments at Sandia's Radiant Heat Facility and Lurance Canyon Burn Site," SAND2004-1023, Sandia National Laboratories, Albuquerque, NM, April 2004.

Noack, B.R., "On the Flow Around a Circular Cylinder. Part II: Turbulent Regime,", ZAMM-Z. Angew. Math. Me., 79, S227-S230, 1999.

Pulido, R.J.M., E.R. Lindgren, S.G. Durbin, A. Zigh, J. Solis, S.R. Suffield, D.J. Richmond, J.A. Fort, L.E. Herranz, F. Feria, J. Penalva, M. LLoret, M. Galbán, J. Benavides, and G. Jiménez, "Modeling Validation Exercises Using the Dry Cask Simulator," SAND2019-6079R, Sandia National Laboratories, Albuquerque, NM, January 2020 (2020a).

Pulido, R.J.M., R.E. Fasano, E.R. Lindgren, G.J. Koenig, S.G. Durbin, A. Zigh, J. Solis, K. Hall, S.R. Suffield, D.J. Richmond, J.A. Fort, M. LLoret, M. Galbán, A. Sabater, "Blind Modeling Validation Exercises Using the Horizontal Dry Cask Simulator," SAND2020-10344R, Sandia National Laboratories, Albuquerque, NM, September 2020 (2020b).

Saltzstein, S., G.A. Freeze, B. Hanson, and K. Sorenson, "Spent Fuel and Waste Science and Technology Storage and Transportation 5-Year R&D Plan," SAND2020-9310R, Sandia National Laboratories, Albuquerque, NM, September 2020.

Schindelholz, E., C. Bryan, and C. Alexander, "FY17 Status Report: Research on Stress Corrosion Cracking of SNF Interim Storage Canisters," SAND2017-10338R, Sandia National Laboratories, Albuquerque, NM, August 2017.

Solis, J. and Zigh, A., "Impact of Variation in Environmental Conditions on the Thermal Performance of Dry Storage Casks," NUREG-2174, Nuclear Regulatory Commission, Washington, D.C., February 2015.

Sparrow, E.M. and Pfeil, D.R., "Enhancement of Natural Convection Heat Transfer from a Horizontal Cylinder Due to Vertical Shrouding Surfaces," J. Heat Trans., 106, 124-130, February 1984.

Strope, L.A., M.A. McKinnon, D.J. Dyksterhouse, and J.C. McLean, "NUHOMS Modular Spent-Fuel Storage System: Performance Testing," EPRI NP-6941, PNL-7327, Electric Power Research Institute, Palo Alto, CA, September 1990.

Taylor, J.R., An Introduction to Error Analysis: The Study of Uncertainties in Physical Measurements, University Science Books, 2nd Ed., August 1996.

Yamamoto, A., Ikehara, T., and Ito, T. "Benchmark Problem Suite for Reactor Physics Study of LWR Next Generation Fuels," J. Nucl. Sci. Tech., 39 (8), 900-912, 2002.

APPENDIX A ERROR PROPAGATION ANALYSIS

The error and uncertainty inherent to an experimental result are critical to the accurate interpretation of the data. Therefore, the uncertainties in the experimental measurements are estimated in this section. Results of this analysis are given, followed by a general description of the method used and a brief explanation of the source of each reported measurement uncertainty.

The overall standard uncertainty of an indirect measurement y, dependent on N indirect measurements x_i, is defined in Equation A.1. The standard uncertainty associated with an indirect measurement is analogous to the standard deviation of a statistical population.

$$u^2 = \sum_{i=1}^{N} \left(\frac{\partial y}{\partial x_i} u_i \right)^2 \quad \text{A.1}$$

Here, u is used to define the standard uncertainty of a measurement [Taylor, 1996; Ifan and Hughes, 2010].

The expanded uncertainty, U, is reported in this Appendix and defines the bounds that include 95% of the possible data. The expanded uncertainty is assumed to be defined as the product of the standard uncertainty and the Student's t-value. Unless otherwise stated, all uncertainty measurements are assumed to be based on a Student's t-distribution with no fewer than 30 measurements. Considering that the HDCS DAQ collects data at least every 5 seconds over the steady-state period, which lasts at least 6 hours for any given test, the steady-state period contains at least 4320 data points for all comparison metrics, so this assumption is valid. The associated t-value for 95% confidence intervals is 2.0 for 29 degrees of freedom. Therefore, Equation A.2 shows the definition of the expanded uncertainty as used in the following sections for a 95% confidence interval.

$$U = t_{\text{value}} \cdot u \quad \text{A.2}$$

A.1 Temperature Measurements

A.1.1 Uncertainty in Clad Temperature Measurement

Clad temperature was measured with a standard type-K TC using the standard ASTM calibration specifications [ASTM, 2017]. No additional calibrations were performed. While uncertainties of up to 2 to 5% are justified for surface-mounted thermocouples in high heat flux and/or highly transient environments, the relatively small spatial and temporal gradients experienced during the HDCS testing warrant an expanded uncertainty for this type of TC of U_T = 1% of the reading in Kelvin [Nakos, 2004]. In this case, the expanded uncertainty was 1% of the maximum temperature reading from each test (the peak cladding temperature). Table A.1 shows the experimental uncertainties in the cladding temperatures, Table A.2 shows the experimental uncertainties in the canister temperatures, and Table A.3 shows the uncertainties in the outlet duct temperatures from the test cases considered in this report. These experimental uncertainties applied to the peak cladding temperature as well as the axial, vertical, and horizontal temperature profiles. Note the symmetry in the upper and lower uncertainty bounds since the calculation of 1% of the maximum temperature contains no uncertainty bias in either direction.

Table A.1 Peak cladding temperature experimental uncertainties.

Conditions		Upper Uncertainty Bound (K)	Lower Uncertainty Bound (K)
Power (kW)	Mole Fraction He, Balance Air		
0.5	1.0 He	3.7	3.7
1.0	1.0 He	4.3	4.3
2.5	1.0 He	5.6	5.6
5.0	1.0 He	6.9	6.9
0.5	0.9 He	3.8	3.8
1.0	0.9 He	4.3	4.3
2.5	0.9 He	5.6	5.6
5.0	0.9 He	7.0	7.0
0.5	0.5 He	3.9	3.9
1.0	0.5 He	4.6	4.6
2.5	0.5 He	6.0	6.0
5.0	0.5 He	7.3	7.3
0.5	0.1 He	4.1	4.1
1.0	0.1 He	4.9	4.9
2.5	0.1 He	6.2	6.2
5.0	0.1 He	7.6	7.6
0.5	0.0 He	4.3	4.3
1.0	0.0 He	5.0	5.0
2.5	0.0 He	6.5	6.5
5.0	0.0 He	7.8	7.8

Table A.2 Canister surface temperature experimental uncertainties.

Conditions		Upper Uncertainty Bound (K)	Lower Uncertainty Bound (K)
Power (kW)	Mole Fraction He, Balance Air		
0.5	1.0 He	3.3	3.3
1.0	1.0 He	3.6	3.6
2.5	1.0 He	4.2	4.2
5.0	1.0 He	4.9	4.9
0.5	0.9 He	3.3	3.3
1.0	0.9 He	3.6	3.6
2.5	0.9 He	4.1	4.1
5.0	0.9 He	4.9	4.9
0.5	0.5 He	3.3	3.3
1.0	0.5 He	3.5	3.5
2.5	0.5 He	4.1	4.1
5.0	0.5 He	4.9	4.9
0.5	0.1 He	3.3	3.3
1.0	0.1 He	3.5	3.5
2.5	0.1 He	4.2	4.2
5.0	0.1 He	4.9	4.9
0.5	0.0 He	3.3	3.3
1.0	0.0 He	3.6	3.6
2.5	0.0 He	4.2	4.2
5.0	0.0 He	5.0	5.0

Table A.3 Outlet duct temperature experimental uncertainties.

Conditions		Upper Uncertainty Bound (K)	Lower Uncertainty Bound (K)
Power (kW)	Mole Fraction He, Balance Air		
0.5	1.0 He	3.1	3.1
1.0	1.0 He	3.3	3.3
2.5	1.0 He	3.5	3.5
5.0	1.0 He	3.9	3.9
0.5	0.9 He	3.1	3.1
1.0	0.9 He	3.3	3.3
2.5	0.9 He	3.5	3.5
5.0	0.9 He	3.9	3.9
0.5	0.5 He	3.1	3.1
1.0	0.5 He	3.2	3.2
2.5	0.5 He	3.5	3.5
5.0	0.5 He	3.9	3.9
0.5	0.1 He	3.1	3.1
1.0	0.1 He	3.2	3.2
2.5	0.1 He	3.5	3.5
5.0	0.1 He	3.9	3.9
0.5	0.0 He	3.1	3.1
1.0	0.0 He	3.3	3.3
2.5	0.0 He	3.5	3.5
5.0	0.0 He	3.9	3.9

A.1.2 Uncertainty in Ambient Air Temperature

The air temperature was measured with a standard type-K TC. The expanded uncertainty for this type of TC is U_T = 1% of the reading in Kelvin [Nakos, 2004]. The maximum ambient temperature reading among the tests considered in this report was 305 K for the 5.0 kW 100 kPa air test. The maximum expanded uncertainty for the ambient temperature is $U_{T\text{-}amb}$ = ±3.1 K.

A.2 Pressure Measurements

A.2.1 Uncertainty in Ambient Air Pressure

The air pressure was measured with an Omega pressure sensor (Model PX2760-600A5V, S/N 6857389). The uncertainty of the ambient air pressure was taken from the manufacturer's calibration sheet, which indicated an expanded uncertainty in the instrument of ±0.25% of full scale (110 kPa). Therefore, the expanded uncertainty in the pressure reading is $U_{P\text{-}atm}$ = ±0.275 kPa.

A.2.2 Uncertainty in Vessel Pressure

The interior vessel pressure was measured as the average output of two high-accuracy 0 to 1,034 kPa (0 to 150 psia) absolute pressure transducers (Setra Systems ASM1-150P-A-1M-2C-03-A-01) installed in the instrument well. The experimental uncertainty associated with a single gage is ±0.05% of full scale, or $U_{PV,1}$ = ±0.52 kPa (±0.075 psi). The combined uncertainty of the average of the two transducers is $U_{PV, AVG}$ = ±0.37 kPa (±0.053 psia). Note that the pressure was controlled to within ±0.35 kPa (±0.051 psia) as measured by taking half of the difference between the overall maximum and minimum internal average pressure observed during testing.

A.3 Uncertainty in Electrical Measurements

The voltage, current, and power supplied to the internal spent fuel assembly heater rods were measured by an Ohio Semitronics, Inc. Multifunction Power Test Board (Model PTB-112D1PCY48, SN 18100713). The stated manufacturer's uncertainty was given as ±0.25% of full scale for each measurement. The full scales for each measurement are as follows: Voltage = 150 V, Amps = 100 A, Power Factor = 1.00, and Power = 12.00 kW. However, a special calibration schedule of thirty-two points was ordered for this instrument. The expanded uncertainty based on the *t*-statistic (t_{31} = 2.0) and the standard error of the regression for each measurement variable was as follows: U_{Volt} = ±0.11 V, U_{Amp} = ±0.07 A, U_{PF} = ±0.036, U_{Watt} = ±13 W. These instrument-specific uncertainties represent considerably better accuracy than the generic manufacturer's certification.

A.4 Flow Measurements

The methodology for determining the induced air flow is described in detail in Section 2.5.2. Air velocity profiles were recorded across the inlet ducts. These velocities were then used to derive the two-dimensional flow field in the ducts. This flow field was then integrated to determine the air mass flow rate.

The uncertainty in the air mass flow rate per duct was calculated to be $U_{\dot{m}, \text{per duct}} = \pm 1.5 \times 10^{-4}$ kg/s. The combined error in the total air mass flow rate across all four ducts is $U_{\dot{m}, \text{Total}} = \pm 3.0 \times 10^{-4}$ kg/s. Note that 90% of this error is associated with uncertainties in the differential areas and integration scheme. The remaining error is due to uncertainty in the hot wire anemometers. Finally, the observed fluctuation in the air mass flow rate per duct, given by $(\dot{m}_{max} - \dot{m}_{min})/2 = 1.7 \times 10^{-4}$ kg/s, was roughly in agreement with the estimated uncertainty.

The instrument uncertainty, together with the observed fluctuation in the steady-state flow (calculated as the 95% confidence interval of the flow measurements during the test steady-state period), were used to calculate a combined measurement uncertainty for the air mass flow rate. Table A.4 shows the results of these calculations for the ten test cases. Note the symmetry in the upper and lower uncertainty bounds since the calculation of the combined measurement uncertainty contains no uncertainty bias in either direction.

Table A.4 Air mass flow rate experimental uncertainties.

Conditions		Upper Uncertainty Bound (K)	Lower Uncertainty Bound (K)
Power (kW)	Mole Fraction He, Balance Air		
0.5	1.0 He	0.0004	0.0004
1.0	1.0 He	0.0006	0.0006
2.5	1.0 He	0.0004	0.0004
5.0	1.0 He	0.0006	0.0006
0.5	0.9 He	0.0008	0.0008
1.0	0.9 He	0.0006	0.0006
2.5	0.9 He	0.0007	0.0007
5.0	0.9 He	0.0008	0.0008
0.5	0.5 He	0.0010	0.0010
1.0	0.5 He	0.0008	0.0008
2.5	0.5 He	0.0005	0.0005
5.0	0.5 He	0.0005	0.0005
0.5	0.1 He	0.0009	0.0009
1.0	0.1 He	0.0007	0.0007
2.5	0.1 He	0.0006	0.0006
5.0	0.1 He	0.0005	0.0005
0.5	0.0 He	0.0006	0.0006
1.0	0.0 He	0.0007	0.0007
2.5	0.0 He	0.0004	0.0004
5.0	0.0 He	0.0005	0.0005

A.4.1 Uncertainty in Hot Wire Anemometer Measurements

The TSI Model 8455 hot wire anemometer has a manufacturer's expanded uncertainty of ±2% of reading +0.5% of full scale. The chosen full scale for all tests was 1 m/s. Therefore, the maximum expanded uncertainty was defined as $U_v = \pm 0.025$ m/s for the ambient temperatures encountered. Standard conditions for the TSI hotwire are 21.1 °C and 101.4 kPa.

For velocities near the wall, an alternative approach was adopted to estimate uncertainty. The difference in the velocity central to the differential area and the average of the estimated velocities along the periphery of the differential area was taken to estimate the maximum uncertainty. The average of this alternative uncertainties along the perimeter of the inlet gives an expanded uncertainty of $U_{v,\nabla v} = \pm 0.033$ m/s for these edge velocities.

A.4.2 Uncertainty in Differential Areas

The positional accuracy of each motorized stage (Velmex Xslide) based on straight line accuracy is given by the manufacturer as $U_{stage} = \pm 0.08$ mm. However, this estimate does not include other sources of uncertainty such as slight errors in stage alignment and deviations in the duct itself. An uncertainty for each dimension of the differential area of $U_{\Delta x} = U_{\Delta y} = \pm 1.6$ mm was chosen to incorporate all known and unknown uncertainties in the differential area.

Table A.1 gives the uncertainty of the average differential area $U_{\Delta A,AVG} = \pm 2.3 \times 10^{-5}$ m^2.

Table A.5 Representative calculation to estimate the expanded error of flow area determination.

Measurement, x_i	Units	Value	Expanded uncertainty, U_i	Influence coefficient ($U_i \cdot [(\partial \Delta A/\partial x_i)/\Delta A]$)	Contribution
Δx_{AVG}	m	6.4E-03	1.6E-03	2.5E-01	0.81
Δy_{AVG}	m	1.3E-02	1.6E-03	1.2E-01	0.19
ΔA_{AVG}	m^2	8.3E-05	2.3E-05	2.8E-01	1.00

This page is intentionally left blank.

APPENDIX B LIST OF INSTRUMENTATION EXTERNAL TO THE PRESSURE VESSEL

B.1 Conventions

A right-hand coordinate system is employed based on an origin defined by the top of the bottom tie plate in the assembly (see Figure 2.10). Based on the orientation of the assembly within the facility, x points downward, y points northward, and z points eastward. Maintaining terminology from previous vertically-oriented tests, the z-component increases from the "bottom" to the "top" of the structure.

A labeling system is devised for instrumentation that identifies the abbreviated name of the adjoining vault component, the cardinal direction, and the cartesian coordinates. For example, on the vault side panel, "SP_S_10.808_-6.5_108" denotes a thermocouple on the side panel facing south 10.808 inches towards the baseplate, 6.5 inches south, and 108 inches east from the origin.

B.2 Thermocouples

B.2.1 Vault Thermocouples

The vault thermocouples are listed in Table B.1 and diagrammed in Figure B.1 through Figure B.3. Those that are installed on the inside of the vault (i.e. facing the pressure vessel) are indicated.

Table B.1 List of thermocouples on the vault top and side panels.

#	Face	Dir.	Label	x (in.)	y (in.)	z (in.)	Type
231	E	W	TP_W_-6.661_0_0	-6.661	0	0	TC (Type-K)
232	E	W	TP_W_-6.661_0_12	-6.661	0	12	TC (Type-K)
233	E	W	TP_W_-6.661_0_24	-6.661	0	24	TC (Type-K)
234	E	W	TP_W_-6.661_0_36	-6.661	0	36	TC (Type-K)
235	E	W	TP_W_-6.661_0_48	-6.661	0	48	TC (Type-K)
236	E	W	TP_W_-6.661_0_60	-6.661	0	60	TC (Type-K)
237	E	W	TP_W_-6.661_0_72	-6.661	0	72	TC (Type-K)
238	E	E	TP_E_-6.661_0_84	-6.661	0	84	TC (Type-K)
239	I	E	TP_INT_E_-6.536_0_84	-6.536	0	84	TC (Type-K)
240	E	E	TP_E_-6.661_0_96	-6.661	0	96	TC (Type-K)
241	E	E	TP_E_-6.661_0_108	-6.661	0	108	TC (Type-K)
242	E	E	TP_E_-6.661_0_120	-6.661	0	120	TC (Type-K)
243	E	E	TP_E_-6.661_0_132	-6.661	0	132	TC (Type-K)
244	E	E	TP_E_-6.661_0_144	-6.661	0	144	TC (Type-K)
245	E	E	TP_E_-6.661_0_156	-6.661	0	156	TC (Type-K)
246	E	SW	RIB_SW_5.027_-6.5_0	5.0	-6.5	0	TC (Type-K)
247	E	S	SP_S_10.808_-6.5_24	10.8	-6.5	24	TC (Type-K)
248	E	S	SP_S_-0.755_-6.5_24	-0.8	-6.5	24	TC (Type-K)
249	E	S	SP_S_5.027_-6.5_48	5.0	-6.5	48	TC (Type-K)
250	E	S	SP_S_10.808_-6.5_71	10.8	-6.5	71*	TC (Type-K)
251	E	S	SP_S_-0.755_-6.5_71	-0.8	-6.5	71*	TC (Type-K)
252	E	S	RIB_S_5.027_-6.5_84	5.0	-6.5	84	TC (Type-K)
253	I	S	RIB_INT_S_5.027_-6.375_84	5.0	-6.375	84	TC (Type-K)

#	Face	Dir.	Label	*x* (in.)	*y* (in.)	*z* (in.)	Type
254	E	S	SP_S_10.808_-6.5_108	10.8	-6.5	108	TC (Type-K)
255	E	S	SP_S_-0.755_-6.5_108	-0.8	-6.5	108	TC (Type-K)
256	E	S	SP_S_5.027_-6.5_132	5.0	-6.5	132	TC (Type-K)
257	E	SE	RIB_SE_10.808_-6.5_156	10.8	-6.5	156	TC (Type-K)
258	E	SE	RIB_SE_-0.755_-6.5_156	-0.8	-6.5	156	TC (Type-K)
259	E	NW	RIB_NW_10.808_6.5_0	10.8	6.5	0	TC (Type-K)
260	E	NW	RIB_NW_-0.755_6.5_0	-0.8	6.5	0	TC (Type-K)
261	E	N	SP_N_5.027_6.5_24	5.0	6.5	24	TC (Type-K)
262	E	N	SP_N_10.808_6.5_48	10.8	6.5	48	TC (Type-K)
263	E	N	SP_N_-0.755_6.5_48	-0.8	6.5	48	TC (Type-K)
264	E	N	SP_N_5.027_6.5_71	5.0	6.5	71*	TC (Type-K)
265	E	N	RIB_N_10.808_6.5_84	10.8	6.5	84	TC (Type-K)
266	E	N	RIB_N_-0.755_6.5_84	-0.8	6.5	84	TC (Type-K)
267	I	N	RIB_INT_N_-0.755_6.375_84	-0.8	6.375	84	TC (Type-K)
268	E	N	SP_N_5.027_6.5_108	5.0	6.5	108	TC (Type-K)
269	E	N	SP_N_10.808_6.5_132	10.8	6.5	132	TC (Type-K)
270	E	N	SP_N_-0.755_6.5_132	-0.8	6.5	132	TC (Type-K)
271	E	NE	RIB_NE_5.027_6.5_156	5.0	6.5	156	TC (Type-K)

TP=top panel, SP=side panel, INT=interior face, E=External, I=Internal
*as-built dimension

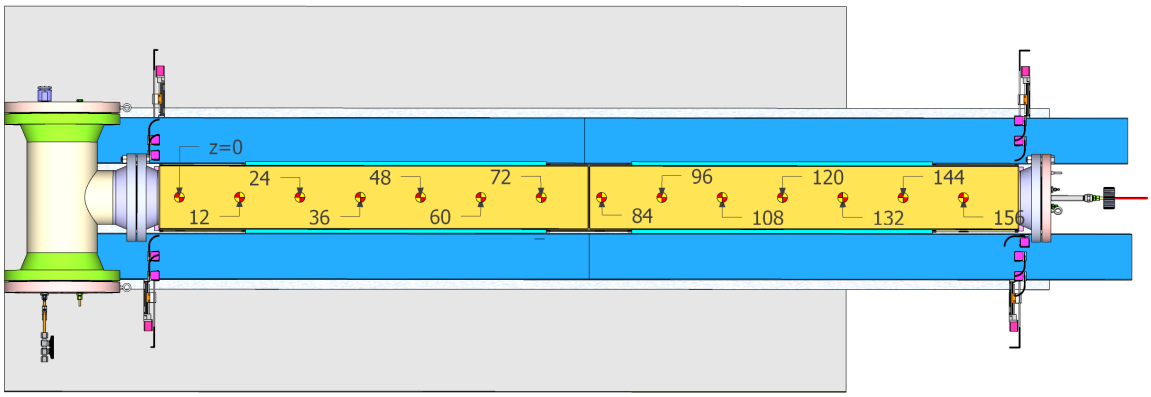

All dimensions are in inches

Figure B.1 View of top panel TCs.

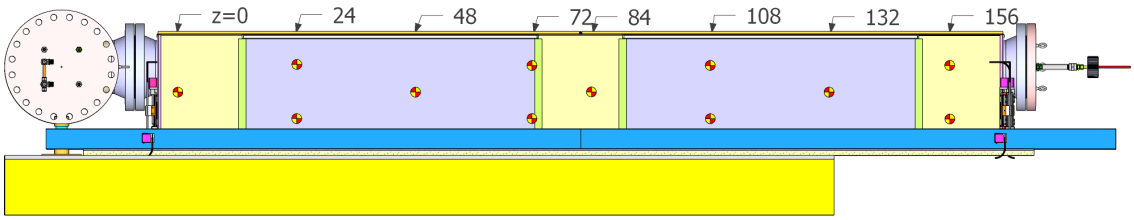

All dimensions are in inches

Figure B.2 View of southern side panel TCs.

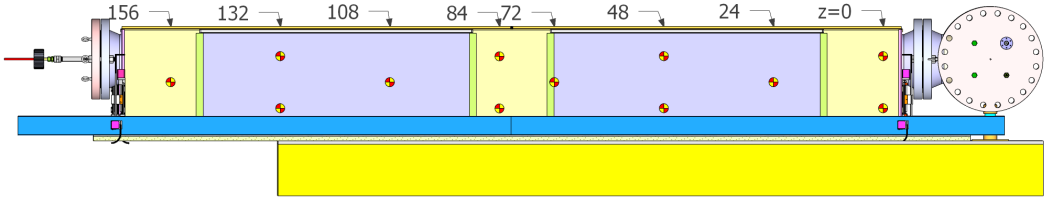

All dimensions are in inches

Figure B.3 View of northern side panel TCs.

B.2.2 Baseplate, Endplate, and Internal Thermocouples

The baseplate and endplate thermocouples are listed in Table B.2; these TCs are diagrammed in Figure B.4 and Figure B.5. The inlet and outlet thermocouples are listed in Table B.3. The system and ambient thermocouples that comprise the internal thermocouples are listed in Table B.4.

Table B.2 List of thermocouples on the baseplate and vault endplate, as well as gas TCs around the baseplate, pressure vessel, and vault.

#	Face	Dir.	Label	*x* (in.)	*y* (in.)	*z* (in.)	Type
272	I	-	BP_TOP_16.589_0_0	16.5890	0	0	TC (Type-K)
273	I	-	g_BP_PV_10.982_0_0	10.9820	0	0	Gas-TC
274	I	-	g_PV_V_-5.973_0_0	-5.9725	0	0	Gas-TC
275	I	-	BP_TOP_16.589_0_24	16.5890	0	24	TC (Type-K)
276	I	-	BP_TOP_16.589_0_48	16.5890	0	48	TC (Type-K)
277	I	-	g_BP_PV_10.982_0_48	10.9820	0	48	Gas-TC
278	I	-	g_PV_V_-5.973_0_48	-5.9725	0	48	Gas-TC
279	I	-	BP_TOP_16.589_0_72	16.5890	0	72	TC (Type-K)
280	I	-	g_BP_PV_10.982_0_72	10.9820	0	72	Gas-TC
281	I	-	g_PV_V_-5.973_0_72	-5.9725	0	72	Gas-TC
282	I	-	BP_TOP_16.589_0_96	16.5890	0	96	TC (Type-K)
283	I	-	BP_TOP_16.589_0_120	16.5890	0	120	TC (Type-K)
284	I	-	g_BP_PV_10.982_0_120	10.9820	0	120	Gas-TC
285	I	-	g_PV_V_-5.973_0_120	-5.9725	0	120	Gas-TC
286	I	-	BP_TOP_16.589_0_144	16.5890	0	144	TC (Type-K)

#	Face	Dir.	Label	*x* (in.)	*y* (in.)	*z* (in.)	Type
287	I	-	BP_TOP_16.589_0_156	16.5890	0	156	TC (Type-K)
288	I	-	g_BP_PV_10.982_0_156	10.9820	0	156	Gas-TC
289	I	-	g_PV_V_-5.973_0_156	-5.9725	0	156	Gas-TC
290	E	SW	EP_SW_11.17_-3.31_-4.644	11.170	-3.313	-4.6	TC (Type-K)
291	E	NW	EP_NW_11.17_3.31_-4.644	11.170	3.313	-4.6	TC (Type-K)
292	E	SE	EP_SE_11.17_-3.31_166.816	11.170	-3.313	166.8	TC (Type-K)
293	E	NE	EP_NE_11.17_3.31_166.816	11.170	3.313	166.8	TC (Type-K)
334	E	-	BP_BOT_16.839_0_156	16.839	0	156.0	TC (Type-K)

BP=base plate, PV=pressure vessel, V=vault, EP=end plate, g=gas, E=External, I=Internal, BOT=bottom

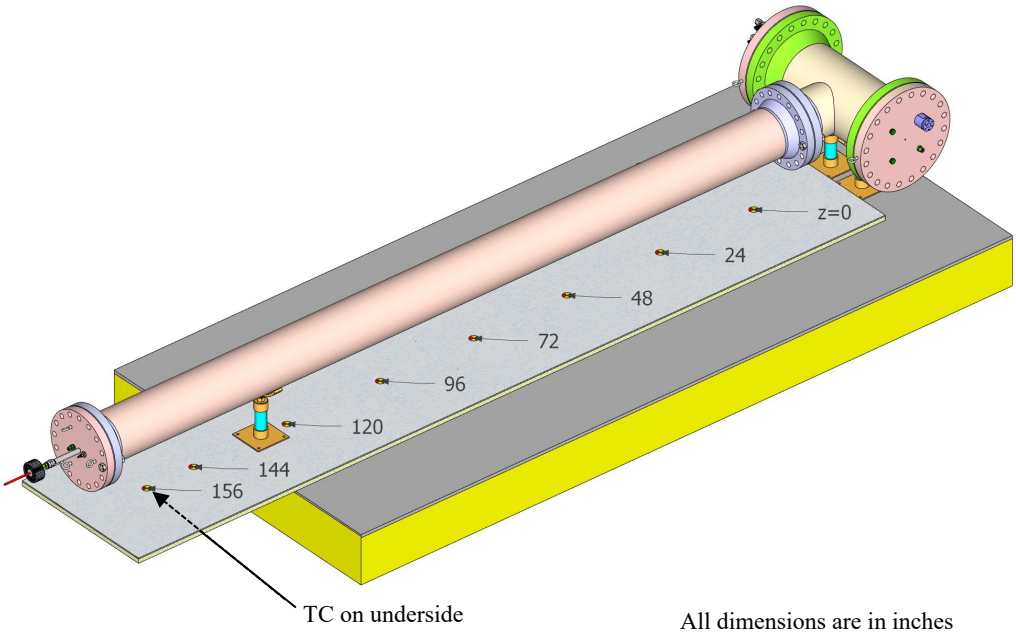

Figure B.4 Baseplate TCs.

Figure B.5 Location of TCs on left and right endplates.

B.2.3 Inlet and Outlet Thermocouples

Table B.3 List of thermocouples on the vault inlets and outlets.

#	Face	Dir.	Label	*x* (in.)	*y* (in.)	*z* (in.)	Type
296	I	NW	g_INL_NW_14.511_11.7_-24.3	14.511	11.7	-24.3	Gas-TC
297	I	NW	g_INL_NW_14.511_11.7_48	14.511	11.7	48	Gas-TC
298	I	SW	g_INL_SW_14.511_-11.7_-24.3	14.511	-11.7	-24.3	Gas-TC
299	I	SW	g_INL_SW_14.511_-11.7_48	14.511	-11.7	48	Gas-TC
300	I	NE	g_INL_NE_14.511_11.7_120	14.511	11.7	120	Gas-TC

#	Face	Dir.	Label	*x* (in.)	*y* (in.)	*z* (in.)	Type
301	I	NE	g_INL_NE_14.511_11.7_186.4	14.511	11.7	186.4	Gas-TC
302	I	SE	g_INL_SE_14.511_-11.7_120	14.511	-11.7	120	Gas-TC
303	I	SE	g_INL_SE_14.511_-11.7_186.4	14.511	-11.7	186.4	Gas-TC
304	I	NW	g_OUT_NW_-6.202_6.5_36	-6.202	6.5	36	Gas-TC
305	I	NW	g_OUT_NW_-6.202_6.5_48	-6.202	6.5	48	Gas-TC
306	I	NW	g_OUT_NW_-6.202_6.5_60	-6.202	6.5	60	Gas-TC
307	I	SW	g_OUT_SW_-6.202_-6.5_24	-6.202	-6.5	24	Gas-TC
308	I	SW	g_OUT_SW_-6.202_-6.5_48	-6.202	-6.5	48	Gas-TC
309	I	SW	g_OUT_SW_-6.202_-6.5_72	-6.202	-6.5	72	Gas-TC
310	I	NE	g_OUT_NE_-6.202_6.5_108	-6.202	6.5	108	Gas-TC
311	I	NE	g_OUT_NE_-6.202_6.5_120	-6.202	6.5	120	Gas-TC
312	I	NE	g_OUT_NE_-6.202_6.5_132	-6.202	6.5	132	Gas-TC
313	I	SE	g_OUT_SE_-6.202_-6.5_96	-6.202	-6.5	96	Gas-TC
314	I	SE	g_OUT_SE_-6.202_-6.5_120	-6.202	-6.5	120	Gas-TC
315	I	SE	g_OUT_SE_-6.202_-6.5_145	-6.202	-6.5	145*	Gas-TC

INL=inlet, OUT=outlet, g=gas, E=External, I=Internal
*as-built dimension

B.2.4 System and Ambient Thermocouples

Table B.4 List of thermocouples measuring ambient and system temperatures.

#	Face	Dir.	Label	*x* (in.)	*y* (in.)	*z* (in.)	Type
294	E	E	Mid_Top_Flange_E_-1_0_173.9	-1.0	0	173.9	TC (Type-K)
295	E	W	Mid_Inst_Well_W_0_0_-29.8	0.0	0	-29.8	TC (Type-K)
316	A	N	AMB_N_0_42.5_0	0	42.5	0	Gas-TC
317	A	S	AMB_S_0_-42.5_0	0	-42.5	0	Gas-TC
318	A	N	AMB_N_0_42.5_84	0.0	42.5	84	Gas-TC
319	A	S	AMB_S_0_-42.5_84	0.0	-42.5	84	Gas-TC
320	A	N	AMB_N_-12_42.5_84	-12.0	42.5	84	Gas-TC
321	A	S	AMB_S_-12_-42.5_84	-12.0	-42.5	84	Gas-TC
322	A	N	AMB_N_12_42.5_84	12.0	42.5	84	Gas-TC
323	A	S	AMB_S_12_-42.5_84	12.0	-42.5	84	Gas-TC
324	A	N	AMB_N_-97_42.5_84	-97.0	42.5	84	Gas-TC
325	A	S	AMB_S_-97_-42.5_144	-97.0	-42.5	144	Gas-TC
326	A	N	AMB_N_33_42.5_84	33.0	42.5	84	Gas-TC
327	A	S	AMB_S_33_-42.5_84	33.0	-42.5	84	Gas-TC
328	A	N	AMB_N_0_42.5_144	0	42.5	144	Gas-TC
329	A	S	AMB_S_0_-42.5_144	0.0	-42.5	144	Gas-TC
330	A	NW	AMB_NW_14.511_-11.7_-63.3	14.511	-11.7	-63.3	Gas-TC
331	A	SE	AMB_SE_14.511_11.7_225.4	14.511	11.7	225.4	Gas-TC
332	A	NE	AMB_NE_14.511_11.7_225.4	14.511	11.7	225.4	Gas-TC
333	A	SW	AMB_SW_14.511_-11.7_-63.3	14.511	-11.7	-63.3	Gas-TC
335	E	E	Power_feed_tube_E_-0.5_0_180.6	-0.5	0	180.6	TC (Type-K)

#	Face	Dir.	Label	*x* (in.)	*y* (in.)	*z* (in.)	Type
336	I	E	Power_box_air_E_1_0_193.2	1.0	0	193.2	Gas-TC

AMB=A=ambient, E=External, I=Internal

B.3 Hotwire Anemometers

The hotwire anemometers are listed in Table B.5, shown from the east in Figure B.6, and shown isometrically in Figure B.7.

Table B.5 List of hot wire anemometers including position and direction of travel.

#	Position	Travel	Duct	Label	*x* (in.)	*y* (in.)	*z* (in.)
1	inner	*x*-axis	SE	HW_SE_xvar_-7.703_-6.019	variable	-7.7	-6.0
2	middle	*x*-axis	SE	HW_SE_xvar_-11.703_-6.019	variable	-11.7	-6.0
3	outer	*x*-axis	SE	HW_SE_xvar_-15.703_-6.019	variable	-15.7	-6.0
4	horizontal	*y*-axis	SE	HW_SE_14.511_yvar_-5.019	14.511	variable	-5.0
5	inner	*x*-axis	NW	HW_NW_xvar_7.703_-6.019	variable	7.7	-6.0
6	middle	*x*-axis	NW	HW_NW_xvar_11.703_-6.019	variable	11.7	-6.0
7	horizontal	*y*-axis	NW	HW_NW_14.511_yvar_-5.019	14.511	variable	-5.0
8	middle	*x*-axis	NE	HW_NE_xvar_11.703_168.191	variable	11.7	168.2
9	outer	*x*-axis	NE	HW_NE_xvar_15.703_168.191	variable	15.7	168.2
10	horizontal	*y*-axis	NE	HW_NE_14.511_yvar_167.191	14.511	variable	167.2
11	middle	*x*-axis	SW	HW_SW_xvar_-11.703_168.191	variable	-11.7	168.2
12	outer	*x*-axis	SW	HW_SW_xvar_-15.703_168.191	variable	-15.7	168.2
13	horizontal	*y*-axis	SW	HW_SW_14.511_yvar_167.191	14.511	variable	167.2
xvar = variable in *x*-direction, yvar = variable in *y*-direction							

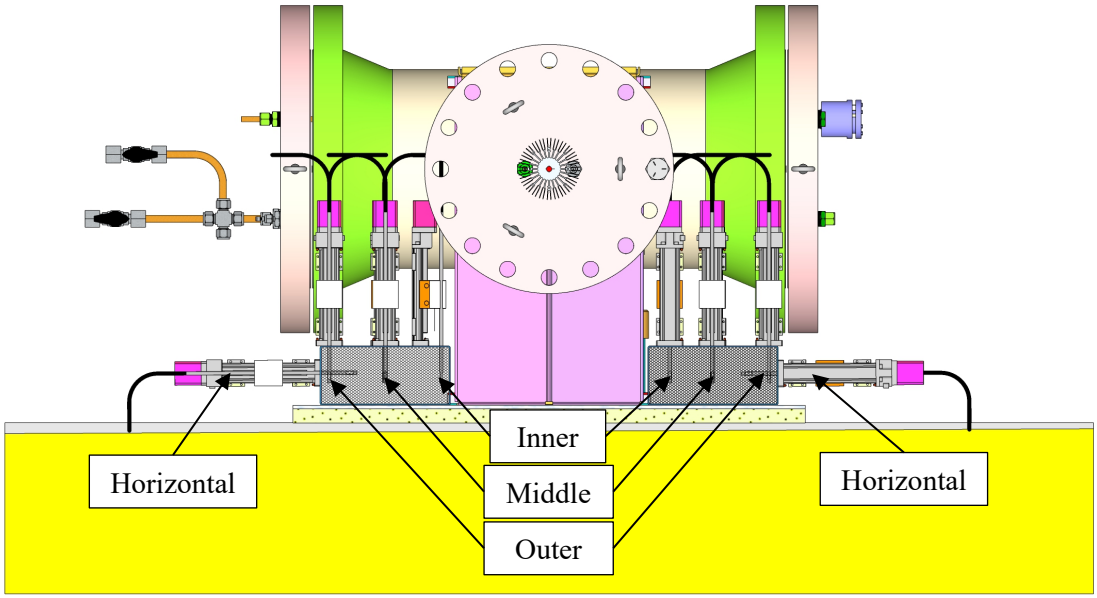

Figure B.6 View of HDCS from east.

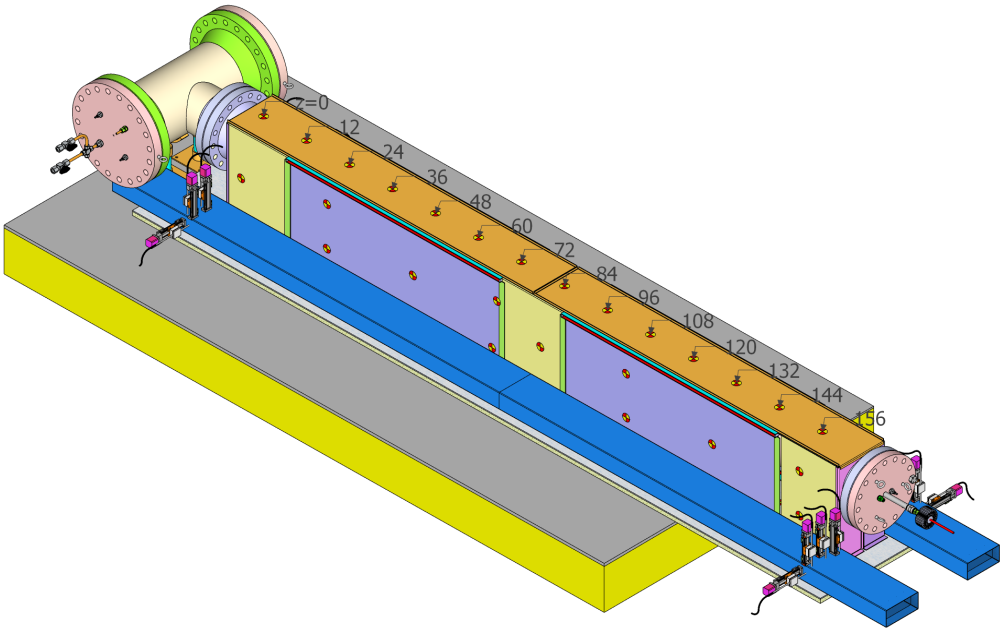

All dimensions are in inches

Figure B.7 Isometric view of HDCS (from southeast) showing vault TCs on top and south side panels and the south side hotwires.

This page is intentionally left blank.

APPENDIX C COMPARISON OF VERTICAL BELOWGROUND DRY CASK SIMULATOR HELIUM AND AIR BACKFILL TEST RESULTS

This report presented steady state results from a total of twenty HDCS tests using various mole fractions of helium, balanced by air, as backfill gases to represent various stages of a loss of helium backfill from a horizontal dry storage canister and the subsequent replacement of helium with air. The results as a whole showed a consistent trend in that as the mole fraction of helium in air decreases, the temperatures within the fuel assembly increase.

Testing results using helium in the vertical dry cask simulator were reported previously in both aboveground and belowground configurations in NUREG/CR-7250 [Durbin and Lindgren, 2018]. However, a comparison between the use of helium versus air backfill gases in the vertical dry cask simulator has yet to be reported. This Appendix presents the results from two belowground test cases. One is the 5.00 kW power, 100 kPa pressure, helium backfill test reported previously in NUREG/CR-7250. The other is an as yet unreported test from the same test series that was also run at 5.00 kW power and 100 kPa pressure, but uses air as a backfill gas instead of helium.

C.1 Steady State Summary Tables

Table C.1 shows the steady state summary tables for the helium and air tests. Note that the PCT locations for the two tests are located on different heater rods and different axial levels, which suggests that the axial temperature profiles will have slightly different trends. Also note that with the dry cask simulator in the vertical belowground configuration, in place of the vault enclosure there was an insulation-covered carbon steel sheet metal shell that simulated concrete and is concentric to the pressure vessel (canister), so the four quadrants are symmetric with regards to the heater rods. Therefore, the maximum temperatures on each component of the DCS are not expected to be located in any particular quadrant (see Figure 2.9 for Quadrant and rod-naming conventions).

Table C.1 Steady state results for the vertical belowground 5.00 kW, 100 kPa helium and air tests.

Mole Fraction He, Balance Air		Power (W)	Pressure (kPa)	PCT (K)	Channel (K)	Basket (K)	Vessel (K)	Shell 1 (K)	Ambient (K)	Tot. Flow Rate (kg/s)
1.0 He	**Average**	**4994**	**99.9**	**703.7**	**624.3**	**555.9**	**473.0**	**394.2**	**296.5**	**0.0699**
	Max	5036	100.2	704.1	624.7	556.4	473.8	395.1	297.9	0.0704
	Min	4954	99.6	703.3	623.9	555.5	472.3	393.3	294.8	0.0694
	Rod or Quadrant #			DT	3	3	3-4 (Corner)	2		
	z-Location (m)			1.22	1.52	1.83	1.83	3.02		
0.0 He	**Average**	**4977**	**100.0**	**780.1**	**679.8**	**580.8**	**470.2**	**392.7**	**299.6**	**0.0646**
	Max	5235	100.5	780.7	680.3	581.0	470.8	393.6	301.2	0.0663
	Min	4759	99.6	779.6	679.4	580.2	469.8	392.3	298.2	0.0635
	Rod or Quadrant #			FV	4	3	1	2		
	z-Location (m)			1.83	1.83	1.83	2.13	3.02		

C.2 Centerline Fuel Axial Temperature Profiles

The axial temperature profiles at the fuel centerline, located at water rod WEU, are shown in Figure C.1. The uncertainty bars corresponding to each plot are the uncertainties in temperature from both tests, based on 1% of the maximum temperature along WEU. As indicated by the profile trends, the helium backfill test generated lower temperatures at WEU than the air backfill test at all axial levels. This was expected due to the superior thermal conductivity of helium over air, and these trends are consistent with the axial temperature profiles from the HDCS shown in Section 3.2.1.

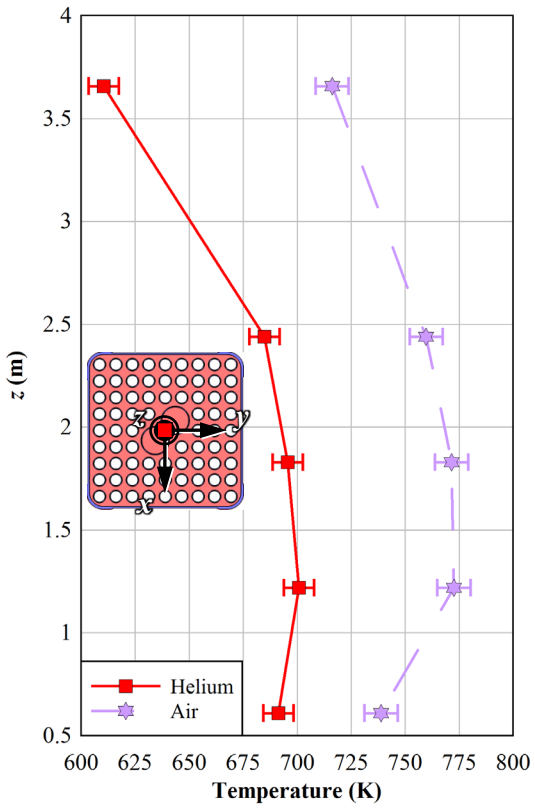

Figure C.1 Centerline fuel axial temperature profiles at water rod WEU for the vertical belowground 5.00 kW, 100 kPa helium and air tests.

C.3 Canister Axial Temperature Profiles

Figure C.2 shows the canister axial temperature profiles along Quadrant 4 from the vertical belowground 5.00 kW, 100 kPa helium and air tests. The uncertainty bars on the 0.0 He data points are the uncertainty in temperature, based on the maximum temperature along the 0.0 He canister axial temperature profile. The shift in the profile trends between the helium and air tests was expected due to the relative locations of the peak cladding temperatures in both tests (shown in Table C.1). The PCT location for the air test was at a higher axial level than the location for the helium test; the differences between the canister axial temperature profile trends for each test stem from each test's respective peak cladding temperature location. At the highest canister temperatures, the differences in temperature between the two tests are within the uncertainty in temperature. Since this was also the case for the HDCS (as shown in Section 3.2.2), this suggests that the measurement of canister temperatures may be insufficient in detecting changes in the canister backfill composition in the event of a loss of helium backfill in a dry storage canister, regardless of canister configuration.

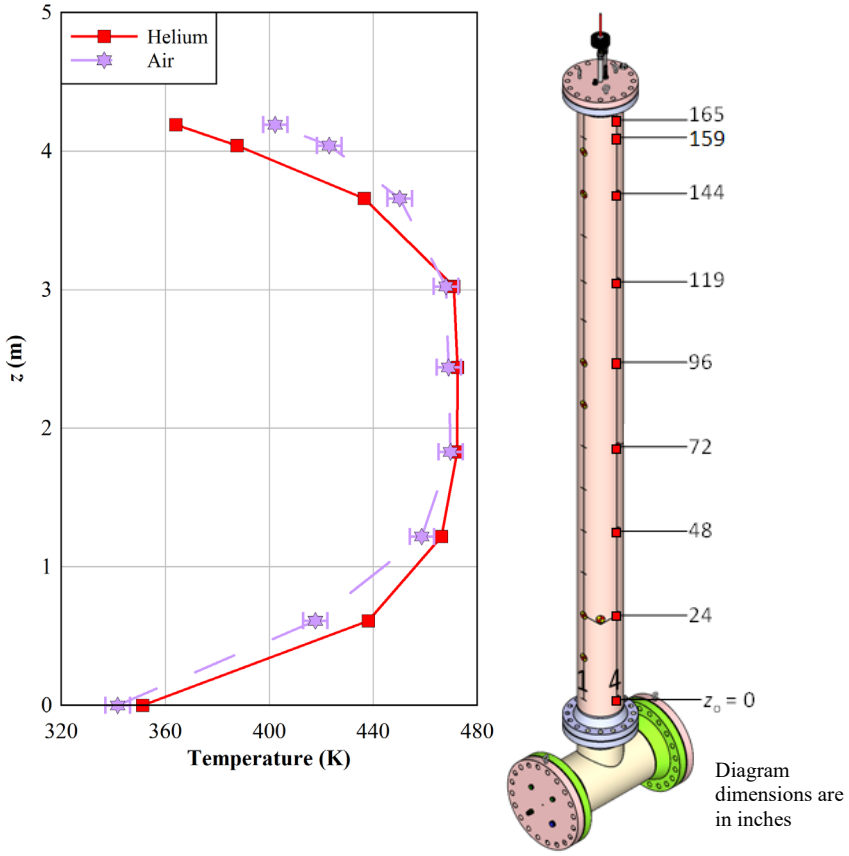

Figure C.2 Axial temperature profiles along Quadrant 4 of the canister for the vertical belowground 5.00 kW, 100 kPa helium and air tests.

C.4 Transverse Temperature Profiles

Figure C.3 shows the transverse temperature profiles from the vertical belowground 5.00 kW, 100 kPa helium and air tests. As expected, the temperatures within and close to the fuel assembly are higher for air than for helium, due to the superior thermal conductivity of helium over air. The temperature differences between the two tests gradually decrease further away from the assembly, with the temperatures at the canister nearly overlapping one another. This is consistent with the transverse temperature trends seen in the HDCS (Section 3.2.3).

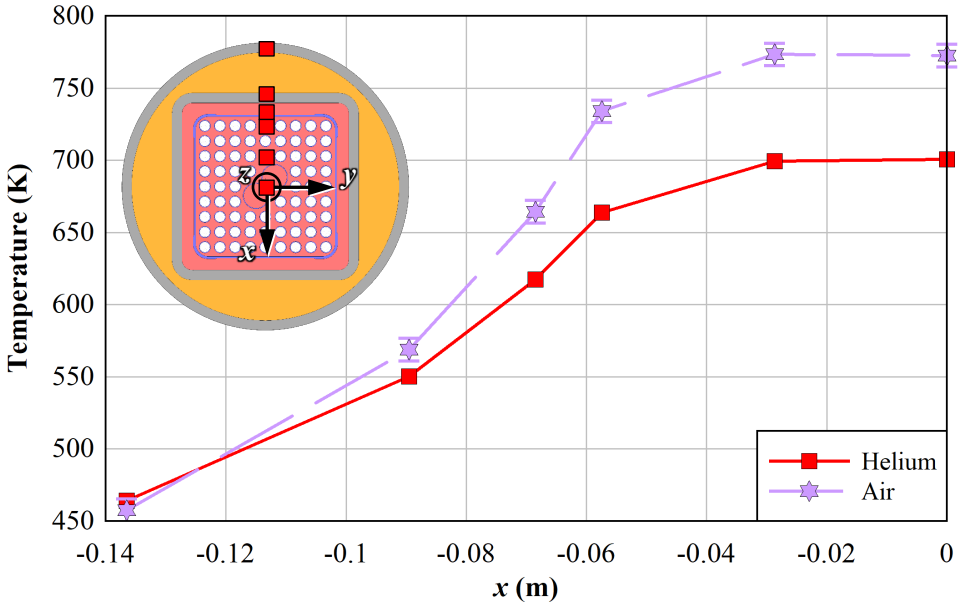

Figure C.3 Transverse temperature profiles at z = 48 in for the vertical belowground 5.00 kW, 100 kPa helium and air tests.

C.5 Conclusions

Although only a helium backfill test and an air backfill test are discussed in this Appendix, rather than a test matrix containing various helium/air blends, the temperature profile trends seen in the HDCS when comparing the helium tests to the air tests are consistent with what is presented here for the vertical belowground DCS. The axial temperature profiles at water rod WEU showed that the temperatures within the fuel assembly are higher for the air backfill than for the helium backfill. The canister axial temperature profiles, at the highest temperatures, are largely similar between the two tests. The transverse temperature profiles show higher fuel assembly temperatures for the air case than for the helium case. The consistency between these results and the results from the HDCS demonstrate that regardless of orientation, a loss of helium backfill from a dry storage canister will result in higher fuel assembly temperatures that are likely to be undetectable by the measurement of canister surface temperatures.

APPENDIX D HORIZONTAL DRY CASK SIMULATOR STEADY-STATE RESULTS TABLES

D.1 Centerline Fuel Axial Temperature Profiles

Table D.1 Centerline fuel axial temperature profiles as a function of the *z*-coordinate for the 0.50 kW tests for all helium mole fractions, balanced by air.

TC Location	*z* (in.)	*z* (m)	Temperature (K)				
			1.0 He	0.9 He	0.5 He	0.1 He	0.0 He
PCT	24.0	0.610	--	--	--	--	--
(Location)	48.0	1.219	373 (ES)	376 (ES)	393 (ES)	415 (ES)	427 (ES)
WEU	24.0	0.610	371	373	389	411	421
	48.0	1.219	371	374	392	412	421
	72.0	1.829	370	372	389	409	418
	96.0	2.438	366	368	384	403	412
	144.0	3.658	343	346	359	370	373
CS	6.0	0.152	353	356	366	385	395
	12.0	0.305	362	364	376	396	408
	18.0	0.457	365	367	379	400	412
	24.0	0.610	369	371	383	404	417
	30.0	0.762	370	372	385	406	419
	36.0	0.914	370	373	385	406	418
	42.0	1.067	370	372	385	405	418
	48.0	1.219	372	374	386	407	419
	54.0	1.372	371	373	385	406	418
	61.0	1.549	370	372	384	404	416
	90.0	2.286	368	370	382	402	414
	96.0	2.438	366	368	380	399	411
	103.0	2.616	363	365	374	393	405
	108.0	2.743	362	364	372	390	403
	114.0	2.896	360	362	370	388	400
	119.0	3.023	358	360	368	385	397
	126.0	3.200	356	359	367	384	395
	132.0	3.353	354	357	365	381	392
GX	72.0	1.829	366	369	389	409	413
	78.0	1.981	366	368	388	409	412
	138.0	3.505	347	351	367	381	384
	144.0	3.658	342	346	361	371	371
	150.0	3.810	329	333	347	354	352
	156.0	3.962	324	331	346	350	346

Table D.2 Centerline fuel axial temperature profiles as a function of the *z*-coordinate for the 1.00 kW tests for all helium mole fractions, balanced by air.

TC Location	*z* (in.)	*z* (m)	Temperature (K)				
			1.0 He	0.9 He	0.5 He	0.1 He	0.0 He
PCT (Location)	24.0	0.610	--	--	--	--	--
	48.0	1.219	433 (ES)	434 (ES)	460 (ES)	488 (ES)	501 (ES)
WEU	24.0	0.610	429	430	456	483	496
	48.0	1.219	430	431	458	483	494
	72.0	1.829	427	428	454	477	489
	96.0	2.438	421	422	446	469	481
	144.0	3.658	381	384	407	425	427
CS	6.0	0.152	401	401	424	446	464
	12.0	0.305	415	415	440	462	482
	18.0	0.457	421	420	445	468	487
	24.0	0.610	426	426	450	473	492
	30.0	0.762	428	428	453	475	494
	36.0	0.914	428	428	453	475	494
	42.0	1.067	428	428	452	474	492
	48.0	1.219	430	430	454	476	494
	54.0	1.372	429	429	453	474	493
	61.0	1.549	427	426	450	471	489
	90.0	2.286	424	424	447	468	485
	96.0	2.438	421	421	444	463	481
	103.0	2.616	415	415	436	454	473
	108.0	2.743	413	413	432	450	469
	114.0	2.896	410	410	429	447	467
	119.0	3.023	407	407	426	445	464
	126.0	3.200	405	405	424	443	461
	132.0	3.353	401	402	422	440	457
GX	72.0	1.829	422	423	452	476	482
	78.0	1.981	421	422	451	475	482
	138.0	3.505	390	393	418	438	443
	144.0	3.658	380	383	407	425	425
	150.0	3.810	355	359	382	398	393
	156.0	3.962	347	353	380	394	383

Table D.3 Centerline fuel axial temperature profiles as a function of the *z*-coordinate for the 2.50 kW tests for all helium mole fractions, balanced by air.

TC Location	*z* (in.)	*z* (m)	Temperature (K)				
			1.0 He	0.9 He	0.5 He	0.1 He	0.0 He
PCT (Location)	24.0	0.610	--	--	--	--	647 (DT)
	48.0	1.219	559 (DT)	562 (DT)	595 (ES)	623 (DT)	--
WEU	24.0	0.610	555	557	592	622	645
	48.0	1.219	553	557	592	620	637
	72.0	1.829	548	552	585	614	630
	96.0	2.438	537	541	574	600	615
	144.0	3.658	466	479	510	531	527
CS	6.0	0.152	506	511	544	578	603
	12.0	0.305	534	536	570	603	632
	18.0	0.457	542	544	578	611	638
	24.0	0.610	550	551	584	615	641
	30.0	0.762	552	554	586	617	641
	36.0	0.914	552	554	586	617	640
	42.0	1.067	551	553	585	616	638
	48.0	1.219	554	556	587	616	639
	54.0	1.372	552	554	585	615	637
	61.0	1.549	548	550	581	611	633
	90.0	2.286	542	545	575	603	622
	96.0	2.438	538	541	570	598	617
	103.0	2.616	527	530	557	586	603
	108.0	2.743	523	525	551	579	597
	114.0	2.896	518	521	547	576	593
	119.0	3.023	513	517	544	573	590
	126.0	3.200	509	513	540	569	585
	132.0	3.353	503	509	536	564	579
GX	72.0	1.829	538	544	581	609	622
	78.0	1.981	538	543	580	609	622
	138.0	3.505	482	494	530	554	555
	144.0	3.658	463	477	511	531	522
	150.0	3.810	408	429	461	475	454
	156.0	3.962	387	426	459	464	431

Table D.4 Centerline fuel axial temperature profiles as a function of the *z*-coordinate for the 5.00 kW tests for all helium mole fractions, balanced by air.

TC Location	*z* (in.)	*z* (m)	Temperature (K)				
			1.0 He	0.9 He	0.5 He	0.1 He	0.0 He
PCT (Location)	24.0	0.610	--	--	733 (DT)	762 (DT)	782 (DT)
	48.0	1.219	694 (DT)	703 (DT)	--	--	--
WEU	24.0	0.610	690	700	731	760	778
	48.0	1.219	684	696	727	755	769
	72.0	1.829	678	689	720	748	762
	96.0	2.438	665	675	704	731	744
	144.0	3.658	572	584	624	647	651
CS	6.0	0.152	628	641	675	709	731
	12.0	0.305	664	675	708	740	762
	18.0	0.457	676	686	719	751	772
	24.0	0.610	684	693	724	754	775
	30.0	0.762	687	696	726	754	775
	36.0	0.914	687	696	725	754	774
	42.0	1.067	686	695	724	752	773
	48.0	1.219	688	696	724	752	772
	54.0	1.372	685	694	722	750	770
	61.0	1.549	680	689	718	747	766
	90.0	2.286	673	682	708	734	751
	96.0	2.438	668	676	703	729	747
	103.0	2.616	654	663	690	714	729
	108.0	2.743	648	655	679	705	722
	114.0	2.896	643	650	676	702	720
	119.0	3.023	638	645	672	700	718
	126.0	3.200	631	639	666	692	710
	132.0	3.353	623	632	661	687	703
GX	72.0	1.829	661	676	710	741	750
	78.0	1.981	661	676	710	741	750
	138.0	3.505	596	608	646	676	682
	144.0	3.658	567	580	621	645	644
	150.0	3.810	474	492	542	557	538
	156.0	3.962	435	468	543	541	498

D.2 Canister Axial Temperature Profiles

Table D.5 Canister axial temperature profiles for the 0.50 kW tests for all helium mole fractions, balanced by air.

Location	*z* (in)	*z* (m)	Temperature (K)				
			1.0 He	0.9 He	0.5 He	0.1 He	0.0 He
Pressure Vessel	0	0.000	314	314	313	313	314
	24	0.610	328	326	324	324	325
	48	1.219	330	329	327	327	328
	72	1.829	328	327	325	325	326
	96	2.438	330	329	327	327	328
	119	3.023	325	324	322	322	323
	144	3.658	318	318	318	318	318
	159	4.039	311	313	314	314	313
	165	4.191	307	308	310	310	309

Table D.6 Canister axial temperature profiles for the 1.00 kW tests for all helium mole fractions, balanced by air.

Location	*z* (in)	*z* (m)	Temperature (K)				
			1.0 He	0.9 He	0.5 He	0.1 He	0.0 He
Pressure Vessel	0	0.000	329	327	325	324	326
	24	0.610	352	348	346	343	345
	48	1.219	356	352	350	348	351
	72	1.829	352	349	347	345	347
	96	2.438	356	352	350	348	351
	119	3.023	346	343	341	340	342
	144	3.658	335	334	335	335	334
	159	4.039	324	324	327	329	326
	165	4.191	316	317	320	322	319

Table D.7 Canister axial temperature profiles for the 2.50 kW tests for all helium mole fractions, balanced by air.

Location	*z* (in)	*z* (m)	Temperature (K)				
			1.0 He	0.9 He	0.5 He	0.1 He	0.0 He
Pressure Vessel	0	0.000	360	358	356	357	358
	24	0.610	407	401	397	396	399
	48	1.219	414	407	404	405	408
	72	1.829	405	401	398	397	399
	96	2.438	412	407	404	404	407
	119	3.023	394	389	387	387	387
	144	3.658	370	373	374	373	367
	159	4.039	345	353	358	357	348
	165	4.191	331	338	344	343	335

Table D.8 Canister axial temperature profiles for the 5.00 kW tests for all helium mole fractions, balanced by air.

Location	*z* (in)	*z* (m)	Temperature (K)				
			1.0 He	0.9 He	0.5 He	0.1 He	0.0 He
Pressure Vessel	0	0.000	397	402	397	397	400
	24	0.610	471	472	464	462	465
	48	1.219	479	479	473	472	476
	72	1.829	469	468	462	461	466
	96	2.438	478	478	473	472	475
	119	3.023	452	451	446	443	448
	144	3.658	417	420	424	421	416
	159	4.039	372	381	396	391	383
	165	4.191	348	358	370	366	361

D.3 Vertical Temperature Profiles

Table D.9 Vertical temperature profiles at z = 1.219 m (48.0 in.) for the 0.50 kW tests for all helium mole fractions, balanced by air.

Location	x (in.)	x (m)	Temperature (K)				
			1.0 He	0.9 He	0.5 He	0.1 He	0.0 He
Vault Top	-6.66	-0.169	315	315	313	314	315
Pressure Vessel Top	-5.38	-0.137	332	331	329	330	331
Basket Top	-3.53	-0.090	344	343	346	350	354
Channel Top	-2.70	-0.068	358	358	366	378	386
EQ	-2.26	-0.057	366	368	382	399	415
ES	-1.13	-0.029	373	376	393	415	427
WEU	0.00	0.000	371	374	392	412	421
Channel Bottom	2.70	0.068	348	347	354	364	367
Basket Bottom	3.53	0.090	344	344	347	351	354
Pressure Vessel Bottom	5.38	0.137	330	329	327	327	328
Vault Bottom	16.6	0.421	303	303	302	302	302

Table D.10 Vertical temperature profiles at z = 1.219 m (48.0 in.) for the 1.00 kW tests for all helium mole fractions, balanced by air.

Location	x (in.)	x (m)	Temperature (K)				
			1.0 He	0.9 He	0.5 He	0.1 He	0.0 He
Vault Top	-6.66	-0.169	331	328	327	326	329
Pressure Vessel Top	-5.38	-0.137	359	355	354	353	356
Basket Top	-3.53	-0.090	381	378	382	387	393
Channel Top	-2.70	-0.068	404	403	417	432	442
EQ	-2.26	-0.057	420	421	442	468	484
ES	-1.13	-0.029	433	434	460	488	501
WEU	0.00	0.000	430	431	458	483	494
Channel Bottom	2.70	0.068	387	386	398	409	418
Basket Bottom	3.53	0.090	381	379	384	388	393
Pressure Vessel Bottom	5.38	0.137	356	352	350	348	351
Vault Bottom	16.6	0.421	309	307	307	306	307

Table D.11 Vertical temperature profiles at z = 1.219 m (48.0 in.) for the 2.50 kW tests for all helium mole fractions, balanced by air.

Location	x (in.)	x (m)	Temperature (K)				
			1.0 He	0.9 He	0.5 He	0.1 He	0.0 He
Vault Top	-6.66	-0.169	368	364	363	364	367
Pressure Vessel Top	-5.38	-0.137	421	414	414	416	420
Basket Top	-3.53	-0.090	462	458	466	477	486
Channel Top	-2.70	-0.068	506	505	525	545	562
EQ	-2.26	-0.057	536	538	569	595	617
ES	-1.13	-0.029	558	561	595	624	645
WEU	0.00	0.000	553	557	592	620	637
Channel Bottom	2.70	0.068	477	476	498	521	534
Basket Bottom	3.53	0.090	464	461	469	478	484
Pressure Vessel Bottom	5.38	0.137	414	407	404	405	408
Vault Bottom	16.6	0.421	323	321	320	321	321

Table D.12 Vertical temperature profiles at z = 1.219 m (48.0 in.) for the 5.00 kW tests for all helium mole fractions, balanced by air.

Location	x (in.)	x (m)	Temperature (K)				
			1.0 He	0.9 He	0.5 He	0.1 He	0.0 He
Vault Top	-6.66	-0.169	416	416	414	416	421
Pressure Vessel Top	-5.38	-0.137	492	492	488	490	496
Basket Top	-3.53	-0.090	555	558	565	577	585
Channel Top	-2.70	-0.068	618	625	643	662	676
EQ	-2.26	-0.057	663	672	697	723	741
ES	-1.13	-0.029	693	703	731	760	777
WEU	0.00	0.000	684	696	727	755	769
Channel Bottom	2.70	0.068	577	586	612	643	655
Basket Bottom	3.53	0.090	555	560	567	576	582
Pressure Vessel Bottom	5.38	0.137	479	479	473	472	476
Vault Bottom	16.6	0.421	340	344	342	342	343

D.4 Horizontal Temperature Profiles

Table D.13 Horizontal temperature profiles at z = 1.829 m (72.0 in.) for the 0.50 kW tests for all helium mole fractions, balanced by air.

Location	y (in.)	y (m)	Temperature (K)				
			1.0 He	0.9 He	0.5 He	0.1 He	0.0 He
WEU	0.00	0.000	370	372	389	409	418
GU	1.13	0.029	370	373	391	414	419
IU	2.26	0.057	365	367	381	398	401
Channel	2.70	0.068	355	356	365	376	379
Basket	3.51	0.089	344	343	346	350	353
Pressure Vessel	5.38	0.137	331	330	329	329	331
Vault	6.50	0.165	306	307	305	306	306

Table D.14 Horizontal temperature profiles at z = 1.829 m (72.0 in.) for the 1.00 kW tests for all helium mole fractions, balanced by air.

Location	y (in.)	y (m)	Temperature (K)				
			1.0 He	0.9 He	0.5 He	0.1 He	0.0 He
WEU	0.00	0.000	427	428	454	477	489
GU	1.13	0.029	429	430	456	484	491
IU	2.26	0.057	419	420	439	462	467
Channel	2.70	0.068	401	400	414	427	433
Basket	3.51	0.089	380	377	382	386	392
Pressure Vessel	5.38	0.137	358	354	353	351	354
Vault	6.50	0.165	315	313	312	311	313

Table D.15 Horizontal temperature profiles at z = 1.829 m (72.0 in.) for the 2.50 kW tests for all helium mole fractions, balanced by air.

Location	y (in.)	y (m)	Temperature (K)				
			1.0 He	0.9 He	0.5 He	0.1 He	0.0 He
WEU	0.00	0.000	548	552	585	614	630
GU	1.13	0.029	550	554	590	619	634
IU	2.26	0.057	532	534	566	591	607
Channel	2.70	0.068	499	500	522	540	552
Basket	3.51	0.089	459	456	464	473	481
Pressure Vessel	5.38	0.137	416	410	409	410	414
Vault	6.50	0.165	334	331	330	331	333

Table D.16 Horizontal temperature profiles at z = 1.829 m (72.0 in.) for the 5.00 kW tests for all helium mole fractions, balanced by air.

Location	y (in.)	y (m)	Temperature (K)				
			1.0 He	0.9 He	0.5 He	0.1 He	0.0 He
WEU	0.00	0.000	678	689	720	748	762
GU	1.13	0.029	677	691	722	752	763
IU	2.26	0.057	651	664	693	719	729
Channel	2.70	0.068	607	616	637	657	665
Basket	3.51	0.089	549	554	560	571	577
Pressure Vessel	5.38	0.137	482	483	480	481	486
Vault	6.50	0.165	361	363	361	361	366


Sandia National Laboratories